FIELD AND CIRCUIT COMBINED ANALYSIS OF PERMANENT MAGNET SYNCHRONOUS MOTORS

PING ZHOU

FIELD AND CIRCUIT COMBINED ANALYSIS OF PERMANENT MAGNET SYNCHRONOUS MOTORS

by

©PING ZHOU

A thesis submitted in partial fulfillment
of the requirements for the degree of
Doctor of Philosophy

Faculty of Engineering and Applied Science
Memorial University of Newfoundland

May 1994

St. John's Newfoundland Canada

ISBN 0-315-96073-6

Abstract

A complete procedure has been developed to predict the steady-state and dynamic performances of permanent magnet synchronous machines. The major feature in this study is to combine a finite element analysis with a lumped parameter circuit model in order to provide satisfactory engineering information but at small computational effort. To this end, two co-ordinated stages are involved. One is to develop a unified lumped parameter circuit model applicable for both steady-state and transient analysis. The other stage is to extract individual lumped parameters from finite element solutions based on corresponding equivalent circuits, each with a predetermined topology.

In this study, static magnetic field calculation is applied to determine the load-dependent direct and quadrature axis reactance parameters X_d, X_q and excitation voltage E_0, in which the effect of the interaction between the d-axis and q-axis quantities is included. Time-varying eddy-current field calculation is used to get starting parameters which serve as the investigation of dynamic behaviour. In order to simplify the time-varying field calculation, time phasor is used to separate the time variable from the field equation based on the introduction of equivalent reluctivity in terms of equivalent magnetic energy. In order to cope with the voltage supply, corresponding finite element formulae are derived with complete elimination of the iterative process for starting current. Due to the availability of the accurate field-based operational parameters, it has become possible to use the lumped parameter circuit model to obtain the complete starting and synchronous performances.

As an integral part of this study, an effort has been directed to the experimental investigation on the steady-state and dynamic performances. A new load test method is proposed to determine the load dependent parameters X_d, X_q and E_0. In addition, a new microprocessor-based digital torque angle measurement system was designed and built to provide improved accuracy and fast data sampling for measuring and control purposes. At the same time, a scheme for accurately locating the position of zero torque angle is proposed with avoiding access to the internal construction of a machine.

The proposed techniques have been successfully applied to a 1 hp laboratory permanent magnet motor. There exists excellent agreement between the simulated and experimental results.

Acknowledgement

I would like to express my most sincere gratitude and appreciation to my supervisor Dr. M.A. Rahman, for his guidance, encouragement and active support throughout the course of this study.

My special thanks to Dr. J.E. Quaicoe and Dr. M.J. Hinchey, members of the supervisory committee, for their constructive criticisms and useful suggestions in preparing this thesis.

Help from the technical staff at the Faculty of Engineering and Applied Science is gratefully acknowledged. Assistance of fellow graduate students is appreciated.

I also like to take this opportunity to acknowledge the financial support through Memorial University of Newfoundland and Dr. Rahman's grant which made this work possible.

Finally, my dedication is due to my wife and daughter, for their understanding, patience and support.

Contents

List of Figures

Chapter 1

Introduction

1.1 A General Description of PM Motors

Increasing interest has been shown in using Permanent magnet(PM) synchronous motors with variable-frequency inverters in adjustable-speed drives, taking advantage of the increased efficiency and power factor product to reduce volt-ampere (VA) requirements[1]. These motors are also widely used at the fixed main frequency source.

Depending on the location of the magnets on the rotor, typical permanent magnet synchronous machines can be broadly classified into three kinds: interior PM synchronous motors which have the permanent magnets buried inside the rotor; surface PM synchronous motors which have their permanent magnets mounted on the surface of the rotor; and inset PM synchronous motors in which the permanent magnets are inset or partially inset into the rotor[2, 3, 4]. Depending on the orientation of the magnet magnetization, the rotor can also be classified as radially oriented type or circumferential type. For interior and inset type configurations, the direction of magnetization can be either radial or circumferential. For surface type configuration, the only direction of magnetization is radial.

For the line frequency start motor, which is normally fed by a fixed voltage source, some sort of conduction or squirrel cage winding is required to develop the starting torque. The squirrel cage also protects the magnets from demagnetization during the startup transient and sudden increase in the stator current, and also acts as a damper to the machine oscillation. This helps to keep the rotor in synchronism. For a variable speed motor fed from the current source inverter, although there is no need to develop the starting induction torque, as the motor drive can be started synchronously from standstill, the damper windings are helpful in reducing the distortion and spikes of line-to-line voltage[5]. The damper windings can also reduce the commutating inductance, and thus help in reducing the commutation overlap. Therefore, damper windings are also employed in these drives. However, for the drive with voltage-source inverter, dampers on the rotor would provide a path for the flow of harmonic currents induced from the non-sinusoidal voltage inverter waveforms[6]. Therefore, it is advantageous not to have dampers in this kind of drives with voltage source inverters..

Figure 1.1 shows the operation of a PM machine at different portions of the demagnetization curve of the B-H loop. The maximum flux density B_r corresponding to point A' is available initially if the magnet is short-circuited with steel keepers. When the magnet is installed in the machine, operating point B will correspond to the no-load line. With load current flowing in the stator winding, the armature reaction effect will further reduce the flux density. A load line $\overline{OD}$ corresponding to worst-case demagnetization may be due to starting, pull-in or other transient conditions. Once the operating point D is reached and the demagnetization effect is removed, the magnet will recover along the recoil line, which has approximately

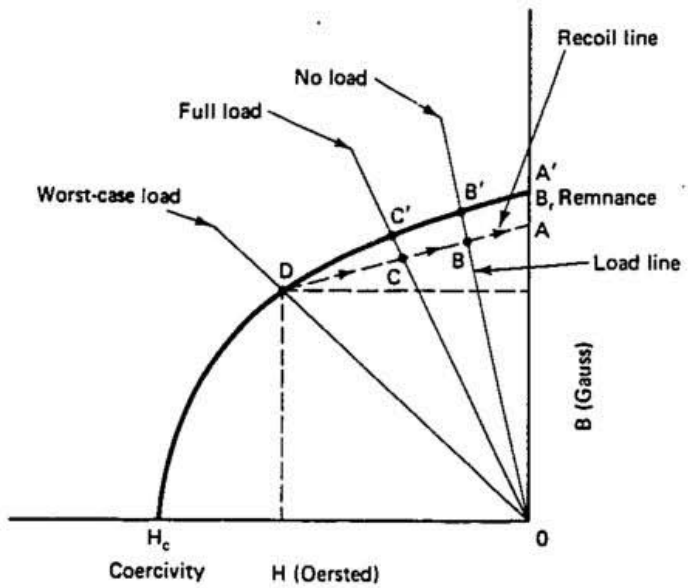

Figure 1.1: PM machine operating points on B-H curve

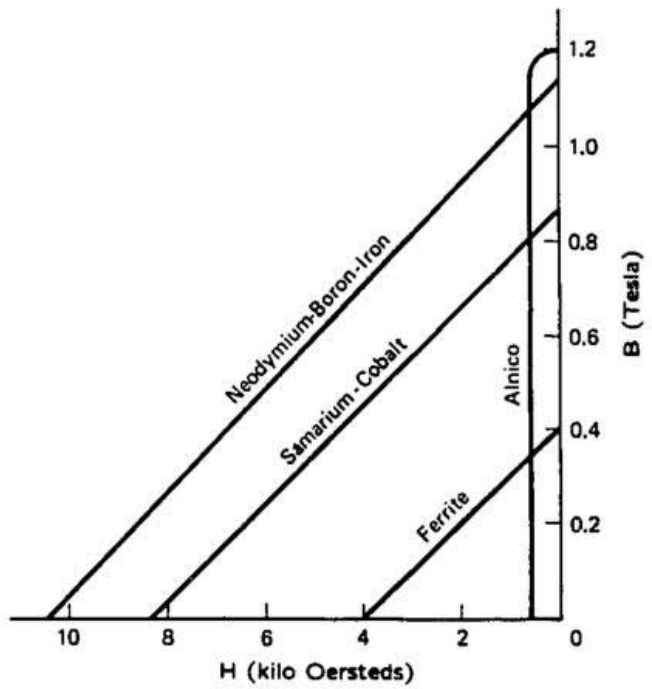

Figure 1.2: Permanent-magnet characteristics

the same slope as the original B-H curve near $H = 0$. Subsequently, the stable operating point will be determined by the intersection of the load line and the recoil line. If the material of the permanent magnet has a straight line demagnetization curve, the recoil line will always trace back along the demagnetization curve with negligible demagnetization effect. Characteristic demagnetization curves for some PM materials are shown in Fig. 1.2. Alnico has the high remanence but the coercivity is low, with a nonlinear demagnetization curve. Therefore, it is now seldom used in ac motor design. Ferrite material is low in cost and has excellent linearity in demagnetization, but the remanence is low, making the machine somewhat bulky. Samarium-Cobalt has substantially increased residual flux density and coercivity as compared with ferrite, but cost is high and likely to remain so. As a result, it is used in high performance servo drives, where a high torque to inertia ratio is desirable. A further increase in residual flux density and coercivity has been achieved with the introduction of Neodymium-Boron-Iron (NdBFe) magnet material at a lower cost than the Samarium-Cobalt material. One potential limitation of NdBFe material in comparison with other high energy magnets is its relatively low temperature limit.

For a variable speed PM motor fed from a variable frequency source, the stator frequency is derived from the rotor position information making use of a shaft position sensor. The machine is therefore always in synchronism with the stator supply irrespective of the machine speed without the help of a squirrel cage winding. With a variable frequency current source power supply, below base speed, the speed is controlled by varying the stator current, and above base speed, it is controlled by weakening the airgap flux. The torque control can be achieved by controlling

the magnitude of the stator current and the spatial angle, β, between the stator magnetomotive force (mmf) this current produces and the rotor mmf produced by magnets. For a power supply from a variable frequency voltage source, the basic control strategy is to operate the motor at a constant flux below base speed and at a constant terminal voltage above base speed. The constant flux operation below base speed is achieved by operating the machine at a constant $voltage/frequency$ ratio, which is increased at low speed to compensate for the stator resistance drop.

Upon energizing a PM motor on fixed frequency supply, the squirrel cage winding provides accelerating torque to carry the rotor to near synchronous speed. This accelerating torque must overcome, not only the applied load torque, but also the generated magnet braking torque due to the presence of the permanent magnet flux. When the rotor reaches a speed close to synchronous speed, the magnets then pull the rotor into synchronism. As the load is applied, the rotor develops torque by increasing the torque angle δ between the rotor direct axis and the axis of resultant airgap magnetic field.

If a PM motor is to have line starting capability, the interior magnet type design with radial magnetization appears to be the most economical to manufacture for the need of a squirrel cage. The interior magnet type also offers the advantages of mechanical robustness and a smaller airgap, which allows for a degree of flux weakening, when the motors are expected to operate in the constant power mode at high speed. In order to be concise and explicit but without lack of generality, this thesis will take the interior magnet type as a working model. An example of the structure is shown in Fig. 1.3.

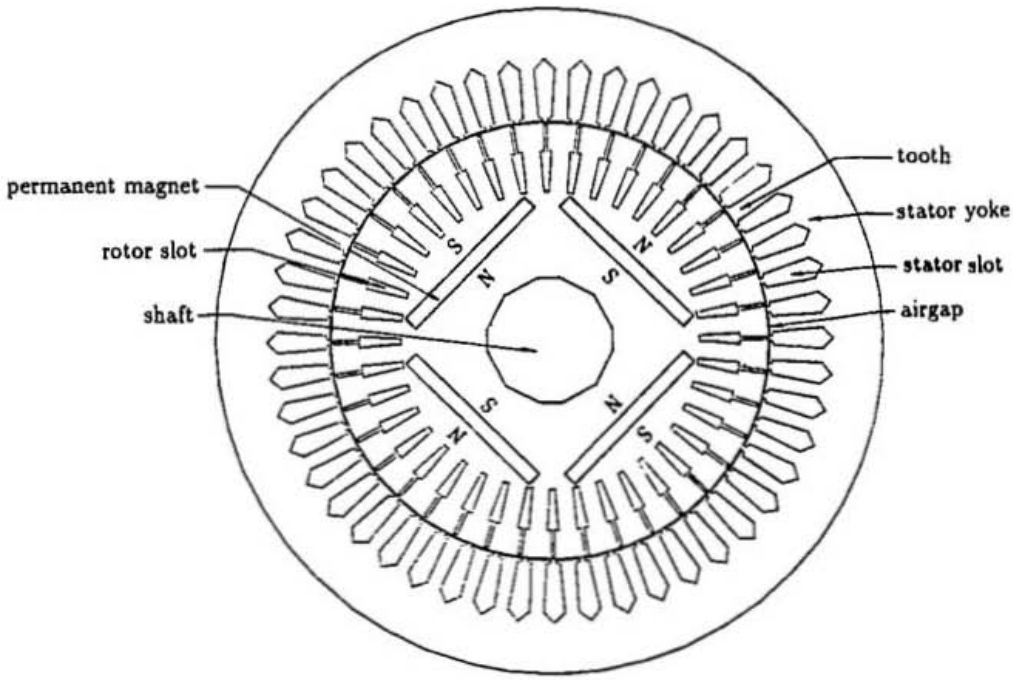

Figure 1.3: Configuration of interior-type PM motor with radial magnetization

1.2 Literature Survey

Due to the increased competition in world markets and the pressure of increased cost of electrical energy, plus the relatively high price of permanent magnets, it is essential to predict accurately the synchronous and dynamic performances of the proposed design of a PM motor in order to avoid the design misjudgement that can prove costly once the motor is manufactured. This situation has necessitated a parallel development of more accurate and practical computation techniques. The topic of both synchronous and dynamic performance analyses has been treated extensively in the literature[7, 8, 9, 10, 11]. Equivalent circuits and lumped parameter models have been traditionally used to calculate the performance of electrical machines and to conduct the design with idealized and simplified physical representation. However, it is difficult to use the traditional analytical method to calculate their characteristics taking into account the effect of magnetic saturation, complex configuration, eddy currents and external system impedances at the same time. Numerical techniques have been recognized as practical and accurate method of field computation to aid in electrical design[12]. Finite elements, amongst numerical methods, have emerged as suitable techniques for electrical design and performance evaluation in low frequency applications, because its elements can be easily adapted to any shape of boundary and interface geometry. The method has been applied with success to non-linear material[13], eddy current problems[14, 15] and permanent magnets[16]. Different post-processing techniques based on finite-element solutions have been developed for the improvement of behavior prediction and design optimization[15, 17]. But this is a time-consuming process. In order to achieve a computationally simple and at the same time functionally accurate

model, a hybrid technique which combines field and electric equivalent circuit has become the subject of considerable efforts[18, 19, 20].

Although recent years have witnessed considerable applications of finite element technique to the analysis of PM synchronous motors, there are still many problems waiting for solutions. It is recognized that the starting point of finite element method (FEM) is in fact based on Maxwell's equations, where the current appears as a cause, producing magnetic flux as an effect, thereupon the induced voltage. Therefore, for PM motors fed by current source inverter, FE analysis is relatively easy to implement[20]. However, in the case of voltage source inverter, the voltage is the cause and current being the effect. This limitation leads to a time-consuming and inconvenient iteration process. In addition, previous investigation of PM motor using FEM was more or less directed towards the study of specific operation modes such as no load or at rated load.

The effects of saturation for PM motor are more profound. Various authors have noted the influence of magnetic saturation upon the performance of PM motors, and some motor design procedures were introduced to take saturation into account including the prediction of reactance parameters[21, 22, 23]. But what is perhaps easily overlooked is the assumption that the magnet excitation voltage E_0 is constant. In addition, little attempts have been made to computationally deal with the interaction between the direct and quadrature axis fields on the operating performance and the determination of saturated parameters.

The common methods for torque evaluation are of these three types: a) Lorentz force method, b) virtual work principle method and c) Maxwell stress tensor method[24, 25]. For the Lorentz force method, the problem region must consist entirely of non-

ferromagnetic material. The virtual work principle method needs numerical differentiation of co-energy. The technique may suffer from cancellation problem, since it relies on the difference between quantities of nearly equal magnitude. For Maxwell stress tensor method, its accuracy is rather susceptible to mesh discretization and the selection of the integration contour. So, some special techniques are needed to make these methods useful in practice[26, 27, 28]. It is also to be noted that all the above methods are based on the flux density distribution. In such a case, each flux density component will no longer satisfy the continuity condition at inter-element boundaries, especially, in the region such as in small airgap where large gradient of magnetic field occurs due to the fact that first-order element solutions are preferable to high-order element solutions[15].

The starting performance of PM motors fed from a constant frequency source from the moment of switch-on to the onset of stable synchronous operation forms a most important part of assessment of such drives for any practical application. Although the methods characterized by these earlier works[9, 29] have provided a general framework for calculating the starting characteristics of a PM synchronous motor, all of these methods assume constant parameters during the starting process. In addition, little investigation of synchronization has been reported. In fact, the rotor parameters will change significantly with the rotor slip due to the magnetic saturation and skin effect. Recently, some efforts have been made to calculate the starting characteristics directly using finite element method by a non-linear time-stepping method with incremental change in rotor position[30, 31]. Since the convergence of the time-stepping procedure can only be ensured by taking extremely small increments in time, the storage and processing time required would be very

large, and the feasibility is still doubtful.

The test investigation of PM motor is another challenging subject. Owing to certain inherent features of PM motor, the standard ac motor test procedures are no longer suitable for the PM synchronous motor. Some measurements of saturated parameters have been reported[3, 32], but these have mainly been under unrepresentative conditions, such as no load or short circuit, etc., when the stator current is purely reactive. Although the load test method[23, 33] was proposed to determine the d-axis reactance X_d from the stator d-axis voltage component and q-axis reactance X_q from q-axis voltage component, respectively, under the actual operating conditions, it is subject to the assumption of constant E_0. It has been shown from the load test that there is a load range where X_d is extremely irregular and becomes difficult to determine. Even negative value of X_d can be obtained. It was recognized that the irregularity is due to the assumption of constant E_0. The failure to consider the variation of E_0 with load is due to the difficulty that effects the magnet excitation voltage and the d-axis armature reaction are inherently linked together by the stator d-axis voltage component and usually cannot be separated. The static inductance measurement method[23] is available to evaluate X_d by using a special bridge circuit (see Appendix A). Since this test is static, there will be no magnet induced voltage E_0 in the stator winding. This gives a means to extract the value of X_d. The significant disadvantages of this method are that hysteresis effects produce a certain amount of scatter in the results, and the thermally induced variation in the bridge resistance leads to the difficulty in maintaining a balanced condition. Furthermore, it is hard to choose the actual quantities of d- and q-axis currents to simulate a real load condition. More recently, a static test

in conjunction with a no-load test was reported to determine the parameters[35]. Although this method is convenient for practical use by avoiding measuring load angle, it is conducted under two assumptions: (i) E_0, X_q are independent of I_d; (ii) X_d is independent of I_q. Both these assumptions are not realistic.

Accurate torque angle measurement is essential for the proper evaluation of motor performance. The torque angle is also an important control parameter for variable frequency inverter driven PM motors. It is obvious that the measurement is required within an interval of time that should be very small compared to the mechanical time constant of the machine. In addition, with increasing emphasis on on-line digital control, it has also become necessary to obtain the quantities of load angle in digital form. Therefore, the conventional stroboscopic method[22, 33] is no longer suitable for practical application. Due to the inherent features of a PM motor, the precision of measured torque angle is highly related to the accuracy of the positioning of zero torque angle. But so far, to the best of the author's knowledge, either approximate methods are available or an auxiliary prime mover[22, 33] is required to locate the position of zero torque angle.

After this brief examination of current status, it is fair to say that although impressive progress has been made in the development of PM motors, there are still many challenging problems waiting for solutions.

1.3 Thesis Objectives and Outline

In this study, efforts are directed to develop a complete and practical procedure for the steady-state and dynamic performance analysis of PM synchronous motors with the objectives of providing accurate engineering information while, at the same

time, retaining an efficient calculation process with low computational effort.

To this end, the major feature in this study is the combination of finite element analysis with lumped parameter circuit model. This approach can not only greatly simplify the analysis and evaluation of machine performance, but also complete the two-dimensional (2D) finite element method by introducing the possibility to take into account the 3D part of the machine. Another advantage is the ability to consider such a machine as a component of a much wider system. This approach will involve two coordinated stages. One is to develop a unified lumped parameter circuit model applicable for both the steady-state and dynamic analysis. The other stage is to extract individual lumped parameters from the associated finite element solutions based on corresponding equivalent circuits, each with a predetermined topology.

In this study, static magnetic field calculation will be applied to determine the load-dependent parameters X_d, X_q and E_0 of a PM motor for different load conditions. Time-varying eddy-current field calculation will be used to get the starting parameters and serve as the investigation of dynamic behaviours. As an integral part of this study, some novel measurement techniques are developed to verify the theoretical results in a laboratory set-up.

An outline of the remaining chapters of this thesis is given as follows:

Using coordinate transformation and matrix technique, a unified lumped parameter model is developed in Chapter 2 for investigating both the steady-state and dynamic behaviours. In terms of the developed mathematical model, some distinguishing features of PM motor are discussed. A per-phase equivalent circuit, rather than the usual separated d-axis and q-axis equivalent circuits, is also pro-

posed to embody the saliency of a PM motor and account for the influence of iron losses on synchronous performance such as current, efficiency and power factor.

The finite element model for static magnetic field calculation is described in Chapter 3. For simulating a PM motor fed from voltage source supply, a practical procedure is proposed to accommodate the finite element model to voltage source supply based on the Newton-Raphson iterative algorithm and updated parameter evaluation in conjunction with a scheme for effective estimation of initial phase current. The static magnetic field solutions are then applied to determine the saturated parameters X_d, X_q and E_0 with different load conditions using a new method, called the loading method, in which the effects of E_0 variation with loads and interaction between the d-axis and q-axis field are included. In addition, an improved approach called the flux method is introduced to carry out the torque calculation, by which the evaluated torque values are no longer susceptible to mesh discretization. One advantage of a field-based analysis is that a realistic assessment can be made of iron losses. For a better evaluation of iron losses, the effect of distortion and minor loop of flux density profiles is also considered.

Chapter 4 starts with the presentation of time-varying eddy-current finite element model for current source supply. In order to simplify the time-varying field calculation, time-phasor is used to separate the time variable from the field equation based on the introduction of equivalent reluctivity in terms of magnetic energy. The use of phasor analysis implies that field solutions do not need to be time-stepped, giving a significant speed advantage compared to time-stepped model. Experience shows that time-stepping approach takes typically two or more orders of magnitude longer time than its complex phasor approach counterpart[36], which is not

incapable of giving satisfactory accuracy based on the appropriate choosing of the effective reluctivity. Then, in order to cope with voltage source, corresponding finite element formulae are derived with complete elimination of iterative process for starting current. It follows that based on the solutions of nonlinear eddy-current fields, a procedure for obtaining the starting parameters taking account of the saturation and skin effect is developed. Finally, various starting performances are examined.

The testing aspect of permanent magnet synchronous motor is dealt with in Chapter 5. A modified load test method is proposed to determine three important load-dependent parameters X_d, X_q and E_0. The results bring forward a clear picture of the impact of the assumption of constant E_0, as made in the earlier load test method, on the value of X_d. In order to satisfy the needs for improved accuracy and fast data sampling, a microprocessor-based digital torque angle measurement system is developed. At the same time, a scheme for accurately positioning the zero torque angle and avoiding access to the internal construction of a motor is described.

As an application example of the developed simulation and testing techniques in the preceding chapters, a laboratory 1 hp 4-pole interior-type PM motor is employed for detailed investigation in Chapter 6. Various simulation and test results of synchronous and starting performances are provided.

The summary and conclusions of this thesis and the contributions of this study are highlighted in Chapter 7, together with suggestions for further study in this area.

Chapter 2

Lumped Parameter Model

In this chapter, a generalized lumped parameter model is derived. A per-phase equivalent circuit will be introduced to account for the saliency of a PM motor and the influence of iron losses.

2.1 Generalized System Equation

The performance analysis of a PM synchronous motor can be initiated by developing the system model equations in matrix form. Analysis will be given for the 3-phase motor, since this class of PM motor is the most likely candidate for wide industrial drive applications. The standard two-axis theory with fixed rotor reference frame will be used. A transformation that compacts the three-phase model to such an equivalent two-phase description is not difficult to find. In fact, a large number of such transformations exist. However, it is desirable to utilize a particular transformation for the voltage and currents such that the representation of electrical power in the machine is preserved. As a result, the developed torques are invariant over the transformation. At the same time, it would be convenient that the transformation be the same for both voltage and current. Assuming that a

square transformation matrix [C] satisfies these two requirements of invariant power and identical transformations for both current and voltage, the variables $\{i\}_{abc}$ and $\{v\}_{abc}$ in 3-phase abc system are transformed to a new set of variables $\{i\}_{dq0}$ and $\{v\}_{dq0}$ in $dq0$ system by

$$\{v\}_{dq0} = [C]\,\{v\}_{abc} \tag{2.1}$$

$$\{i\}_{dq0} = [C]\,\{i\}_{abc} \tag{2.2}$$

Power invariance is described by

$$\begin{aligned} \{v\}^t_{abc}\{i\}_{abc} &= \{v\}^t_{dq0}\{i\}_{dq0} = ([C]\,\{v\}_{abc})^t([C]\,\{i\}_{abc}) \\ &= \{v\}^t_{abc}[C]^t[C]\{i\}_{abc} \end{aligned} \tag{2.3}$$

where superscript t denotes the transpose of the variable. Therefore,

$$[C]^t\,[C] = [I] \tag{2.4}$$

where [I] is an identity matrix. Thus, a necessary condition on the transformation matrix [C] satisfying the requirements of invariant power and identical transformations for both current and voltage is

$$[C]^{-1} = [C]^t \tag{2.5}$$

That is, the transformation matrix [C] must be Hermitian or orthogonal. Equivalently, [C] must be unitary.

It is noted that once the transformations of both current and voltage are specified, the transformation of impedance is automatically determined by

$$\begin{aligned} \{v\}_{dq0} &= [C]\,\{v\}_{abc} = [C]\,[Z]_{abc}\,\{i\}_{abc} \\ &= [C]\,[Z]_{abc}[C]^{-1}\,\{i\}_{dq0} = [Z]_{dq0}\,\{i\}_{dq0} \end{aligned} \tag{2.6}$$

Therefore,

$$[Z]_{dq0} = [C]\,[Z]_{abc}\,[C]^{-1} = [C]\,[Z]_{abc}\,[C]^{t} \tag{2.7}$$

For the model of a PM motor under investigation, the following specific matrix [C] will be applied to define the transformation of variables from the stationary reference frame abc to the rotor reference frame $dq0$[37]

$$[C] = \sqrt{\frac{2}{3}} \begin{bmatrix} \cos\theta_r & \cos(\theta_r - \frac{2\pi}{3}) & \cos(\theta_r + \frac{2\pi}{3}) \\ -\sin\theta_r & -\sin(\theta_r - \frac{2\pi}{3}) & -\sin(\theta_r + \frac{2\pi}{3}) \\ 1/\sqrt{2} & 1/\sqrt{2} & 1/\sqrt{2} \end{bmatrix} \tag{2.8}$$

where θ_r is the angle between the d-axis and the axis of phase A. It can be easily verified that this transformation matrix [C] satisfies the requirements of invariant power and identical transformation for both current and voltage using the condition of Eqn. (2.5). Since three-phase PM motors usually have balanced wye-connected or delta-connected windings with no neutral connection and thus effectively have only two independent phases, the transformation matrix [C] can be further reduced to the following form in the absence of zero-sequence component

$$[C] = \sqrt{\frac{2}{3}} \begin{bmatrix} \cos\theta_r & \cos(\theta_r - \frac{2\pi}{3}) & \cos(\theta_r + \frac{2\pi}{3}) \\ -\sin\theta_r & -\sin(\theta_r - \frac{2\pi}{3}) & -\sin(\theta_r + \frac{2\pi}{3}) \end{bmatrix} \tag{2.9}$$

When such a transformation is applied to the variables of a three-phase PM motor, the three-phase symmetrical windings A, B and C can be replaced by equivalent two-phase windings d and q as shown in Fig. 2.1, in which the magnets are identified by i_f and rotor cage is represented by equivalent shorted D, Q windings.

If the three-phase terminal voltages are

$$\begin{bmatrix} v_A \\ v_B \\ v_C \end{bmatrix} = \begin{bmatrix} \sqrt{2}V\cos\omega t \\ \sqrt{2}V\cos(\omega t - 120°) \\ \sqrt{2}V\cos(\omega t - 240°) \end{bmatrix} \tag{2.10}$$

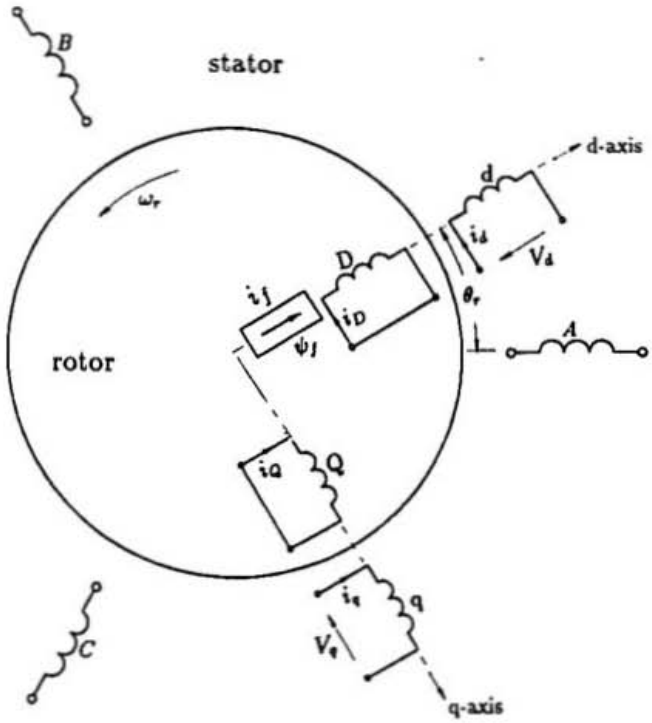

Figure 2.1: Physical model of a PM motor

then through commutator transformation described by Eqn. (2.9), the corresponding voltages in $dq0$ system will be

$$\begin{bmatrix} v_d \\ v_q \end{bmatrix} = \sqrt{3}V \begin{bmatrix} \cos(\omega t - \theta_r) \\ -\sin(\omega t - \theta_r) \end{bmatrix} \tag{2.11}$$

For such an equivalent primitive commutator machine, with the conventional directions shown in Fig. 2.1 and subject to *motor* conventions, the system governing equation can be written as

$$\{v\} = [Z]\{i\} = ([R] + [L]p + [G]\omega_r)\{i\} \tag{2.12}$$

where p is the derivative operator. The diagonal resistance matrix $[R]$, symmetric inductance matrix $[L]$ and asymmetric torque matrix $[G]$ are given by Eqns. (2.13)-(2.15), respectively

$$[R] = diag(r_1, r_1, r_{2d}, r_{2q}, r_f) \tag{2.13}$$

$$[L] = \begin{bmatrix} L_d & 0 & L_{md} & 0 & 0 \\ 0 & L_q & 0 & L_{mq} & 0 \\ L_{md} & 0 & L_D & 0 & 0 \\ 0 & L_{mq} & 0 & L_Q & 0 \\ 0 & 0 & 0 & 0 & 0 \end{bmatrix} \tag{2.14}$$

$$[G] = \begin{bmatrix} 0 & L_q & 0 & L_{mq} & 0 \\ -L_d & 0 & -L_{md} & 0 & -L_{md} \\ 0 & 0 & 0 & 0 & 0 \\ 0 & 0 & 0 & 0 & 0 \\ 0 & 0 & 0 & 0 & 0 \end{bmatrix} \tag{2.15}$$

and the voltage and current vectors are given by Eqns. (2.16) and (2.17), respectively

$$\{v\} = \{v_d\ v_q\ v_D\ v_Q\ E_0\}^t = \{v_d\ v_q\ 0\ 0\ E_0\}^t \tag{2.16}$$

$$\{i\} = \{i_d\ i_q\ i_D\ i_Q\ i_f\}^t \tag{2.17}$$

where suffixes d and q denote the d-axis and q-axis quantities of the stator, respectively; suffixes D and Q denote the d-axis and q-axis quantities of the rotor, respectively. Letter L denotes the inductances, and suffix m denotes the mutual quantities between d-axis and q-axis. The magnet is represented by equivalent current i_f whose value is defined by

$$E_0 = r_f i_f = \frac{1}{\sqrt{3}} \omega L_{md} i_f \tag{2.18}$$

where E_0 is the induced phase voltage in abc system by the magnet only under synchronous speed. The torque matrix is derived from the fact that the motion induced voltage terms are the ones that contribute to the electromechanical power conversion process and, therefore, are associated with the torque:

$$T_e = P\{i\}^t[G]\{i\} = P[(L_q - L_d) i_d i_q - L_{md} i_q i_D + L_{mq} i_d i_Q - L_{md} i_q i_f] \tag{2.19}$$

where P is the number of pole pairs.

It should be noted that equations (2.12) and (2.19) are quite general. These equations describe the steady-state as well as transient conditions. The parameters in these equations will change with loads due to the effects of magnetic saturation and skin effect. These load dependent parameters will be determined from finite element solutions.

It can be understood that system equations (2.12) and (2.19) are applicable to a PM motor fed by either voltage source or current source with fixed frequency or variable frequency.

2.2 Model Specialization

Although the established generalized system model equation (2.12) has provided the capability for complete analysis of any operation mode of a PM motor, it is still advisable to specialize the generalized system equations for a particular operation mode. It will not only simplify the calculation but also provide a convenient way to explore some distinguishing features of a PM motor.

In order to have a deep insight into the starting characteristics of a PM motor fed from a fixed frequency source, two approaches cooperate to deal with asynchronous performance during run-up. One is the quasi-dynamic analysis approach with pseudo-constant speed characteristic. The other is transient analysis approach. The former can lead to an identification of different current and torque components and presents a clear physical interpretation of the cause of each component, and allow convenient parameter sensitivity analysis on the overall system; while the latter will provide more detailed information such as possible demagnetizing effect on the magnets, maximum current requirement for the converter and the time of run-up to stable synchronization, as well as synchronization process.

2.2.1 Quasi-dynamic Model

The quasi-dynamic analysis model is based on the assumption that the motor operates under steady-state at each slip point during run-up assuming that the mechanical time constants are very large compared with the electrical time-constants. Therefore, using quasi-dynamic analysis model, no electromagnetic transient is taken into account.

If we assume magnetic materials are linear, starting process can be treated as

the superposition of two operation modes. One mode is the operation of an unsymmetric asynchronous motor alone. The other one is the operation mode of a magnet-excited asynchronous generator with short-circuit stator windings. However, saturation phenomenon in fact is unavoidable. This difficulty is surmounted by adopting adjusted saturated parameters, where the interaction between the two modes has been appropriately considered. Consequently, the superposition scheme is assumed for the analysis.

Unsymmetric Asynchronous Motor Mode

It has been shown in Eqn. (2.11) that for balanced three phase terminal voltages, the corresponding transformed two-phase voltages in the rotating rotor frame will be

$$\begin{bmatrix} v_d \\ v_q \end{bmatrix} = \sqrt{3}V \begin{bmatrix} \cos(\omega t - \theta_r) \\ -\sin(\omega t - \theta_r) \end{bmatrix} = \sqrt{3}V \begin{bmatrix} \cos(s\omega t + \delta) \\ -\sin(s\omega t + \delta) \end{bmatrix} \tag{2.20}$$

where s is the slip. The value of δ is the final angle at which the system would have operated had the machine synchronized. The concern at hand is only run-up that ends just under synchronism and not to synchronism, itself. In this case, the angle δ is irrelevant and is equated to zero. Since all the exciting functions are sinusoidal and of the same angular frequency $s\omega$ in d-q axis system, the use of complex phasor is preferred. With $\dot{V}_d$ as reference phasor, the applied voltage source can be expressed as

$$\begin{bmatrix} \dot{V}_d \\ \dot{V}_q \end{bmatrix} = \sqrt{\frac{3}{2}}V \begin{bmatrix} 1 \\ j \end{bmatrix} \tag{2.21}$$

The p operator of the impedance matrix can be replaced by $js\omega$ to obtain the steady-state impedance matrix. If let $\mu = \omega_r/\omega = 1 - s$, then ω_r can be replaced

by $\mu\omega$. Omitting the row of the impedance matrix corresponding to permanent magnet, because only asynchronous motor mode is considered at hand, we have

$$[Z] = \begin{bmatrix} r_1 + jsX_d & \mu X_q & jsX_{md} & \mu X_{mq} \\ -\mu X_d & r_1 + jsX_q & -\mu X_{md} & jsX_{mq} \\ jsX_{md} & 0 & r_{2d} + jsX_D & 0 \\ 0 & jsX_{mq} & 0 & r_{2q} + jsX_Q \end{bmatrix} \tag{2.22}$$

For the convenience of solving, it is suitable to eliminate the shorted rotor part first, which leads to the reduced impedance matrix

$$[Z'] = \begin{bmatrix} r_1 + jsX_d + \frac{s^2 X_{md}^2}{r_{2d}+jsX_D} & \mu X_q - \frac{js\mu X_{mq}^2}{r_{2q}+jsX_Q} \\ -\mu X_d + \frac{js\mu X_{md}^2}{r_{2d}+jsX_D} & r_1 + jsX_q + \frac{s^2 X_{mq}^2}{r_{2q}+jsX_Q} \end{bmatrix} \tag{2.23}$$

Hence, the stator currents can be figured out by the inverse of impedance matrix $[Z']$, and we then proceed to obtain the shorted rotor currents in terms of rotor voltage equations. Let the solutions be represented by

$$\{\dot{I}^m\} = \left\{ \begin{array}{cccc} \dot{I}_d^m & \dot{I}_q^m & \dot{I}_D^m & \dot{I}_Q^m \end{array} \right\}^t = \left\{ \begin{array}{cccc} A+jB & C+jD & E+jF & G+jH \end{array} \right\}^t \tag{2.24}$$

where A, B, C, D, E, F, G and H are real and imaginary parts of each current, respectively; and each is a function of slip. For simplicity the superscripts m and g are used for the *motor* mode and *generator* mode, respectively. The instantaneous quantity of each current component corresponding to asynchronous motor mode will be

$$\{i^m\} = \begin{Bmatrix} i_d^m \\ i_q^m \\ i_D^m \\ i_Q^m \end{Bmatrix} = \begin{Bmatrix} \sqrt{2}(A\cos s\omega t - B\sin s\omega t) \\ \sqrt{2}(C\cos s\omega t - D\sin s\omega t) \\ \sqrt{2}(E\cos s\omega t - F\sin s\omega t) \\ \sqrt{2}(G\cos s\omega t - H\sin s\omega t) \end{Bmatrix} \tag{2.25}$$

Magnet-excited Asynchronous Generator mode

In this case the stator windings are shorted and thus $V_d = V_q = 0$. At the same time, it is obvious that no induced currents exist in the rotor windings, that

is, $i_D^g = i_Q^g = 0$. It is also noted that the only excitation source $\omega_r L_{md} i_f$ is constant and the steady-state impedance matrix is obtained by replacing p with zero. If the term $\omega_r L_{md} i_f$ is moved to the left of the equality, Eqn. (2.12) can be written as

$$\begin{Bmatrix} 0 \\ \omega_r L_{md} i_f \end{Bmatrix} = \begin{bmatrix} r_1 & \mu X_q \\ -\mu X_d & r_1 \end{bmatrix} \begin{Bmatrix} i_d^g \\ i_q^g \end{Bmatrix} \tag{2.26}$$

The shorted-circuit currents in the stator can be readily obtained as

$$\{i^g\} = \begin{Bmatrix} i_d^g \\ i_q^g \\ i_D^g \\ i_Q^g \end{Bmatrix} = \frac{\sqrt{3}}{r_1^2 + \mu^2 X_d X_q} \begin{Bmatrix} -\mu^2 X_d X_q E_0 \\ \mu r_1 E_0 \\ 0 \\ 0 \end{Bmatrix} \tag{2.27}$$

Current of Each Winding

Superposing the results of the above two operating modes results in the d-q axis instantaneous current components of each winding,

$$\{i\} = \{i^m\} + \{i^g\} \tag{2.28}$$

The results can be transformed back to *abc* system to get the instantaneous value of each phase current if necessary. For example, for *A*-phase in the absence of zero-sequence component, the current i_A becomes

$$i_A = \sqrt{\frac{2}{3}}(\cos\theta_r i_d + \sin\theta_r i_q) \tag{2.29}$$

The total instantaneous torque containing both average and pulsating components can be determined by substituting equation (2.28) in the torque expression (2.19).

2.2.2 Transient Model

If both the mechanical and electromagnetic transients are needed to be included in the analysis, a true transient model is necessary. In addition to the system

equation (2.12), the other necessary equations to deal with transient behavior are the mechanical equations as follows:

$$p\delta = \omega - \omega_r \tag{2.30}$$

and

$$p\omega_r = \frac{P}{J}(T_e - T_L) - \frac{B}{J}\omega_r \tag{2.31}$$

where $T_e = \{i\}^t[G]\{i\}$ is the electro-dynamic torque defined by Eqn. (2.19); T_L is the load torque; B is the friction coefficient; p is the time derivative and J is the moment of inertia. From equations (2.12), (2.30) and (2.31), it is obviously convenient to choose the four currents i_d, i_q, i_D and i_Q, the rotor torque angle δ and the rotor speed ω_r as the state-variables. Thus, with necessary rearrangement the above equations can be expressed in state variable form as

$$\begin{cases} p\delta = \omega - \omega_r \\ p\omega_r = \frac{P}{J}(T_e - T_L) - \frac{B}{J}\omega_r \\ pi_d = \frac{1}{\Delta_d}(r_1 L_D i_d + L_q L_D \omega_r i_q - L_{md} r_{2d} i_D + L_{mq} L_D \omega_r i_Q - \sqrt{3} L_D V \cos\delta) \\ pi_q = \frac{1}{\Delta_q}(-L_d L_Q \omega_r i_d + r_1 L_Q i_q - L_{md} L_Q \omega_r i_D - L_{mq} r_{2q} i_Q - \sqrt{3} L_Q V \sin\delta \\ \qquad - L_{md} L_Q \omega_r i_f) \\ pi_D = \frac{1}{\Delta_d}(-r_1 L_{md} i_d - L_{md} L_q \omega_r i_q + L_d r_{2d} i_D - L_{md} L_{mq} \omega_r i_Q + \sqrt{3} L_{md} V \cos\delta) \\ pi_Q = \frac{1}{\Delta_q}(L_{mq} L_d \omega_r i_d - r_1 L_{mq} i_q + L_{md} L_{mq} \omega_r i_D + L_q r_{2q} i_Q + \sqrt{3} L_{mq} V \sin\delta \\ \qquad + L_{md} L_{mq} \omega_r i_f) \end{cases} \tag{2.32}$$

where $\Delta_d = L_{md}^2 - L_d L_D$, $\Delta_q = L_{mq}^2 - L_q L_Q$, $\delta = \omega t - \theta_r$. It is noted that the system of state-variable equations is nonlinear which implies that the simulation of run-up response of a PM motor can only be achieved by solving the equation (2.32) numerically.

2.2.3 Synchronous Operation Model

Upon considering synchronous behavior of this system, it is only a matter of setting the derivative terms to zero and $\omega_r = \omega$ or $s = 0$. Due to $i_D = i_Q = 0$, in terms of equations (2.20) and (2.22) the system equation in reduced order form is given as

$$\begin{Bmatrix} -\sqrt{3}V\sin\delta \\ -\sqrt{3}V\cos\delta + \sqrt{3}E_0 \end{Bmatrix} = \begin{bmatrix} r_1 & X_q \\ -X_d & r_1 \end{bmatrix} \begin{Bmatrix} i_d \\ i_q \end{Bmatrix} \tag{2.33}$$

where δ is the torque angle. Therefore, equation (2.33) can be easily solved to get

$$\begin{Bmatrix} i_d \\ i_q \end{Bmatrix} = \frac{\sqrt{3}}{r_1^2 + X_d X_q} \begin{Bmatrix} V(X_q\cos\delta - r_1\sin\delta) - E_0 X_q \\ -V(r_1\cos\delta + X_d\sin\delta) + E_0 r_1 \end{Bmatrix} \tag{2.34}$$

Correspondingly, the torque equation (2.19) can be reduced to

$$T_e = P[(L_q - L_d)i_d i_q - L_{md} i_q i_f] \tag{2.35}$$

Substituting equation (2.34) into Eqn. (2.35), one can readily obtain the overall torque characteristic of a PM motor. At this stage, it is necessary to clarify one of the distinguishing features of PM motors, that is, $L_d < L_q$. Since permanent magnets usually have a relative permeability close to that of free space, for interior-type PM motor, the magnet thicknesses appear as large-series air gaps in the d-axis magnetic flux paths. The q-axis magnetic flux can pass through the ferromagnetic pole pieces without crossing the magnet and therefore the stator phase inductance is noticeably higher with q-axis rotor orientation. One of the most important consequences of having $L_d < L_q$ can be seen in the torque versus torque angle characteristic, which can be derived from Eqn. (2.35). Substituting equation (2.34) into Eqn. (2.35) while neglecting the stator resistance to make the interpretation

of the results straightforward leads to

$$\begin{aligned} T_e &= \frac{3P}{\omega}[\frac{E_0 V}{X_d}\sin\delta - \frac{V^2}{2}(\frac{1}{X_d} - \frac{1}{X_q})\sin 2\delta] \\ &= T_{e1}\sin\delta + T_{e2}\sin 2\delta \end{aligned} \tag{2.36}$$

where

$$\begin{aligned} T_{e1} &= \frac{3P E_0 V}{\omega X_d} \\ T_{e2} &= \frac{3P V^2}{2\omega}(\frac{X_q - X_d}{X_d X_q}) \end{aligned} \tag{2.37}$$

and P is pole pairs, V is per phase applied voltage. Compared with a conventional synchronous motor, for which $X_d > X_q$, the reluctance torque T_{e2} is reversed in sign. It implies that, at normal supply voltage, the total torque can be negative between $\delta = 0$ and $\delta = \delta_0$ as indicated in Fig. 2.2. Since $\delta = 0$ is generally an unstable point, the no-load operation of a PM motor occurs at $\delta = \delta_0$. This means that at no-load neither the d-axis nor the q axis is aligned with the axis of armature flux. The reason is that in this range of torque angles the reluctance torque tends to align the rotor q-axis with the armature current, whereas the magnet flux tends to align the d-axis with the flux axis produced by 3-phase armature currents. Since the reluctance torque varies with $\sin 2\delta$ and the magnet alignment torque varies with $\sin\delta$, there are ranges of δ in which these torques are additive, resulting in a higher pull-out torque than would be obtained with either by itself. The value of δ_0 can be approximately derived by manipulating Eqn. (2.36) as

$$\delta_0 = \cos^{-1}\{\frac{E_0}{V(1 - X_d/X_q)}\} \tag{2.38}$$

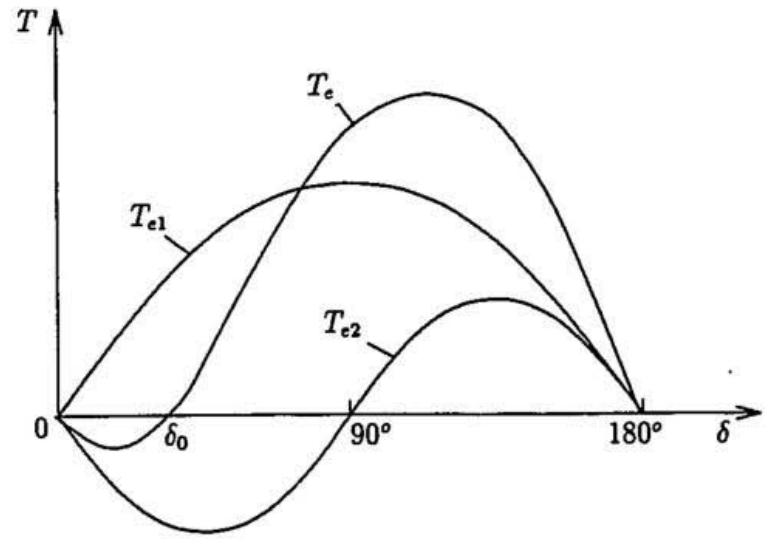

Figure 2.2: Typical torque versus torque angle characteristics of an interior-type PM motor

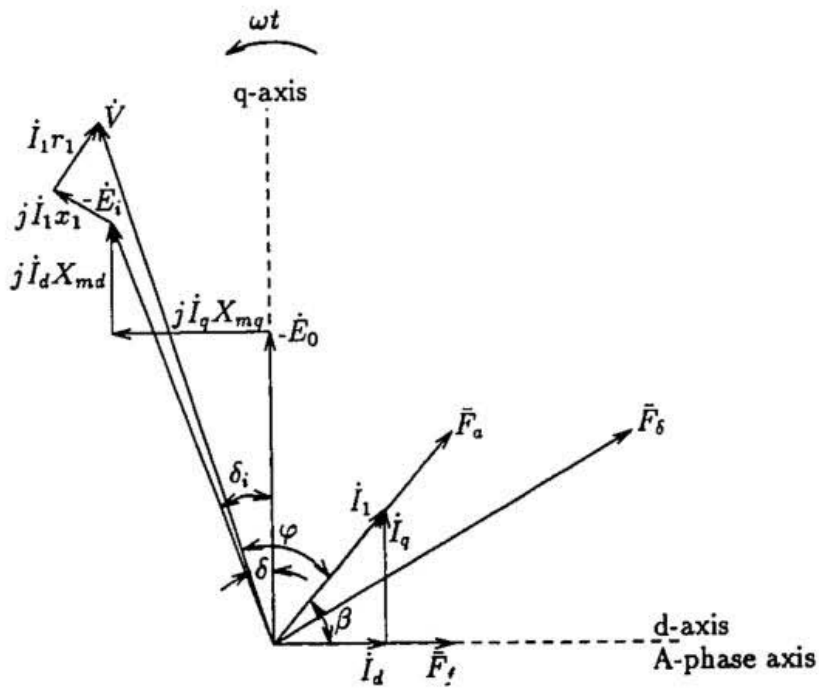

Figure 2.3: PM motor phasor diagram ignoring iron loss

2.3 Per-phase Equivalent Circuit

It is well known that, for salient-pole synchronous machines, two separate d-axis and q-axis equivalent circuits as well as a phasor diagram are usually employed to deal with synchronous performance analysis. As improved computation of losses and efficiency are required, a per-phase equivalent circuit will be more useful.

With reference to the phasor diagram shown in Fig. 2.3, which ignores iron losses, the voltage equation can be expressed as

$$\begin{aligned}
\dot{V} &= -\dot{E}_0 + \dot{I}_1 r_1 + j\dot{I}_1 x_1 + j\dot{I}_d X_{md} + j\dot{I}_q X_{mq} \\
&= -\dot{E}_0 + \dot{I}_1 r_1 + j\dot{I}_1 x_1 + j\dot{I}_1 X_{mq} + j\dot{I}_d (X_{md} - X_{mq}) \\
&= -\dot{E}_0 + \dot{I}_1 r_1 + j\dot{I}_1 x_1 + j\dot{I}_1 X_{mq} + \dot{I}_1 \cos\beta \sin\beta (X_d - X_q) + j\dot{I}_1 \cos^2\beta [(X_d - X_q)] \\
&= -\dot{E}_0 + \dot{I}_1 r_1 + j\dot{I}_1 x_1 + j\dot{I}_1 X_{mq} + \dot{I}_1 r_e + j\dot{I}_1 x_e \qquad (2.39)
\end{aligned}$$

where

$$r_e = \cos\beta \sin\beta (X_d - X_q) \qquad (2.40)$$

$$x_e = \cos^2\beta [(X_d - X_q)] \qquad (2.41)$$

It is interesting to note that with the introduction of two parameters r_e and x_e, only phase current I_1, rather than d-q axis components I_d and I_q, appears in the voltage equation (2.39). This suggests that a per-phase equivalent circuit can be constructed, as shown in Fig. 2.4. It is noted from equations (2.40) and (2.41) that, if the machine has no saliency, r_e and x_e become zero and the equivalent circuit assumes the same form as for the cylindrical-rotor machine. The parameters r_e and x_e will also become saturated, because they depend on X_d and X_q which vary with load conditions. It can be observed from Eqns. (2.40) and (2.41) that x_e can be

negative for permanent magnet machines as $X_d < X_q$; and r_c can be either positive or negative depending on the excitation angle β.

Since the phasor diagram in Fig. 2.3 and the per-phase equivalent circuit in Fig. 2.4 ignore iron and stray-load losses, corresponding performance evaluation should be regarded as approximate. In order to further include iron and stray-load losses, a modified per-phase equivalent circuit is proposed as shown in Fig. 2.5(a). A shunt resistor r_c is placed across the internal voltage E_i to account for the voltage dependent iron loss. At the same time, another resistor r_s is placed across the stator leakage reactance x_1 to account for the current dependent stray-load losses.

Parameter r_c can be determined in terms of finite element-based calculation of iron loss, P_c, details of which will be described in the next chapter. The values of r_c usually vary with the load conditions. For a specific load, then

$$r_c = \frac{3E_i^2}{P_c} \tag{2.42}$$

Stray-load losses are comprised of many intricate components, not just additional iron loss due to the stator leakage flux. The value of stray-load losses, P_s, may be computed by conventional method under a given rated operating condition[42]. The equivalent resistance representing the stray-load losses can be evaluated from

$$r_s = \frac{P_s}{3I_1''^2} \tag{2.43}$$

where I_1'' is a component of the rms value of the rated current.

It may be computationally convenient to further convert the connection between r_s and x_1 from parallel to series as shown in Fig. 2.5(b): the two components of the equivalent series impedance are

$$r_s' = \frac{x_1^2 r_s}{r_s^2 + x_1^2} \tag{2.44}$$

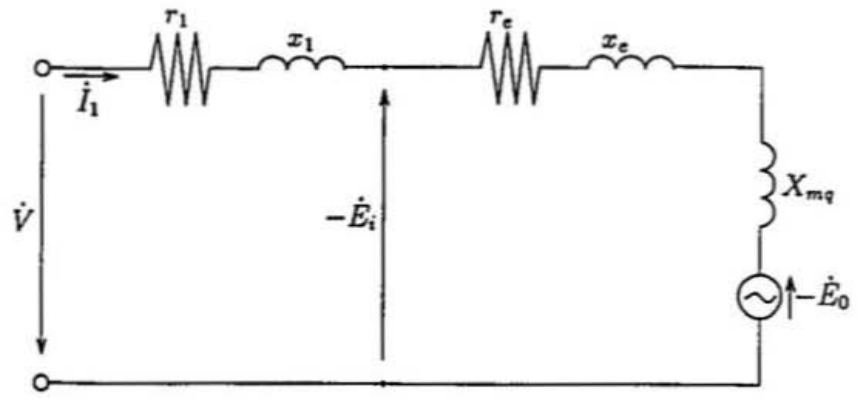

where

$$r_e = (x_d - x_q)\ \cos\beta\ \sin\beta$$
$$x_e = (x_d - x_q)\ \cos^2\beta$$

Figure 2.4: Per-phase equivalent circuit of PM motor ignoring iron loss

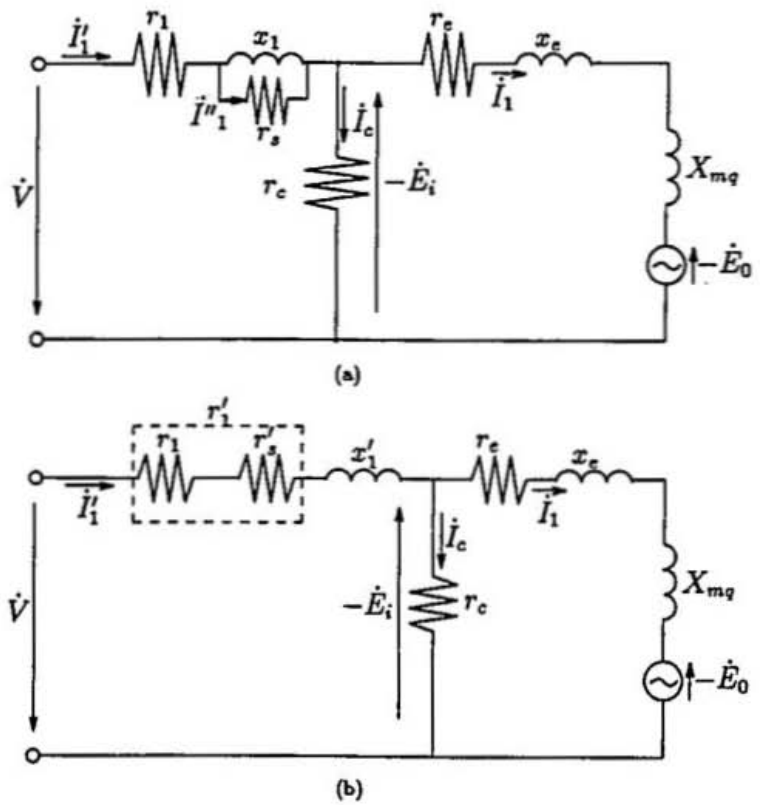

Figure 2.5: Modified Per-phase equivalent circuit of PM motor taking into account iron and stray-load losses

$$x_1' = \frac{x_1 r_s^2}{r_s^2 + x_1^2} \tag{2.45}$$

Furthermore, r_1 and r_s' can be combined to give

$$r_1' = r_1 + r_s' \tag{2.46}$$

Therefore, the introduction of the adjusted parameters r_1' and x_1' can serve as an aid to include the effect of stray-load losses. Correspondingly, the adjusted phasor diagram can be expressed as Fig. 2.6, where

$$\dot{I}_1' = \dot{I}_1 + \dot{I}_c \tag{2.47}$$

and

$$\dot{I}_c = -\frac{\dot{E}_i}{r_c} \tag{2.48}$$

The above developed lumped parameter model for a PM motor has provided a framework for the performance prediction of both synchronous operation and starting process. However, the effectiveness of the model and the accuracy of the resulting simulation results will definitely rest on how close those adopted lumped parameters in the model can represent a true operating condition. This will be the topic of the next two chapters.

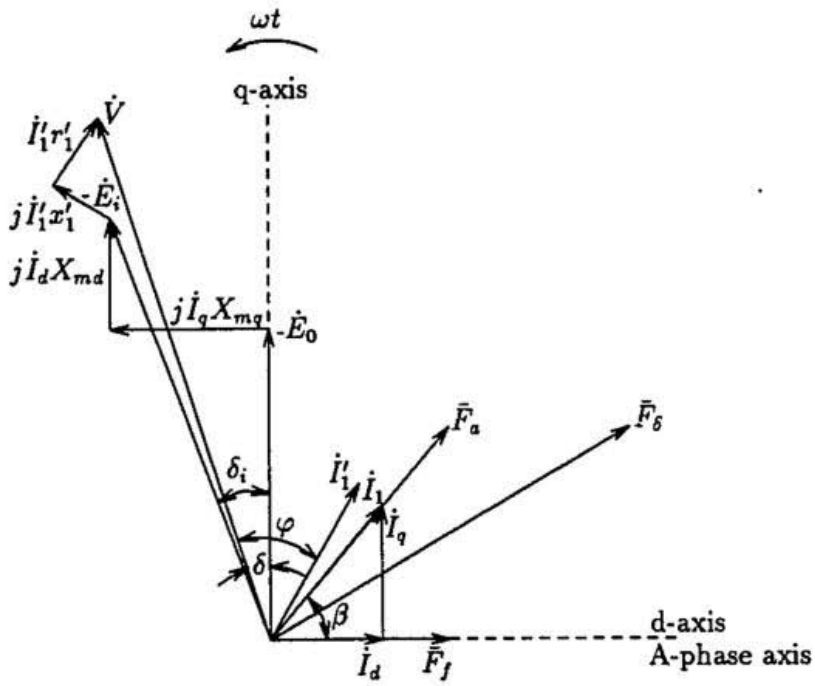

Figure 2.6: Adjusted PM motor phasor diagram taking into account iron and stray-load losses

Chapter 3

Simulation of Synchronous Performance

In this chapter, the finite element model for static magnetic field calculation is described. In order to simulate voltage source supply, a Newton-Raphson iterative procedure is presented based on the updated parameter evaluation. Then, a new method is proposed to determine the three important synchronous parameters X_d, X_q and E_0 from load field solutions.

3.1 Introduction to Finite Element Method

The finite element analysis is based on a variational approach according to which the field problem is formulated in terms of a variational expression called energy functional. In most engineering applications, this expression can be identified with the energy stored in the system. Minimization of the energy functional leads to Euler equation which is the partial differential equation describing the field. The field problem is solved by searching for a function that minimizes the energy functional directly, instead of attempting to solve the differential equation. Natural boundary conditions which are also known as Neumann boundary, are implicit in

the energy functional formulation. In order to implement the variational approach by means of numerical computations, the continuous function representing the exact solution of the problem is approximated by functions defined over each of the discrete elements into which the field region is subdivided.

Two dimensional (2D) finite element analysis is applied to obtain complete solution of the field in a cross-section of a PM motor under actual load conditions. The magnetic field prevailing in the interior of the machine can be described in terms of the vector potential $\bar{A}$. In two-dimensional rectangular coordinates, nonlinear magnetostatic Poisson equation problem is

$$\begin{aligned} \Omega: \quad & \frac{\partial}{\partial x}(\nu\frac{\partial A}{\partial x}) + \frac{\partial}{\partial y}(\nu\frac{\partial A}{\partial y}) = -J \\ s_1: \quad & A = A_0 \\ s_2: \quad & \nu\frac{\partial A}{\partial n} = -H_t = J_s \end{aligned} \tag{3.1}$$

where A and J are the z components of $\bar{A}$ and $\bar{J}$, respectively. Ω is the domain of the region under consideration. s_1 and s_2 denote the Dirichlet boundary and Neumann boundary, respectively. The kind of inhomogeneous Neumann boundary condition will occur if surface current density J_s exists over the interface between the air sub-region and iron sub-region. Letting

$$\bar{B} = rot\bar{A} \tag{3.2}$$

The equivalent variational expression to the above class of nonlinear magnetic field problems can be written as

$$\begin{cases} W(A) = \iint_\Omega (\int_0^B \nu b\, db - JA)\, dx\, dy - \int_{s_2} J_s A\, ds = min. \\ s_1: \ A = A_0 \end{cases} \tag{3.3}$$

Details are given in Appendix B. The interpolating function is chosen to be a polynomial whose order depends on the number of nodes in each element. In view of the large amount of details and hence of the large number of elements required to describe the contour of the lamination and slots, it is convenient to choose triangular elements, each having three nodes coinciding with the vertices. The corresponding interpolating function is the linear polynomial:

$$A(x,\ y) = \alpha_1 + \alpha_2 x + \alpha_3 y \tag{3.4}$$

The coefficients α_1, α_2, α_3 may be found from the three simultaneous equations which are obtained by requiring the potential to assume vertex values A_i, A_j, A_m at the three vertices

$$\begin{aligned}
\alpha_1 &= \frac{1}{2\Delta}(a_i A_i + a_j A_j + a_m A_m) \\
\alpha_2 &= \frac{1}{2\Delta}(b_i A_i + b_j A_j + b_m A_m) \\
\alpha_3 &= \frac{1}{2\Delta}(c_i A_i + c_j A_j + c_m A_m)
\end{aligned} \tag{3.5}$$

where

$$\begin{array}{lll}
a_i = x_j y_m - y_j x_m; & a_j = x_m y_i - y_m x_i; & a_m = x_i y_j - y_i x_j; \\
b_i = y_j - y_m; & b_j = y_m - y_i; & b_m = y_i - y_j; \\
c_i = x_m - x_j; & c_j = x_i - x_m; & c_m = x_j - x_i;
\end{array}$$

and Δ represents the surface area of the triangle. By inserting Eqn. (3.5) into Eqn. (3.4), the interpolating function in terms of the values of A at the nodes can be expressed as follows:

$$A = N_i A_i + N_j A_j + N_m A_m \tag{3.6}$$

where

$$N_i = \frac{1}{2\Delta}(a_i + b_i x + c_i y)$$

$$N_j = \frac{1}{2\Delta}(a_j + b_j x + c_j y)$$
$$N_m = \frac{1}{2\Delta}(a_m + b_m x + c_m y) \tag{3.7}$$

are the so-called *shape function* at the node l ($l = i, j, m$).

Since the values of A and B are defined everywhere in terms of the value of A at the nodes, the minimization of the energy functional of Eqn. (3.3) is performed by setting the first derivative of the functional with respect to every node of A equal to zero so that

$$\frac{\partial W}{\partial \{A\}} = 0 \tag{3.8}$$

where $\{A\}$is the set of nodal vector potentials in region Ω. To achieve this minimization, it is convenient to separate the global energy functional into its element components W_e and to minimize one triangle at a time:

$$W = \sum_{e=1}^{E} W_e = \sum_{e=1}^{E} [\iint_{\Omega_e} (\int_0^B \nu b \, db - JA) \, dx \, dy - \int_{s_{2e}} J_s A \, ds] \tag{3.9}$$

where E is the total number of elements in region Ω. Equation (3.8) can now be rewritten as

$$\frac{\partial W}{\partial \{A\}} = \sum_{e=1}^{E} \frac{\partial W_e}{\partial \{A\}} = 0 \tag{3.10}$$

Introducing the value of W_e from Eqn. (3.10) and differentiating with respect to the nodal potential A_l gives

$$\begin{aligned} \frac{\partial W_e}{\partial \{A_l\}} &= \iint_{\Omega_e} (\frac{\partial}{\partial B} \int_0^B \nu b \, db \frac{\partial B}{\partial A_l} - J \frac{\partial A}{\partial A_l}) \, dx \, dy - \int_{s_{2e}} J_s \frac{\partial A}{\partial A_l} \, ds \\ &= \iint_{\Omega_e} (\nu B \frac{\partial B}{\partial A_l} - J \frac{\partial A}{\partial A_l}) \, dx \, dy - \int_{s_{2e}} J_s \frac{\partial A}{\partial A_l} \, ds \end{aligned} \tag{3.11}$$

Differentiation with respect to A_l clearly produces zero unless l is one of the nodes of the element e under consideration. Thus Eqn. (3.11) is an expression in only three

variables A_l. Realizing that B is constant throughout the element and assuming that J in the element and J_s along the Neumann boundary (including interface between two materials) of the element are also constant, one can obtain

$$\frac{\partial W_e}{\partial\{A_l\}}|_{l=i,j,k} = \frac{\partial}{\partial A_l}(\frac{1}{2}\nu B^2) - J\frac{\partial}{\partial A_l}\iint_{\Omega_e} A\,dx\,dy - J_s\frac{\partial}{\partial A_l}\int_{s_{2e}} A\,ds \tag{3.12}$$

Since A varies linearly over the triangle and assuming the Neumann boundary is defined by the side connecting node j and m, then

$$\iint_{\Omega_e} A\,dx\,dy = A_c\Delta \tag{3.13}$$

and

$$\int_{s_{\overline{jm}}} A\,ds = \frac{s_i}{2}(A_j + A_m) \tag{3.14}$$

where $A_c = \frac{1}{3}(A_i + A_j + A_m)$ is the centroid value of A in the element; s_i is the length of side $\overline{jm}$. Obtaining the partial derivative with respect to A_l yields

$$\begin{aligned}
\frac{\partial W_e}{\partial A_i} &= \frac{\nu}{4\Delta}[(b_i^2 + c_i^2)A_i + (b_ib_j + c_ic_j)A_j + (b_ib_m + c_ic_m)A_m] - \frac{J\Delta}{3} = 0 \\
\frac{\partial W_e}{\partial A_j} &= \frac{\nu}{4\Delta}[(b_ib_j + c_ic_j)A_i + (b_j^2 + c_j^2)A_j + (b_jb_m + c_jc_m)A_m] - \frac{J\Delta}{3} - \frac{J_ss_i}{2} = 0 \\
\frac{\partial W_e}{\partial A_m} &= \frac{\nu}{4\Delta}[(b_ib_m + c_ic_j)A_i + (b_jb_m + c_jc_m)A_j + (b_m^2 + c_m^2)A_m] - \frac{J\Delta}{3} - \frac{J_ss_i}{2} = 0
\end{aligned} \tag{3.15}$$

This set of equations can be written in matrix form as

$$[K_e]\{A_e\} = \{P_e\} \tag{3.16}$$

In order to obtain a corresponding discrete representation for the entire problem, it is only necessary to write one equation similar to Eqn. (3.16) for each and every

triangle in the grid. The resulting assembly of algebraic equations may then be combined as indicated in [38], to obtain a single matrix equation:

$$[K]\{A\} = \{P\} \tag{3.17}$$

Since any one node is connected to a limited number of other nodes only, the stiffness matrix $[K]$ is sparse with the nonzero terms bunched together along the diagonal. The stiffness matrix is also symmetrical, that is $[K] = [K]^t$. Finally, $[K]$ is positive definite. These properties are favourable to reduce the storage and use certain solution methods.

The nonlinearity of the problem is preserved, since $[K]$ depends not only on the shape and size of each triangle, but also on the reluctivity ν which depends on $\{A\}$. The most common method of solution to the system of nonlinear equations is the Newton-Raphson(N-R) algorithm which starts from an assumed value for the reluctivity ν and proceeds by means of iterations[38]. In each iteration ν is updated with respect to the $B - H$ characteristics of the materials.

3.2 Finite Element Model

In the following discussion, a 4-pole, 25 hp, interior-type PM motor will serve as an illustrative working model. Periodicity conditions are invoked to reduce the area of the motor to be discretized, one pole being sufficient in this case, as shown in the Fig. 3.1. The number of stator slots is 48 and the coil pitch is $1 - 11$. Individual phase windings A, B, and C are located in the stator slots with the axis of $A-$phase in alignment with the d-axis.

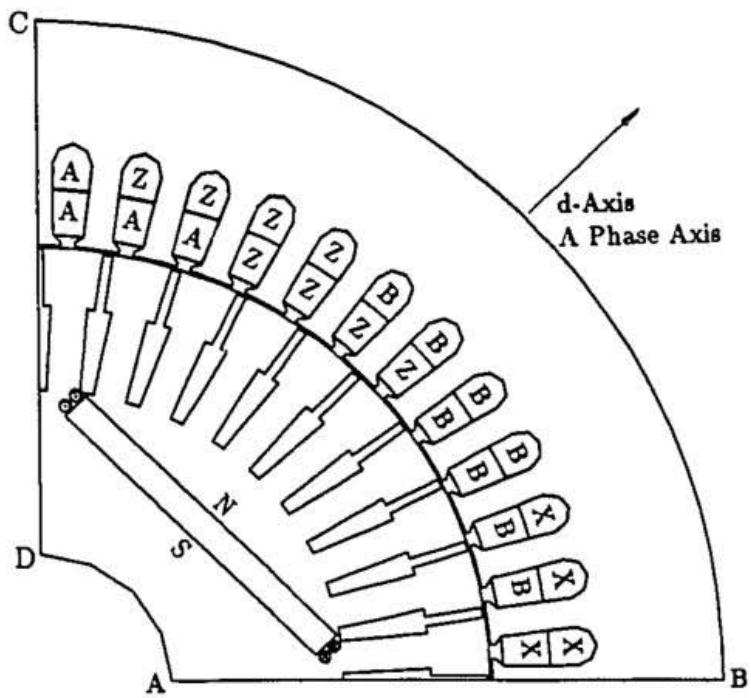

Figure 3.1: Cross section view of one pole of a 4-pole interior-type PM motor

Basic Assumptions

For two-dimensional finite element analysis of magnetostatic field, the following assumptions are made:

1. The magnetic field is contained in the geometry.
2. The magnetic field distribution inside the motor is constant along the axial direction and end effect is taken into account by the end leakage impedance.
3. The permanent magnet is represented by current density sheets.
4. The reluctivity is a unique function of the flux density, i.e. nonlinearity is allowed but not hysteresis.
5. Eddy currents in the iron are ignored.

Although the above assumptions are used in formulating the finite element analysis, assumption 4. and 5. are relaxed when calculating iron losses.

Modeling of Permanent magnet

Since modern permanent magnets, such as NdFeB and Samarium-Cobalt, have practically linear characteristics over the normal operating range, the recoil lines can be described as

$$\vec{B} = \mu(\vec{H} + \vec{H}_c) \tag{3.18}$$

where $\vec{H}$, $\vec{H}_c$ and μ are magnetic field intensity, coercive force and permeability, respectively. Then

$$\nabla \times \frac{1}{\mu}\vec{B} = \nabla \times \vec{H} + \nabla \times \vec{H}_c$$

$$= \vec{J} + \nabla \times \vec{H}_c \tag{3.19}$$

where $\vec{J}$ denotes the source current density. If $\vec{H}_c$ is considered as uniform within each element of the magnet, $\vec{H}_c$ may vary only across the element boundaries and thus the effect of permanent magnet can be replaced by a surface current surrounding the magnet element

$$\vec{J}_s = \nabla \times \vec{H}_c = -\vec{n} \times \vec{H}_c \tag{3.20}$$

where $\vec{n}$ is the unit normal pointing out of the element boundary. Particularly, in the case of uniform magnetization within the entire magnet, the surface current will exist only at the boundary between the magnet and the other materials. Hence, Eqn. (3.19) can be written in the form

$$\nabla \times \frac{1}{\mu}\vec{B} = \vec{J} + \vec{J}_s \tag{3.21}$$

This equation (3.21) implies that permanent magnets can be simply modeled as conducting current sheets surrounding a material having a permeability equal to the recoil permeability of the material.

Representation of the Armature MMF

A balanced three-phase system of currents in a balanced three-phase winding sets up a space magnetomotive force (MMF), the fundamental of which is constant in magnitude and rotates at a constant synchronous angular velocity. Let the currents be

$$\begin{cases} i_a = & I_m cos(\omega t + \beta) \\ i_b = & I_m cos(\omega t + \beta - 120°) \\ i_c = & I_m cos(\omega t + \beta - 240°) \end{cases} \tag{3.22}$$

where β is the phase angle at time zero. Since the stator MMF due to all phases is in alignment with the particular phase which is carrying the maximum current, it is convenient to choose the axis of phase A as a time-axis, as shown in the related time-space vector diagram of Fig. 2.3. In this case, the initial phase angle β of stator current $\dot{I}_1$ is also the space angle between the stator MMF, $\bar{F}_a$ and the rotor field MMF, $\bar{F}_f$. In addition, whichever particular instant is taken for consideration, it will make no difference due to MMF waves moving synchronously with the time vectors. Let $\omega t = 0$ in Eqn. (3.22), namely

$$\begin{cases} i_a = & I_m cos(\beta) \\ i_b = & I_m cos(\beta - 120°) \\ i_c = & I_m cos(\beta - 240°) \end{cases} \tag{3.23}$$

In such a case, the value of β in Eqn. (3.23) will be the space angle between the MMFs of stator and rotor. This will simulate different armature reactions under any load conditions. Two particular cases are taken as examples: i) $\beta = 0$ is d-axis reaction; ii) $\beta = 90°$ is characterized by q-axis reaction.

Boundary-value Problem

Since an equivalent current sheet approach, $\vec{J}_s = \vec{H}_c$ can be used to model the permanent magnets adequately, a field problem can be analyzed by using a vector potential function $\bar{A}$. For two-dimensional planar analysis, the vector $\bar{A}$ and source current density $\bar{J}$ contain only out-of-plane(Z-direction) components and thus act as scalar. Therefore, the boundary-value problem of a PM motor can be expressed as

$$\frac{\partial}{\partial x}(\nu \frac{\partial A}{\partial x}) + \frac{\partial}{\partial y}(\nu \frac{\partial A}{\partial y}) = -J$$

$$A|_{DA} = A|_{CB} = 0$$

$$A\,|_{AB} = -A|_{DC}$$

$$\nu \frac{\partial A}{\partial n}\Big|_l^+ - \nu \frac{\partial A}{\partial n}\Big|_l^- = H_c\,|_l = J_s \tag{3.24}$$

where l is the interface. The source current density J can be easily assessed according to Eqn. (3.23) for a given value of β corresponding to a specified load.

According to variational principle, the equivalent variational expression to the above class of nonlinear magnetic field problems can be written as

$$W(A) = \int \int_\Omega \left(\int_0^B \nu b\, db - JA\right) dx\, dy - \int_l J_s A\, dl = min$$

$$A\,|_{DA} = A|_{CB} = 0$$

$$A\,|_{AB} = -A|_{DC} \tag{3.25}$$

where $W(A)$ is the energy functional. The required solution to the field problem can be obtained by discretizing and further minimizing the energy function with respect to each of the nodal potentials as described in section 3.1.

3.3 Implementation with Current Source

In the case of a PM motor fed from current source, the implementation of finite element analysis is relatively straightforward under any prescribed set of currents in a machine. Different operating modes with a current source inverter can be simulated just by shifting the angle β between the stator and rotor MMFs in Eqn. (3.23). The angle β is also defined as the torque angle of a synchronous motor when fed from a current source, as the torque is a function of the angle β[39]. The whole torque characteristic of a PM motor can be obtained by varying the angle β from 0° to 180°. Fig. 3.2 shows a flow chart for evaluating the performance of

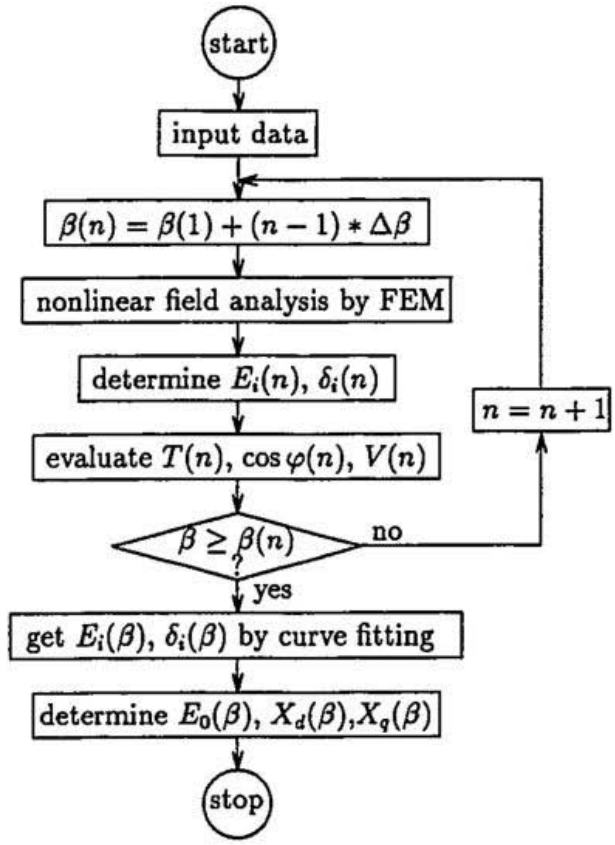

Figure 3.2: Flowchart for evaluating PM motor performance fed from current source

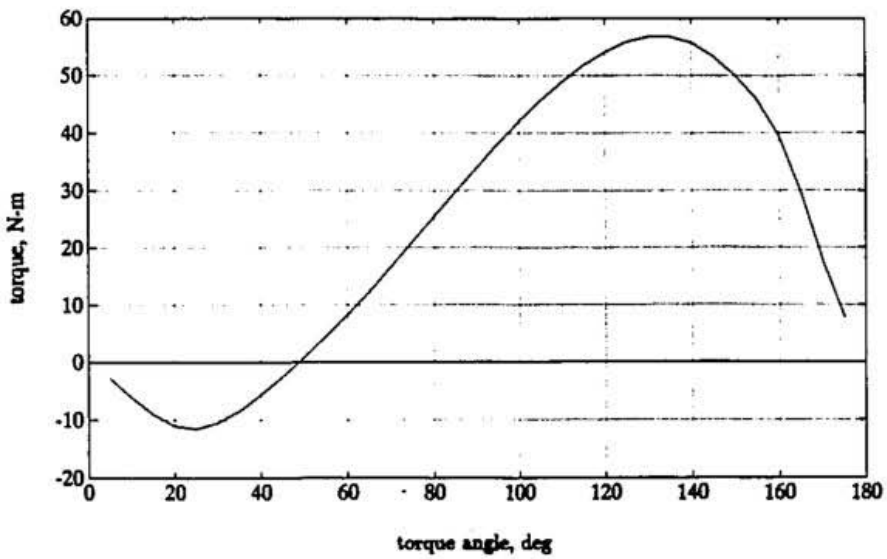

Figure 3.3: Torque characteristic with stator current $I_1 = 35A$

a PM motor fed from a current source. Fig. 3.3 contains the results of the torque versus torque angle characteristics of the model shown in Fig. 3.1 with constant stator current $I_1 = 35A$. It is to be noted that a PM synchronous motor drive fed from a current source inverter is usually operated under specific power factor in favour of proper thyristor commutation process. From Fig. 3.3 it is seen that there are two values of β which result in the same value of torque and hence power for the same speed. Therefore, before deciding on the strategies to be adopted it is important to know the operating region of the angle β positions. From the phasor diagram of Fig. 2.3, it is apparent that if β is less than 90°, the motor operates at a lagging power factor and the inverter used in the drive has to employ forced commutation. However, if β is greater than 90°, the motor operates at either a leading or lagging power factor. Since the motor may now operate at a leading power factor, it is possible to have a load commutated thyristor inverter system. In view of the fact that power factor angle is the result of the field solutions rather than the prescribed quantity, two approaches can be employed to obtain the simulation results corresponding to a specific power factor condition. One is searching for a particular angle β to satisfy the specific power factor by an iterative procedure. The other one is directed towards investigating a certain region which is sure to include that actual operating point by shifting the angle β sequentially from β_1 to β_n by incremental $\Delta\beta$ as shown in the flowchart of Fig. 3.2. The details for obtaining saturated parameters $E_0(\beta)$, $X_d(\beta)$ and $X_q(\beta)$ and performance quantities $T(\beta)$, $\cos(\beta)$, $V(\beta)$ will be described in the section 3.5.

It is also to be noted that the use of a value of torque angle greater than 90° may mean operation in the unstable part of the torque versus torque angle characteristic

as shown in Fig. 3.3. However, stable operation is possible because of the nature of the feedback which holds β constant.

3.4 Implementation with Voltage Source

In the case of a PM motor fed from voltage source, the implementation of finite element analysis is somewhat troublesome. The problem may be stated as follows: Given the supply voltage, determine the current in each winding, load angle and power factor as well as the torque at the prescribed terminal voltage condition.

For the same illustrative working model shown in Fig. 3.1, specifying the quantity of β in Eqn. (3.23) will lead to the setting of the identical value β of the space angle between the MMFs of the stator and rotor. This will effectively simulate different armature reactions under any load conditions so long as the amplitude of current, I_m, related to a specific load is determined. Of the two unknown variables, β and I_m in Eqn. (3.23), it is expedient to choose β as independent variable in connection with different load conditions. The reason is that the variable I_m is not a monotonical function of load angle δ, but β is. This argument can be verified as follows:

Referring to the phasor diagram Fig. 2.1, we have

$$\delta = \tan^{-1}\{\frac{I_1 \sin\beta X_q - I_1 \cos\beta r_1}{E_0 + I_1 \sin\beta r_1 + I_1 \cos\beta X_d}\} \tag{3.26}$$

The first derivative of Eqn. (3.26) with respect to β gives

$$\delta' = \frac{\partial\delta}{\partial\beta} = \frac{E_0(\cos\beta X_q + \sin\beta r_1) + I_1 X_d X_q + I_1 r_1^2}{\sec^2\delta\,(E_0 + I_1 \sin\beta r_1 + I_1 \cos\beta X_d)^2} \tag{3.27}$$

It can be seen that $\delta' \geq 0$ if $\beta \leq 90°$, and also $\delta' \geq 0$ when $\beta > 90°$ so long as

$$I_1 > \frac{E_0(|\cos\beta| X_q - \sin\beta r_1)}{X_d X_q + r_1^2} \tag{3.28}$$

For actual motor parameters, this requirement will be well satisfied. Therefore, β is a monotonically increasing function of power angle δ, and any value of β between 0° and 180° will represent a physical operation mode and assures a definite solution.

According to the phasor diagram of Fig. 2.6, the externally applied voltage $\dot{V}$ can be expressed as

$$\begin{aligned} \dot{V} &= -\dot{E}_0 + j\dot{I}_1\{X_{md}, X_{mq}\} + j\dot{I}'_1 x'_1 + r'_1 \dot{I}'_1 \\ &= -\dot{E}_i + j\dot{I}'_1 x'_1 + r'_1 \dot{I}'_1 \end{aligned} \tag{3.29}$$

where

$$\dot{I}_1 = I_d + jI_q = I_1 \angle\beta \tag{3.30}$$

$\dot{I}'_1$, r'_1 and x'_1 are defined by Eqns. (2.44) to (2.47) and $\dot{E}_i$ is the internal induced voltage due to resultant airgap flux. If a motor is powered by a voltage source inverter, x'_1 and r'_1 have to be used as equivalent circuit parameters to include the impact of the power switching elements. Referring to Eqns. (2.42), (2.47) and (2.48), and projecting the external voltage V on the d-axis and q-axis, one has

$$V_d = -\sin\delta_i E_i + I_1(r'_1\cos\beta - x'_1\sin\beta) - \frac{E_i}{r_c}\sin\delta_i r'_1 - \frac{E_i}{r_c}\cos\delta_i x'_1 \tag{3.31}$$

$$V_q = \cos\delta_i E_i + I_1(x'_1\cos\beta + r'_1\sin\beta) + \frac{E_i}{r_c}\cos\delta_i r'_1 - \frac{E_i}{r_c}\sin\delta_i x'_1 \tag{3.32}$$

and

$$V = \sqrt{V_d^2 + V_q^2} \tag{3.33}$$

The specification of the current I_1 (or $I_m = \sqrt{2}I_1$) related to a prescribed β for finite element analysis entails a special treatment, since the value of I_1 satisfying

Eqn. (3.33) is not available *apriori* until $\dot{E}_i$ is obtained from field solutions. Therefore, an iterative procedure is needed to cope with the problem. Since Newton-Raphson method converges rather rapidly, it is suitable to employ the Newton-Raphson algorithm to the iterative process. Making use of the following equations

$$E_i \cos\delta_i = E_0 + I_d X_{md} \tag{3.34}$$

$$E_i \sin\delta_i = I_q X_{mq} \tag{3.35}$$

The derivative of V with respect to I_1 will give

$$\begin{aligned} V'(I_1) &= \frac{1}{V}(V_d V_d' + V_q V_q') \\ &= \frac{1}{V}\{V_d[(-I_1 \sin\beta X_{mq})' + r_1' \cos\beta - x_1' \sin\beta] \\ &\quad + V_q[(E_0 + I_1 \cos\beta X_{md})' + x_1' \cos\beta + r_1' \sin\beta]\} \\ &= \frac{1}{V}\{V_d[(-E_i \sin\delta_i / I_1 + r_1' \cos\beta - x_1' \sin\beta] \\ &\quad + V_q[(E_i \cos\delta_i - E_0)/I_1 + x_1' \cos\beta + r_1' \sin\beta]\} \end{aligned} \tag{3.36}$$

where the prime indicates the operation of derivative. The current amplitude I_m for a specific angle β, therefore, is updated in each iteration as:

$$\begin{aligned} I_m^{(i+1)} &= I_m^{(i)} + \frac{1}{V'^{(i)}}(V_0 - V^{(i)}) \\ &= I_m^{(i)} + \Delta I_m \end{aligned} \tag{3.37}$$

where V_0 is the prescribed quantity, and $V^{(i)}$ and $V'^{(i)}$ are the calculated values based on the field solutions in the ith iteration loop under the current setting of $I_m^{(i)}$, that is

$$\begin{aligned} V^{(i)} = \{&[-E_i^{(i)} \sin\delta_i^{(i)} + I_1^{(i)}(r_1' \cos\beta - x_1' \sin\beta)]^2 \\ &+ [E_i^{(i)} \cos\delta_i^{(i)} + I_1^{(i)}(r_1' \sin\beta + x_1' \cos\beta)]^2\}^{1/2} \end{aligned} \tag{3.38}$$

and

$$V'^{(i)} = \frac{1}{V^{(i)}}\{V_d^{(i)}[(-E_i^{(i)}\sin\delta_i^{(i)}/I_1^{(i)} + r_1'\cos\beta - x_1'\sin\beta] + V_q^{(i)}[(E_i^{(i)}\cos\delta_i^{(i)} - E_0)/I_1^{(i)} + x_1'\cos\beta + r_1'\sin\beta]\} \quad (3.39)$$

as well as

$$r_c^{(i)} = \frac{3E_i^{2\,(i)}}{P_c^{(i)}} \quad (3.40)$$

where E_0 employs its open-circuit value, and it is to be noted that internal voltage $E_i^{(i)}$, internal load angle $\delta_i^{(i)}$, iron loss $P_c^{(i)}$ will be updated along with the adjusted value of I_m at each iteration. The details for obtaining these quantities will be given in the next section. This procedure will be repeated until the convergence criterion is satisfied

$$abs[(V_0 - V^{(i)})/V_0] \leq \varepsilon \quad (3.41)$$

As a result, the convergent value of current I_m will be the quantity truly related to a specific phase angle β. Using the same procedure, the value of $I_{m(n)}$, $E_{i(n)}$, $\delta_{i(n)}$ over its entire operating range can be obtained by setting different phase angle β, where the subscript n with parenthesis indicates each individual operating point.

For the Newton-Raphson iterative scheme to converge, however, it must begin from an initial value that is close to the correct one. This value of $I_{m(n)}^{(0)}$ can be determined in terms of the voltage equation (3.33) by inserting the updated parameters obtained from the solution of the last load condition.

In accordance with this scheme, it is advisable to investigate the whole range of operation step by step in such a regular way so that the current phase angle β has to be shifted sequentially from small to large value with the increase of load

angle δ or inverse. In such a case, the obtained initial value is fairly close to the final convergent value. Practical applications show that the obtained initial value in many cases is simply just the final convergent value. At the worst case, only a couple of iterations are needed to converge to its final values as shown in Fig. 3.4. Fig. 3.5 shows a flow chart for evaluating the synchronous performance of a PM motor with voltage source inverter supply throughout its operating range.

3.5 Parameter Determination and Performance Prediction

Accurate performance prediction, rather than the details of magnetic field distribution, is the final aim by finite element analysis. In this section, some schemes are proposed to extract the engineering information from the field solutions.

3.5.1 Parameters

Due to the saturation in the rotor and stator iron, the d-axis quantities and q-axis quantities are no longer independent of each other. For example, the q-axis path has a low reluctance and, as a result of q-axis armature reaction, may have a considerable effect on the saturation of the rotor pole tip and the magnetic bridge region between the rotor bar and the corners of magnet. This situation will also have an influence on the reluctance of the d-axis path and therefore cause a change in the magnet operating point and hence the field. However, the conventional method for obtaining saturated parameters, if expressed by its mathematical model, will be in the form

$$\begin{cases} E_0 = & f_1(I_f) = constant \\ X_d = & f_2(E_0, I_d) \\ X_q = & f_3(I_q) \end{cases} \tag{3.42}$$

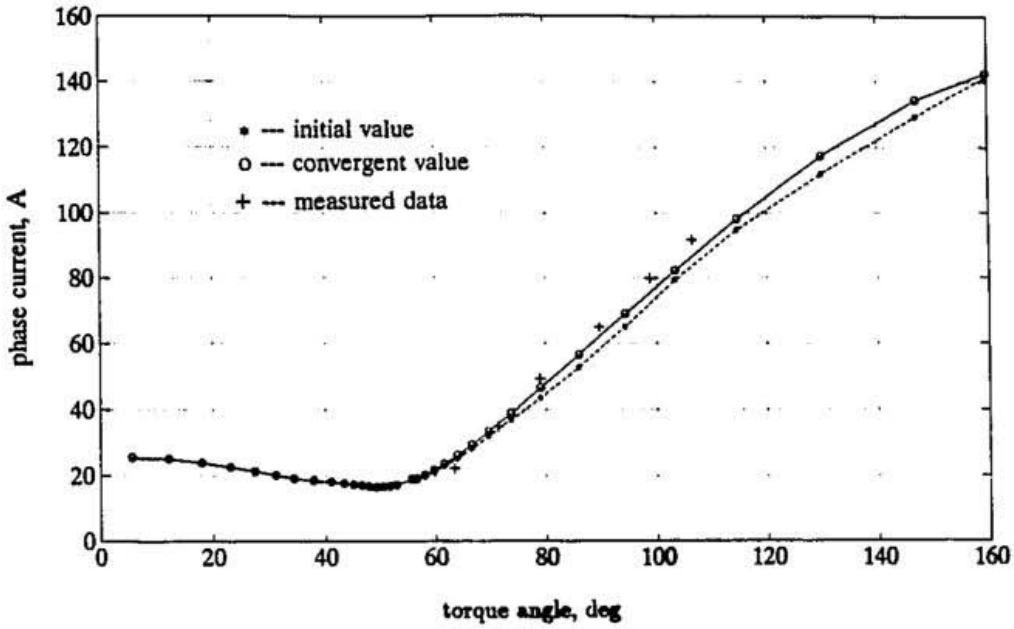

Figure 3.4: Comparison of estimated initial stator current with the convergent values and measured data

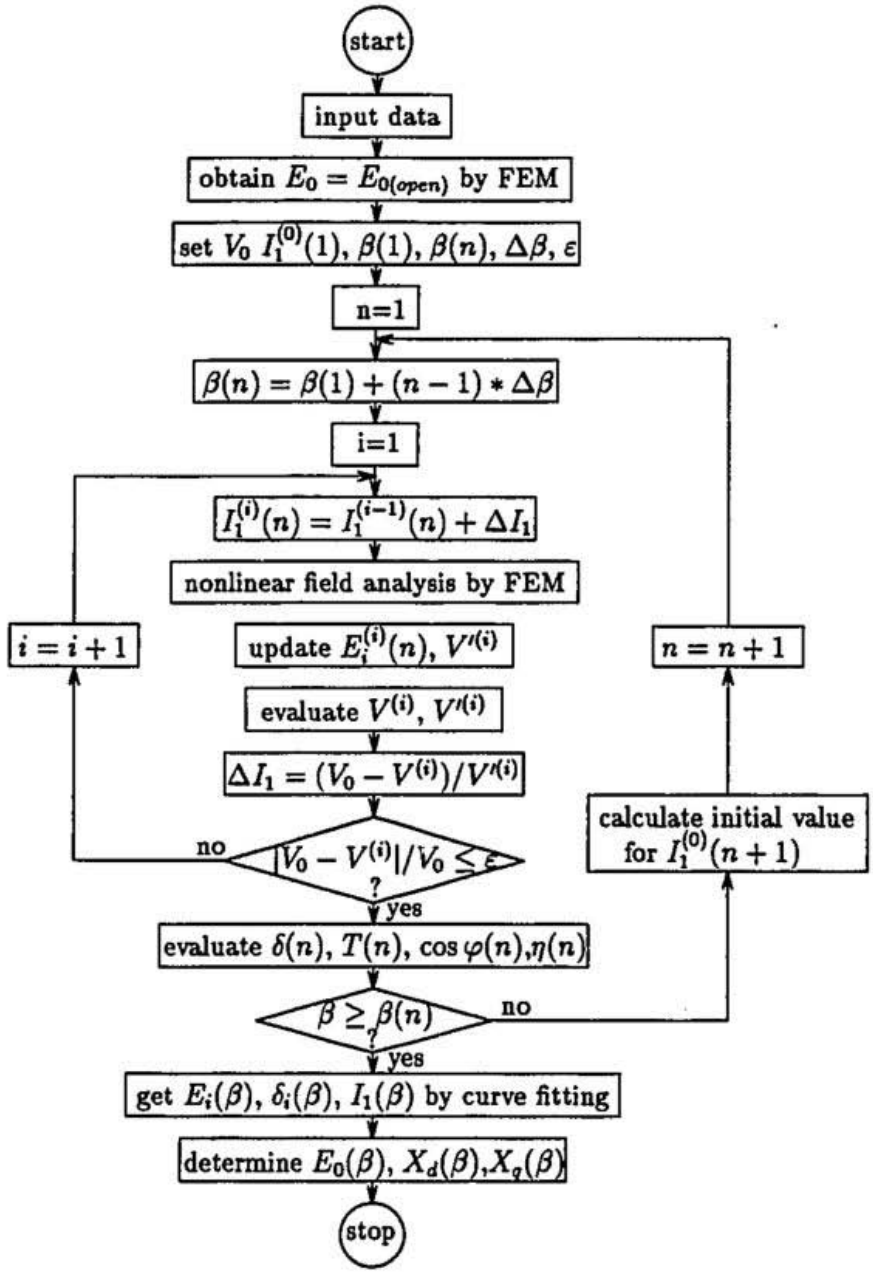

Figure 3.5: Flowchart for evaluating PM motor performance fed from voltage source

The limitations of the conventional method are:

- Excitation voltage E_0 produced by permanent magnets is unaffected by armature reactions.
- Effects of interaction between the d-axis and q-axis field on the value of the saturated parameters are not taken into account.

A proposed method, called the loading method, is applied to determine the saturated parameters[40]. Its mathematical model can be expressed as

$$\begin{cases} E_0 = & f_1(I_f, I_d, I_q) \\ X_d = & f_2(I_f, I_d, I_q) \\ X_q = & f_3(I_f, I_d, I_q) \end{cases} \tag{3.43}$$

It can be seen that this method enables the values of saturated parameters to conform to actual operating conditions. Unlike in equation (3.42), the parameters E_0, X_d and X_q in equation (3.43) are all influenced by the resultant load field due to the magnets and the d-axis and q-axis stator currents.

For the two-dimensional planar case, the value of the constant vector potential defines the flux paths. This argument can be mathematically proved. Assuming that Z is the direction of the current, the vector potential $\bar{A}$ has only one component in the Z-direction, denoted as A, and

$$\bar{B} = \nabla \times A = \frac{\partial A}{\partial y}\bar{i} - \frac{\partial A}{\partial x}\bar{j} \tag{3.44}$$

$$\nabla A = \frac{\partial A}{\partial x}\bar{i} + \frac{\partial A}{\partial y}\bar{j} \tag{3.45}$$

Since the dot product $\bar{B} \cdot \nabla A = 0$, it is clear that B is perpendicular to ∇A. It follows that the equipotential lines represent flux lines. Hence, both the d-axis and q-axis fundamental components of the flux in the airgap can be derived by

performing a Fourier analysis on the vector potentials A around the outer surface of the rotor. The cosine term coefficient a_1 represents the quantity of half the q-axis fundamental flux per pole (per unit depth) with respect to the analytical model of Fig. 3.1. The sine term coefficient b_1 represents the quantity of half the d-axis fundamental flux per pole (per unit depth). Obviously, the value of the resultant fundamental flux per pole is given by

$$\phi_m = 2l\sqrt{a_1^2 + b_1^2} \tag{3.46}$$

where l is the axial length of airgap. The inner torque angle is obtained by

$$\delta_i = \tan^{-1}(b_1/a_1) \tag{3.47}$$

This flux when rotating at synchronous speed induces a voltage E_i in each stator phase winding as

$$E_i = 4.44 f \phi_m N_s k_s K_{dp1} \tag{3.48}$$

where k_{dp1} is the fundamental winding factor and k_s is the skew slot factor; N_s is the series turns per phase; ϕ_m is the peak flux per phase. Referring to the phasor diagram shown in Fig. 2.3, the following can be obtained

$$E_i \cos\delta_i = E_0 + I_d X_{md} = E_0 + I_1 \cos\beta X_{md} \tag{3.49}$$

$$E_i \sin\delta_i = I_q X_{mq} = I_1 \sin\beta X_{mq} \tag{3.50}$$

From equation (3.50), the q-axis magnetizing reactance can be obtained as

$$X_{mq} = E_i \sin\delta_i / I_1 \sin\beta \tag{3.51}$$

It is to be noted that at different loads the armature reaction will change the saturation level of magnet flux path, and thus the excitation voltage E_0. Hence

in addition to Eqn. (3.49), another equation is needed to evaluate two unknown quantities, E_0 and X_{md}. To this end, a small displacement from the operating point is applied and the corresponding load field calculation is used to get the other equation similar to Eqn. (3.49) as

$$E_i' \cos \delta_i' = E_0 + I_1' \cos \beta X_{md} \tag{3.52}$$

The solution of the simultaneous algebraic Eqns. (3.49) and (3.52) should render these two saturated values for any operating point as

$$X_{md} = (E_i \cos \delta_i - E_i' \cos \delta_i')/(I_1 \cos \beta - I_1' \cos \beta') \tag{3.53}$$

and

$$E_0 = E_i \cos \delta_i - I_1 \cos \beta X_{md} \tag{3.54}$$

In fact, this approach does not demand extra field calculation. After the load field investigation covering the whole range of operation is carried out as discussed in the previous section, three curves $E_i(\beta)$, $\delta_i(\beta)$ and $I_1(\beta)$ can be obtained by the curve fitting scheme. As a result, for any particular operating point, the required information for both Eqns. (3.49) and (3.52) can be obtained by reading up the three ready-made curves. Practical application shows that this scheme not only simplifies the computation, but also offers satisfying results as long as the selected displacement point from the curves is not unreasonably too far from the chosen operating point.

Fig. 3.6 shows the calculated results of E_0, X_d and X_q for the working model. Note that at the torque angle around 37°, there is a dip on the E_0 curve and a crest on the X_d curve. This is due to the fact that, at the ferromagnetic bridge

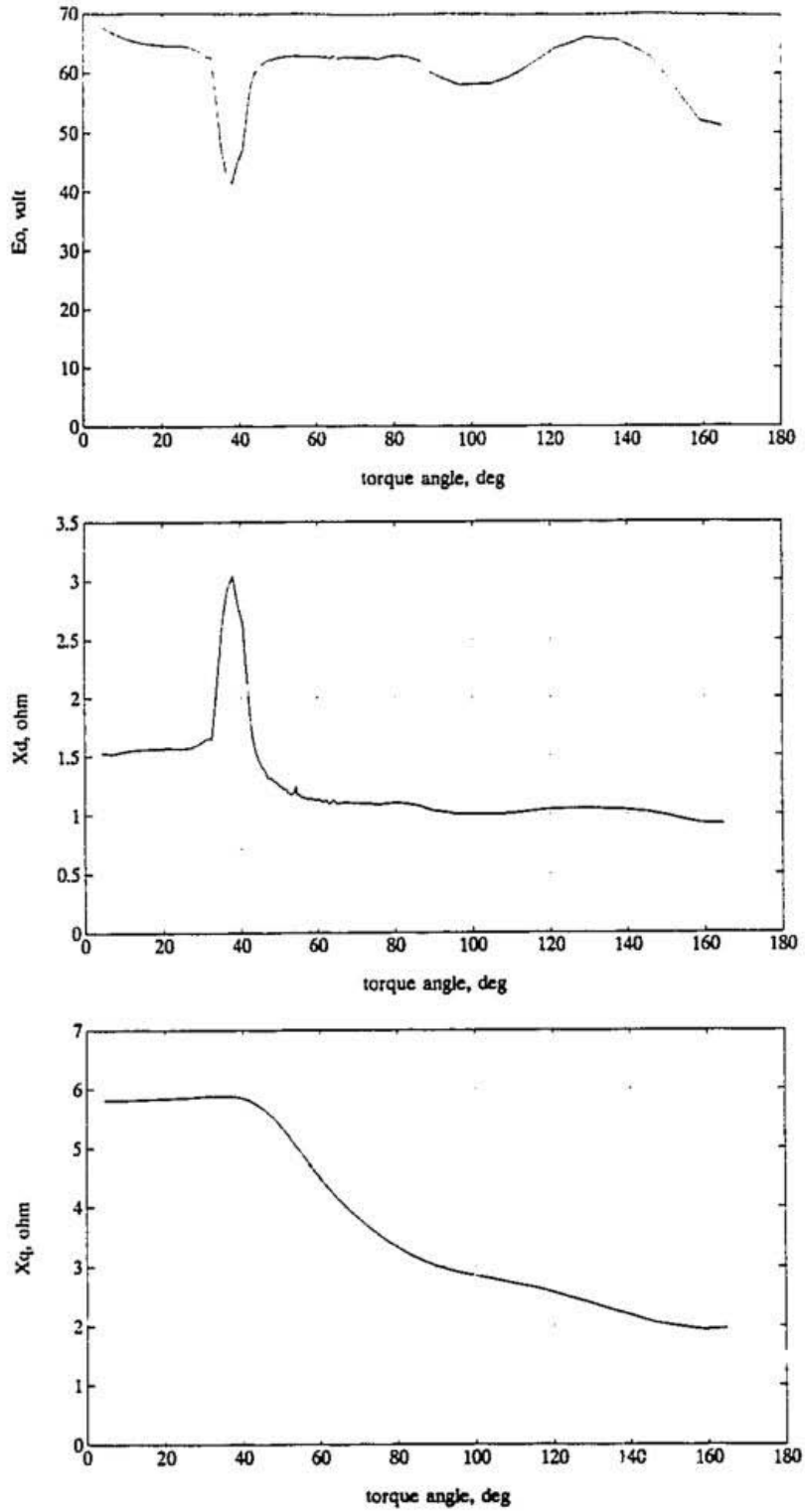

Figure 3.6: Variation of E_0, X_d and X_q with load angle δ

region between the rotor bar and the corners of magnet, the direction of the flux produced by the *magnetizing* armature reaction is opposite to the direction of the end leakage flux of the magnets. This is shown in Fig. 3.7 in which a programming technique is introduced to isolate the magnet component and the d-axis armature reaction component from the resultant loading fields. Thus, under certain load conditions, the bridge which is the main path of the magnet leakage flux becomes least saturated. As a result, the end leakage flux of the magnets increases rapidly. This leads to a dip on the E_0 curve. At the same time, due to the significant reduction of the magnet component of air-gap flux, the magnetic path for the d-axis component of armature reaction turns out to be much less saturated. Consequently, X_d increases notably.

3.5.2 Torque

For improved accuracy and being free of susceptibility to mesh discretization, the following flux method is proposed for torque calculation. The continuity of flux between elements is intrinsically fulfilled when using vector potential.

The electromagnetic power developed at the airgap can be found by mapping the I_d, I_q currents along the interior voltage E_i as:

$$P_e = mE_iI_1\cos(\delta_i + \frac{\pi}{2} - \beta) \tag{3.55}$$

Thus, the electromagnetic torque would be

$$T_e = \frac{m}{\omega}E_i(I_q\cos\delta_i - I_d\sin\delta_i) \tag{3.56}$$

By substituting equation (3.48) into equation (3.56), one can obtain the expression

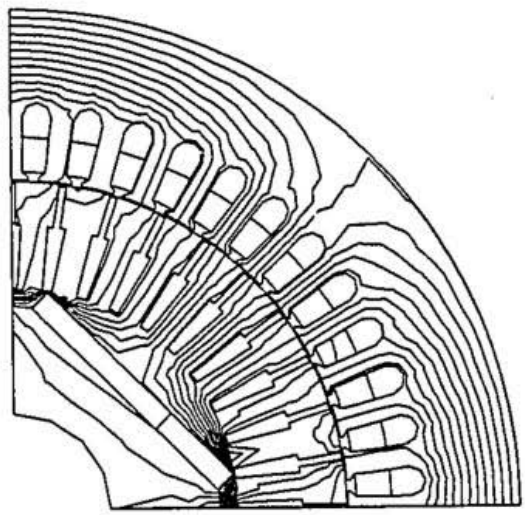

(a) d-axis component

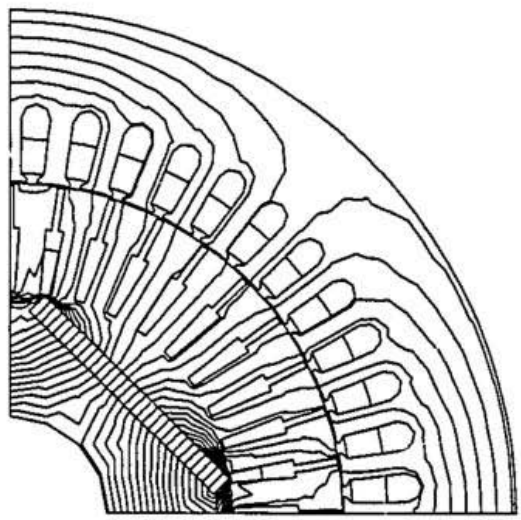

(b) magnet component

Figure 3.7: Flux distribution at $\delta = 37^o$

for the developed torque related to a specific load angle as:

$$T_{(n)} = \frac{mP}{\sqrt{2}} N_s k_s K_{dp1} \phi_{m(n)} \{ I_{1(n)} \sin \beta_{(n)} \cos \delta_{i(n)} - I_{1(n)} \cos \beta_{(n)} \sin \delta_{i(n)} \} \quad (3.57)$$

Thus, since the values of the flux ϕ_m and the torque angle δ_i have become available as discussed in the preceding section, it is possible to evaluate the torque of a PM motor using equation (3.57).

It is understandable that the calculated torque using Eqn. (3.57) is no longer susceptible to the mesh discretization. The reason for this can be linked to the fact that the solution accuracy of the vector potential at a certain point mainly rests on the global modeling, rather than the local feature around the concerned point as flux density does.

In fact, the use of the flux method for torque calculation of a PM motor can be theoretically interpreted as using virtual work principle (see Appendix C). However, from a practical point of view, the implementation of the flux method is more convenient and its results are more accurate. Fig. 3.8 shows the comparison of the torque characteristics between the simulated results and experimental values.

3.5.3 Eddy Current and Hysteresis Losses

Losses occur in the stator core when the magnetic field is alternating because of the hysteresis in the B-H magnetization cycle and because of eddy currents. In general, the losses per unit weight of laminations based on sinusoidally time varying flux density can be expressed as

$$P_{Fe} = c_1 f^2 B_p^2 + c_2 f B_p^\alpha = P_e + P_h \quad (3.58)$$

where B_p is the peak value of B and where the first term accounts for the eddy current loss and the second for the hysteresis loss. The frequency, f, is the fun-

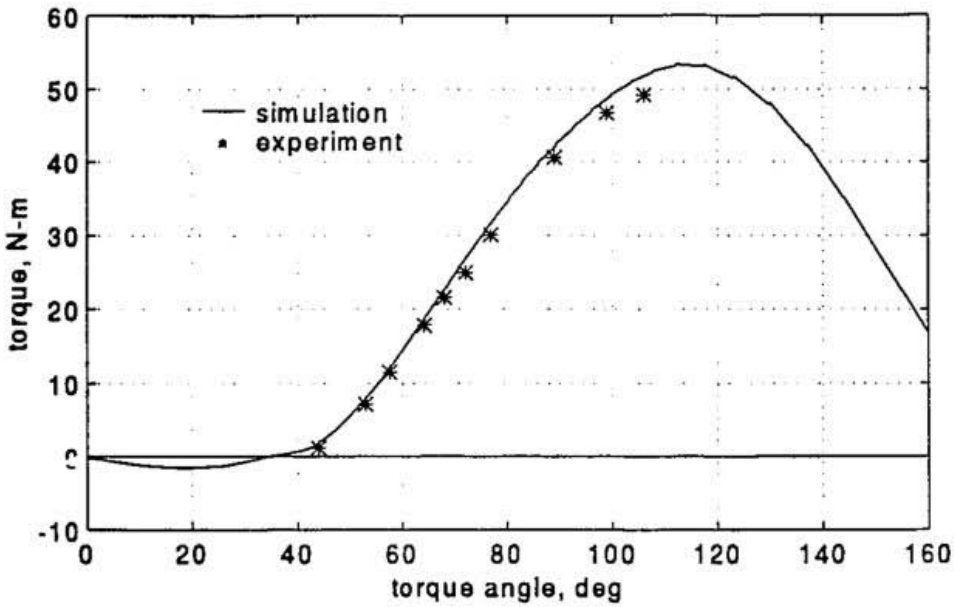

Figure 3.8: Simulated and measured torque characteristics

damental frequency of the waveform. The constants c_1, c_2 and α depend on the properties of the used material. Their values are available in related engineering handbooks.

Due to the nature of the magnetic fields in PM motors, flux density variations with time in many regions of the laminated stator core are not sinusoidal, but rather highly distorted waveforms with considerable harmonic contents. Under such a condition, it is advocated that actual time-varying flux density waveforms in various parts of the stator laminations are used to obtain a better evaluation of the core losses. Besides, it can be appreciated that a full cycle of the time-varying waveform of B in a certain point of the stator laminations can be appropriately simulated by a pole-period of its space distribution at an arbitrary instant. This space profile can be pictured in terms of the values of the flux density at those points which are located at the same radius as that of the point being investigated but with one-slot circumferential displacement in between. In fact, the notion of a point can be extended to an element because the value of B in each element has been regarded as constant when the triangle element is employed.

Based on the availability of those flux density profiles in each part of the stator core, the effects of distortion of the flux density waveforms on core losses are accounted for by introducing two correction factor k_e and k_h in Eqn. (3.58), associated to eddy current loss component and hysteresis loss component, respectively by the following equation:

$$P_{Fe} = k_e c_1 f^2 B_p^2 + k_h c_2 f B_p^{\alpha} \tag{3.59}$$

The determinations of these two factors are outlined as follows[41].

The Eddy Current Correction Factor k_e

For a distorted flux density profile as shown in Fig. 3.9, one can get the magnitudes of its fundamental and harmonics by a Fourier series expansion. Then the sinusoidal eddy current losses in stator laminations can be corrected for the effects of harmonic distortion by the following factor

$$k_e = (\frac{B_1}{B_p})^2 \sum_n (\frac{nB_n}{B_1})^2 \tag{3.60}$$

where B_1 denotes the magnitude of the fundamental flux density; B_n the magnitude of the nth flux density harmonic; B_p peak value of the distorted flux density waveform.

The Minor Loop Hysteresis Correction Factor k_h

Referring to Fig. 3.9, the occurrence of the reversals of magnitude ΔB_i, which is the magnitude of the i th flux reversal, results in the so-called minor hysteresis loops, and it is the contribution of the minor hysteresis loops that increases the hysteresis loss when the flux density waveform contains harmonics. Hence, the value of the sinusoidal hysteresis loss at the same B_p can be corrected for the effects of these minor loops by the following factor

$$k_h = 1 + 0.67 \frac{1}{B_p} \sum_n \Delta B_i \tag{3.61}$$

Equation (3.60) together with Eqn. (3.61) will provide a practical means of estimating the losses in the lamination under distorted flux mode. Due to the duplication of geometric structure and the characteristics of rotating magnetic field, it is feasible to find out only those element values over one slot pitch and then sum

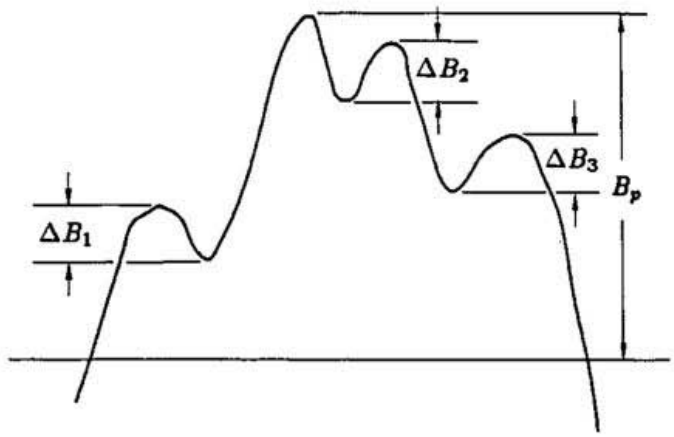

Figure 3.9: Distorted flux density profile

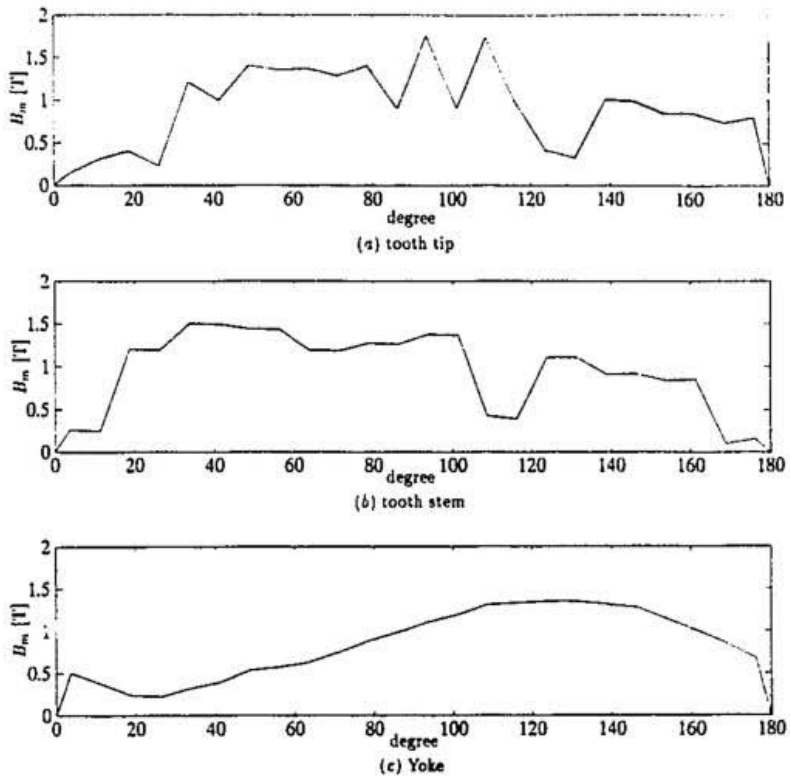

Figure 3.10: Flux density profiles in tooth tip, tooth stem and yoke elements

them. The total core losses of the entire stator can further be figured out from the summed value multiplied by the number of stator slots.

As stated above, the flux density profile varying with time for a particular element can be described by the corresponding spatial distribution waveform. Three of the flux density profiles are given in Fig. 3.10 for those elements located in the tooth tip, tooth stem, and yoke regions, respectively. Notice that all of these profiles are highly distorted and non-sinusoidal.

For the illustrative model with voltage source supply, the calculated correction factors k_e and k_h under the rated conditions are given in Table-1. It is obvious from the table that the effect of distorted flux density waveforms on the core losses should not be neglected.

Table-1

Correction Factors for Core Losses

element	k_e	k_h
tooth tip	8.176	2.088
tooth stem	6.874	1.630
yoke	3.868	1.141

3.5.4 Power Factor and Efficiency

Once the values of E_i, δ_i, I_1, I_c, P_c are available from the field solutions for a certain β, the corresponding power factor at this operating point can be determined by

$$\cos\varphi = \cos\{\tan^{-1}(-V_d/V_q) + \pi/2 - \beta'\} \tag{3.62}$$

where β' is the phase angle of $\dot{I}_1'$, namely

$$\dot{I}_1' = I_1 \angle\beta + I_c \angle(\delta_i + \pi/2) \tag{3.63}$$

and

$$I_c = P_c/3E_i \tag{3.64}$$

Fig. 3.11(a) shows the simulation results of power factor for the current source case with $I_1 = 35A$. Fig. 3.11(b) contains the simulation and measured results of power factor for the voltage source case with $V = 110$V.

At this stage, the overall efficiency at any operating point can be easily determined as follows

$$\eta = \frac{P_2}{P_1} = \frac{E_i I_1 \cos(\delta_i + \pi/2 - \beta) - P_{fw}}{V I_1' \cos\varphi} \tag{3.65}$$

where the mechanical losses P_{fw} due to friction and windage are obtained by the following conventional expression[42]

$$P_{fw} = 16P(\frac{v_t}{4})^3\sqrt{\frac{l_s}{19}}\ \text{W} \tag{3.66}$$

where P is the number of pole pairs; l_s the length of machine bore and v_t the rotor peripheral velocity.

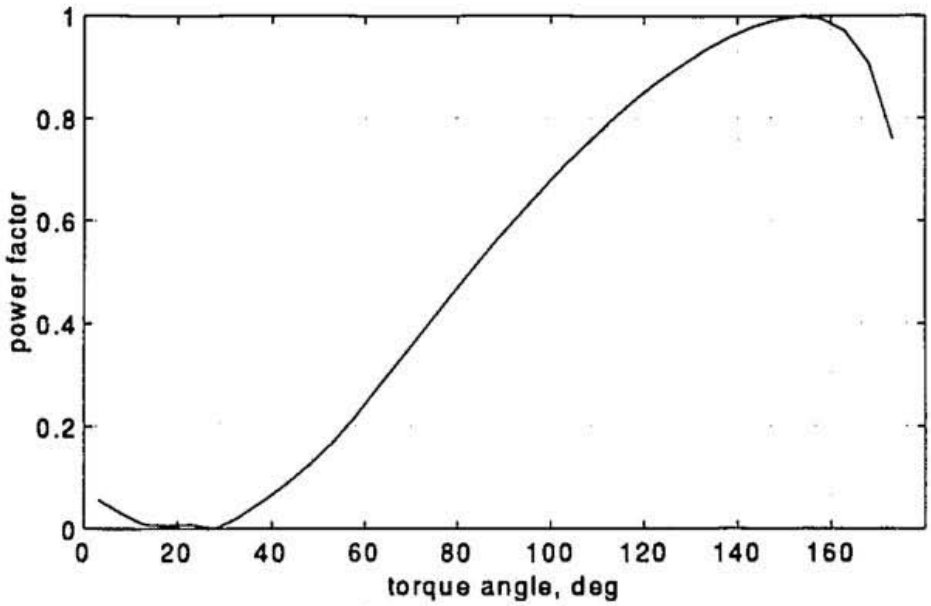

(a) current source case

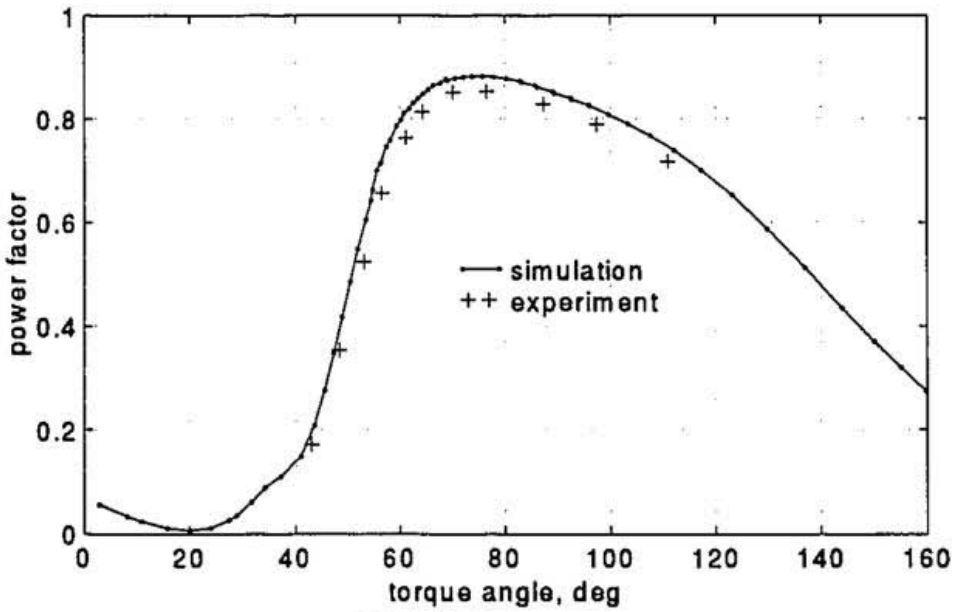

(b) voltage source case

Figure 3.11: Power factor characteristics

Chapter 4

Simulation of Starting Performance

The strategy of field-circuit combined analysis for starting process will be discussed in this chapter. The correct assessment of starting behaviour lies in how to extract accurate transient parameters from the eddy-current field solutions. As a necessary first step, it is imperative to develop appropriate finite element formulae for two-dimensional nonlinear eddy-current field problems.

4.1 Nonlinear Eddy-current Finite Element Model with Current source

As mentioned in the previous chapter, in order to avoid a large amount of field calculations, as encountered when using a time-stepping procedure, time-phasor is introduced to obtain nonlinear eddy-current field calculation so that finite element analysis can be independent of time factor. First, we investigate the relatively simple case with current source supply, and then proceed to the tough case with voltage source supply.

4.1.1 Assumptions

For two-dimensional finite element analysis of nonlinear eddy-current field, the following assumptions are made:

1. Displacement currents are neglected.
2. The hysteresis of solid iron is neglected.
3. Eddy currents are assumed present only in the rotor bar.
4. Material conductivity is assumed constant.
5. The rotor end-ring resistance is represented by modification of the rotor bar conductivity; the rotor end-ring leakage flux effect is represented by the end-ring leakage reactance.

4.1.2 Boundary-value Problem

The same physical model as applied in magnetostatic field analysis in Fig. 3.1 is used as an illustrative example. Subject to the above assumptions and in terms of Maxwell's equations, the following equation holds

$$\frac{\partial}{\partial x}(\nu\frac{\partial A}{\partial x}) + \frac{\partial}{\partial y}(\nu\frac{\partial A}{\partial y}) = -J + \sigma\frac{\partial A}{\partial t} \tag{4.1}$$

where A is the z-component of the magnetic vector potential; ν is the reluctivity; J is the source-current density; σ is the conductivity and t is the time.

If the higher harmonics of the magnetic vector potential are neglected, and the rotor is considered as pseudo-stationary, the sources and the magnetic vector potential can be assumed to vary sinusoidally with time. The field and its source

may, therefore, be conveniently represented by the use of complex numbers. Thus, the time variation of A and J can be expressed as time phasor $\dot{A}$ and $\dot{J}$, so that Eqn. (4.1) together with boundary conditions can be rewritten as

$$\frac{\partial}{\partial x}(\nu\frac{\partial \dot{A}}{\partial x}) + \frac{\partial}{\partial y}(\nu\frac{\partial \dot{A}}{\partial y}) = -\dot{J} + j\omega_r\sigma\dot{A}$$

$$\dot{A}\Big|_{DA} = \dot{A}\Big|_{CB} = 0$$

$$\dot{A}\Big|_{AB} = -\dot{A}\Big|_{DC} \tag{4.2}$$

where ω_r is the angular slip frequency. It is to be noted that the introduction of time-phasor requires the reluctivity to be constant throughout the time cycle. However, since the reluctivity will vary non-linearly with magnetic flux density

$$\nu = \nu[B(t)] \tag{4.3}$$

time factor still exists in Eqn. (4.2); and therefore, it can not be solved directly. For this reason, the concept of equivalent reluctivity ν_e is introduced to handle this difficulty.

4.1.3 Equivalent Reluctivity

It is desirable to make equivalent reluctivity ν_e to be only a function of amplitude of magnetic flux density in one periodic time for the lamination material, that is

$$\nu_e = \nu_e[B_m] \tag{4.4}$$

Consequently, the equivalent magnetic field intensity H_e can be expressed as

$$H_e = \nu_e B_m \tag{4.5}$$

Equivalent reluctivity ν_e may be appropriately determined in terms of equivalent magnetic energy. The magnetic energy density w_m for the medium can be expressed as

$$w_m = \frac{1}{2}\nu\, B^2(t) \tag{4.6}$$

Corresponding to equivalent reluctivity, the equivalent magnetic energy density w_{me} is defined as

$$w_{me} = \frac{1}{2}\nu_e\, B^2(t) \tag{4.7}$$

The square difference $D(\nu_e)$ between w_m and w_{me} in one periodic time is

$$D(\nu_e) = \int_0^T (w_m - w_{me})^2\, dt \tag{4.8}$$

Thus, equivalent reluctivity can be determined by minimizing $D(\nu_e)$. Making the first derivative of Eqn. (4.8) with respect to ν_e be equal to zero yields

$$\nu_e = \frac{\int_0^T \nu B^4(t)\, dt}{\int_0^T B^4(t)\, dt} = \frac{\int_0^T H(t)B^3(t)\, dt}{\int_0^T B^4(t)\, dt} \tag{4.9}$$

It is worthwhile noting that, although, both the magnetic flux density in x direction B_x and in the y direction B_y at each point of the field domain vary sinusoidally with time respectively, the initial phase angles generally are different. Let

$$B_x = B_1 \sin(\omega t + \varphi_1) \tag{4.10}$$

and

$$B_y = B_2 \sin(\omega t + \varphi_2) \tag{4.11}$$

As a result, the locus of their resultant in $x - y$ plane is an ellipse, as it varies with time, and it can be expressed as (see Appendix D)

$$B(t) = a\sqrt{\frac{1}{2}\{1 + (\frac{b}{a})^2 - [1 - (\frac{b}{a})^2]\cos 2\omega t\}} \tag{4.12}$$

where a denotes the major axis of the ellipse and also represents the amplitude B_m of $B(t)$, that is

$$a = \{\frac{1}{2}[B_1^2 + B_2^2 + \sqrt{B_1^4 + B_2^4 + 2B_1^2 B_2^2 \cos 2(\varphi_2 - \varphi_1)}]\}^{1/2} = B_m \tag{4.13}$$

and b denotes the minor axis

$$b = \{\frac{1}{2}[B_1^2 + B_2^2 - \sqrt{B_1^4 + B_2^4 + 2B_1^2 B_2^2 \cos 2(\varphi_2 - \varphi_1)}]\}^{1/2} \tag{4.14}$$

If $\varphi_1 = \varphi_2 = \varphi$, then $(b/a) = 0$ and Eqn. (4.12) becomes

$$B(t) = \sqrt{B_1^2 + B_2^2}\sin(\omega t + \varphi) \tag{4.15}$$

and the ellipse degenerates to a line.

If $\varphi_1 = \varphi_2 \pm \pi/2$ and $B_1 = B_2$, then $b/a = 1$ and Eqn. (4.12) becomes

$$B(t) = B_1 + B_2 \tag{4.16}$$

and the ellipse becomes a circle.

Up to now, even though it is possible to evaluate equivalent reluctivity in terms of Eqn. (4.12), the amount of computing burden for real time computation directly using Eqn. (4.12) will be formidable. Therefore, an alternative way is recommended such that three typical equivalent magnetization curves relating the amplitude of flux density B_m to the equivalent magnetic field intensity H_e are prepared before hand. Using these three equivalent magnetization curves which are intentionally chosen at $(b/a) = 0$, 0.5, and 1.0 respectively, the equivalent reluctivity ν_e corresponding to any B_m with other (b/a) values can be determined by parabolic interpolation.

In the first case of $(b/a) = 0$, substituting Eqns. (4.15) and (4.9) into Eqn. (4.5), the formula for computing equivalent magnetic field intensity H_e as a function of the amplitude of flux density B_m, can be obtained

$$H_e(B_m) = \frac{16}{3\pi} \int_0^{\frac{\pi}{2}} H \sin^3 t \, dt \tag{4.17}$$

It is to be noted that integrand H is the function of $B = B_m \sin t$, described by the fundamental magnetization curve of the material and Eqn. (4.17) may involve a numerical integration.

For obtaining the equivalent magnetization curve corresponding to $(b/a) = 0.5$, the formula for computing equivalent magnetic field intensity can be obtained from Eqns. (4.5), (4.9) and (4.12) as,

$$H_e(B_m) = \frac{256}{59\pi} \int_0^{\frac{\pi}{2}} H(0.625 - 0.375 \cos 2t)^{1.5} \, dt \tag{4.18}$$

where integrand H is the function of $B = \sqrt{0.625 - 0.375 \cos 2t}$.

In the case of $(b/a) = 1.0$, flux density turns to be a constant, $B(t) = B_m$. As a result, the equivalent magnetization curve is just the fundamental magnetization curve.

From these three previously obtained equivalent magnetization curves, the equivalent reluctivity ν_e corresponding to any B_m with other (b/a) values can be easily determined by parabolic interpolation.

4.1.4 Variational Formulation

Due to the introduction of equivalent reluctivity ν_e, the boundary-value problem in Eqn. (4.2) can thus be expressed as

$$\frac{\partial}{\partial x}(\nu_e \frac{\partial \dot{A}}{\partial x}) + \frac{\partial}{\partial y}(\nu_e \frac{\partial \dot{A}}{\partial y}) = -\dot{J} + j\omega_r \sigma \dot{A}$$

$$\dot{A}\Big|_{DA} = \dot{A}\Big|_{CB} = 0$$
$$\dot{A}\Big|_{AB} = -\dot{A}\Big|_{DC} \tag{4.19}$$

Multiply each term of first equation of Eqn. (4.19) by the first variation $\delta\dot{A}$ of vector potential $\dot{A}$, and then the integration is performed over entire region Ω,

$$\iint_\Omega [\frac{\partial}{\partial x}(\nu_e \frac{\partial \dot{A}}{\partial x}) + \frac{\partial}{\partial y}(\nu_e \frac{\partial \dot{A}}{\partial y})]\, \delta\dot{A}\, dx\, dy = -\iint_\Omega \dot{J}\, \delta\dot{A}\, dx\, dy + \iint_\Omega j\omega_r \sigma \dot{A}\, \delta\dot{A}\, dx\, dy \tag{4.20}$$

Applying Green's theorem and following the same manipulation as in the case of magnetostatic problems (see Appendix B), one obtains

$$\iint_\Omega \nu_e \dot{B}\, \delta\dot{B}\, dx\, dy - \iint_\Omega \dot{J}\, \delta\dot{A}\, dx\, dy + \iint_\Omega j\omega_r \sigma \dot{A} \delta\dot{A}\, dx\, dy - \int_{s2} \dot{J}_s \delta\dot{A}\, ds = 0 \tag{4.21}$$

The left of Eqn. (4.21) can be viewed as the first variation δW of the functional W, and thus the equivalent variational problem is given by

$$W(\dot{A}) = \iint_\Omega (\int_0^{B_m} \nu_e b\, db)\, dx\, dy - \iint_\Omega \dot{J}\dot{A}\, dx\, dy + \frac{1}{2}\iint_\Omega j\omega_r \sigma \dot{A}^2\, dx\, dy - \int_{s2} \dot{J}_s \dot{A}\, ds = \min$$

$$\dot{A}\Big|_{DA} = \dot{A}\Big|_{CB} = 0$$

$$\dot{A}\Big|_{AB} = -\dot{A}\Big|_{DC} \tag{4.22}$$

4.1.5 Discretization and Functional Minimization

The equivalent variational problem of nonlinear eddy current field is formally identical to Eqn. (3.25) for nonlinear magnetostatic field problem except the integration term $\frac{1}{2}\iint_\Omega j\omega\sigma\dot{A}^2\, dx\, dy$. For the sake of simplicity, of all terms of the element energy functional only the following term needs to be considered in the discretization process

$$W_e^*(\dot{A}) = \iint_{\Omega_e} \frac{1}{2} j\omega_r \sigma \dot{A}^2\, dx\, dy \tag{4.23}$$

Differentiating with respect to the nodal potential $\dot{A}_l$ $(l = i, j, m)$ gives

$$\frac{\partial W_e^*}{\partial \dot{A}_l} = \iint_{\Omega_e} j\omega_r \sigma \dot{A} \frac{\partial \dot{A}}{\partial \dot{A}_l}\, dx\, dy \tag{4.24}$$

Introducing interpolating function in terms of the vertex values of $\dot{A}$

$$\dot{A} = N_i \dot{A}_i + N_i \dot{A}_j + N_j \dot{A}_m \tag{4.25}$$

where shape function N_i, N_j, N_m are defined by Eqn. (3.7). Eqn. (4.24) becomes

$$\frac{\partial W_e^*}{\partial \dot{A}_l} = \iint_{\Omega_e} j\omega_r \sigma (N_i \dot{A}_i + N_i \dot{A}_j + N_j \dot{A}_m) N_l\, dx,\, dy \quad (l = i, j, m) \tag{4.26}$$

Eqn. (4.26) reduces after some algebraic manipulation to the form

$$\begin{aligned}
\frac{\partial W_e^*}{\partial \dot{A}_i} &= j\omega_r \sigma \frac{\Delta}{12}(2\dot{A}_i + \dot{A}_j + \dot{A}_m) \\
\frac{\partial W_e^*}{\partial \dot{A}_j} &= j\omega_r \sigma \frac{\Delta}{12}(\dot{A}_i + 2\dot{A}_j + \dot{A}_m) \\
\frac{\partial W_e^*}{\partial \dot{A}_j} &= j\omega_r \sigma \frac{\Delta}{12}(\dot{A}_i + \dot{A}_j + 2\dot{A}_m)
\end{aligned} \tag{4.27}$$

Superimposing the results of Eqn. (4.27) into Eqn. (3.15), the minimization of the energy function over a single element results in the elemental equation

$$([K_e] + j\omega_r [H_e])\{\dot{A}_e\} = \{\dot{P}_e\} \tag{4.28}$$

where

$$[K_e] = \frac{\nu_e}{4\Delta} \begin{bmatrix} b_i b_i + c_i c_i & b_i b_j + c_i c_j & b_i b_m + c_i c_m \\ & b_j b_j + c_m c_m & b_j b_m + c_j c_m \\ SYM & & b_m b_m + c_m c_m \end{bmatrix} \tag{4.29}$$

$$[H_e] = \frac{\sigma \Delta}{12} \begin{bmatrix} 2 & 1 & 1 \\ 1 & 2 & 1 \\ 1 & 1 & 2 \end{bmatrix} \tag{4.30}$$

and

$$\{\dot{P}_e\} = \{\ \tfrac{j\Delta}{3} \quad \tfrac{j\Delta}{3} + \tfrac{j_s s_i}{2} \quad \tfrac{j\Delta}{3} + \tfrac{j_s s_i}{2}\ \}^t \tag{4.31}$$

By assembling the individual element contribution described by Eqn. (4.28), the overall system equations are constructed in the matrix form

$$([K] + j\omega_r[H])\{\dot{A}\} = \{\dot{P}\} \tag{4.32}$$

Eqn. (4.32) represents the finite element discretization of the nonlinear eddy-current problem with current source described by Eqn. (4.19). Since these matrix equations are nonlinear, they are first quasi-linearized, and then are solved by the Gaussian elimination procedure. The quasi-linearization of the nonlinear complex matrix equation (4.32) is achieved by an iteratively convergent process.

4.2 Nonlinear Eddy-current Finite Element Model with Voltage Source

For voltage source supply, the current density $\dot{J}$ is unknown before field solutions are available. In such a case, a flux distribution from a finite-element nonlinear eddy-field solutions, based on any assumed set of currents in the machine, can be used to determine induced voltages in various windings. In general, the impressed voltage from the voltage source inverter will not balance with the sum of the induced voltage and impedance voltage drops. The lack of balance is usually used to obtain an improved estimate of the correct current set, and to proceed in an iterative manner until satisfactory balance is achieved. In this study, a finite element model directly starting with the voltage source will be derived to eliminate the iterative process[43].

From the discussion of the last section, due to the introduction of both phasor vector potential $\dot{A}$ and equivalent reluctivity ν_e, the boundary-value problem can

be expressed as

$$\frac{\partial}{\partial x}(\nu_e \frac{\partial \dot{A}}{\partial x}) + \frac{\partial}{\partial y}(\nu_e \frac{\partial \dot{A}}{\partial y}) = -\dot{J} + j\omega_r \sigma \dot{A}$$

$$\dot{A}\Big|_{DA} = \dot{A}\Big|_{CB} = 0$$

$$\dot{A}\Big|_{AB} = -\dot{A}\Big|_{DC} \tag{4.33}$$

Since the current density $\dot{J}$ is unknown before field solutions are available, as a much better alternative to usually adopted iterative process, an approach which combines field quantities with electrical circuit equations is employed to tackle this problem.

The induced electromotive forces in stator winding may well be evaluated on a coil-by-coil basis. The average value of the induced voltage, e_c, over a coil side of cross-sectional area s_c, is given by Faraday's law

$$e_c = -N_1 l_{ef} \frac{1}{s_c} \int_{S_c} \frac{\partial A}{\partial t}\, ds = -j\omega N_1 l_{ef} (\frac{1}{s_c} \int_{s_c} \dot{A}\, ds) \tag{4.34}$$

where the average value of phasor vector potential in the bracket represents the average flux linkage over a coil side per turn per length; ω is the angular frequency of voltage source; s_c is half the value of the slot area for two-layer windings, or just the value of the whole slot area for single-layer windings. In numerical field calculation, the average value of phasor vector potential can be expressed as

$$\frac{1}{s_c} \int_{s_c} \dot{A}\, ds = \frac{1}{s_c} \sum_{i=1}^{n_e} \int_{\Delta_i} \dot{A}_i\, ds = \frac{\sum_{i=1}^{n_e} \Delta_i \sum_{j=1}^{3} \dot{A}_{ij}}{3 s_c} \tag{4.35}$$

where the summation for i ranges over all the elements n_e in the area s_c, and

$$\int_{\Delta_i} \dot{A}_i\, ds = \frac{\Delta_i}{3} \sum_{j=1}^{3} \dot{A}_{ij} \tag{4.36}$$

Consequently, Eqn. (4.34) is rewritten as

$$e_c = -j\omega N_1 l_{ef}\left(\frac{\sum_{i=1}^{n_e}\Delta_i \sum_{j=1}^{3}\dot{A}_{ij}}{3s_c}\right) \tag{4.37}$$

Depending upon the details of the discretization and the connections of the phase windings, the back EMF induced in phase A winding is given as

$$\dot{E}_A = -j\frac{\omega N_1 l_{ef} 2P}{3s_c a_1}\{D\}_A^t\{\dot{A}\} \tag{4.38}$$

where P is the number of pole pairs, a_1 number of parallel circuits in windings; $\{D\}_A^t = \{d_{A1}, ..., d_{Ak}, ..., d_{An}\}$ is the area vector related to all the nodes in the sub-region of phase A winding. The definition of any one component d_{Ak} is given by

$$d_{Ak} = \sum_{e=1}^{E_k}\Delta_{ke} \tag{4.39}$$

where Δ_{ke} denotes the area of element e, one of whose vertices is just the numbered node k. E_k is the number of total elements related to node k.

Similarly, the back EMF induced in phase B and phase C can be expressed as

$$\dot{E}_B = -j\frac{\omega N_1 l_{ef} 2P}{3s_c a_1}\{D\}_B^t\{\dot{A}\} \tag{4.40}$$

and

$$\dot{E}_C = -j\frac{\omega N_1 l_{ef} 2P}{3s_c a_1}\{D\}_C^t\{\dot{A}\} \tag{4.41}$$

respectively.

Using *motor* conventions, the relationship between the terminal voltage and induced voltage will be

$$\sqrt{2}\dot{V}_i = -\dot{E}_i + \dot{I}_i Z \qquad (i = A, B, C) \tag{4.42}$$

where Z is the total phase impedance including external impedance except the slot leakage reactance, tooth top leakage reactance and harmonic leakage reactance. The induced voltage $\dot{E}_i$ from field analysis enables the presence of the slot and tooth top leakage flux and harmonic fluxes to be included implicitly. The current and current density flowing in phase-windings are given, respectively, by

$$\dot{I}_i = \frac{\sqrt{2}\dot{V}_i + \dot{E}_i}{Z} \qquad (i = A, B, C) \tag{4.43}$$

and

$$\begin{aligned} \dot{J}_i &= \frac{\dot{I}_i N_1}{s_c a_1} \\ &= \frac{\sqrt{2} N_1 \dot{V}_i}{s_c a_1 Z} - j\omega \frac{2PN_1^2 l_{ef}}{3 s_c^2 a_1^2 Z} \{D\}_i^t \{\dot{A}\} \qquad (i = A, B, C) \end{aligned} \tag{4.44}$$

Eqn. (4.44) is the expression of equivalent current source for voltage source supply. It is clear that the value of calculated current density expressed by Eqn. (4.44) is not only the function of the impressed voltage source, but also related to vector potentials to be solved.

It is to be noted that the corresponding equivalent variational problem for the voltage source is formally identical to Eqn. (4.22) for the current source case. It can be expected that the difference of discretization results between each other lies only in one term related to field source, identified as

$$\begin{aligned} W_j(\dot{A}) &= -\iint_\Omega \dot{J}\dot{A}\, dx\, dy \\ &= -\iint_{\Omega_A} \dot{J}_A \dot{A}\, dx\, dy - \iint_{\Omega_B} \dot{J}_B \dot{A}\, dx\, dy - \iint_{\Omega_C} \dot{J}_C \dot{A}\, dx\, dy \end{aligned} \tag{4.45}$$

where subscripts A, B, C of Ω denote the subregion of phase A winding, phase B winding and phase C winding respectively. Examining phase A winding contribu-

tion to the energy functional, one obtains

$$W_A(\dot{A}) = -\iint_{\Omega_A} \dot{J}_A \dot{A}\, dx\, dy = -\sum_{e=1}^{e_A} \iint_{\Omega_e} \dot{J}_A \dot{A}\, dx\, dy$$
$$= -\sum_{e=1}^{e_A} \Delta_e \left(\frac{\sqrt{2}N_1 \dot{V}_A}{s_c a_1 Z} - j\omega \frac{2PN_1^2 l_{ef}}{3s_c^2 a_1^2 Z} \{D\}_A^t \{\dot{A}\}\right) \frac{(\dot{A}_{ei} + \dot{A}_{ej} + \dot{A}_{em})}{3} \quad (4.46)$$

where e_A is the number of all the elements in the sub-region of phase A winding. Differentiating with respect to any one of the nodal potentials $\dot{A}_l$ and noting that the vector potentials $\{\dot{A}\}$ in the bracketed current density factor have to be considered as constant, we have

$$\frac{\partial W_A}{\partial \dot{A}_l} = -\frac{\sqrt{2}N_1 \dot{V}_A}{3s_c a_1 Z} d_{Al} + j\omega \frac{2PN_1^2 l_{ef}}{9s_c^2 a_1^2 Z} \{D\}_A^t \{\dot{A}\} d_{Al} \quad (4.47)$$

where d_{Al} was defined by Eqn. (4.39).

Similarly, the contributions of phase B winding and phase C winding are given, respectively as:

$$\frac{\partial W_B}{\partial \dot{A}_l} = -\frac{\sqrt{2}N_1 \dot{V}_B}{3s_c a_1 Z} d_{Bl} + j\omega \frac{2PN_1^2 l_{ef}}{9s_c^2 a_1^2 Z} \{D\}_B^t \{\dot{A}\} d_{Bl} \quad (4.48)$$

and

$$\frac{\partial W_C}{\partial \dot{A}_l} = -\frac{\sqrt{2}N_1 \dot{V}_C}{3s_c a_1 Z} d_{Cl} + j\omega \frac{2PN_1^2 l_{ef}}{9s_c^2 a_1^2 Z} \{D\}_C^t \{\dot{A}\} d_{Cl} \quad (4.49)$$

Therefore, the resulting system of complex simultaneous equations corresponding to the finite element model with the voltage source can be expressed in matrix form as

$$([K] + j\omega_r[H] + j\omega[T])\{\dot{A}\} = \{\dot{P}_v\} + \{\dot{P}\} \quad (4.50)$$

where matrix $[K]$, matrix $[H]$ and vector $\{\dot{P}\}$ have been previously defined for current source case by Eqns. (4.29), (4.30), (4.31) respectively. Matrix $[T]$ and

vector $\{\dot{P}_v\}$ corresponding to the voltage source supply are defined in terms of Eqn. (4.47) to (4.49) by

$$[T] = \frac{2PN_1^2 l_{ef}}{9s_c^2 a_1^2 Z}(\{D\}_A\{D\}_A^t + \{D\}_B\{D\}_B^t + \{D\}_C\{D\}_C^t) \tag{4.51}$$

$$\{\dot{P}_v\} = \frac{\sqrt{2}}{3}\frac{N_1}{s_c a_1 Z}(\dot{V}_A\{D\}_A + \dot{V}_B\{D\}_B + \dot{V}_C\{D\}_C) \tag{4.52}$$

The solutions to the nonlinear equation (4.50) can be obtained by means of the same procedure as in the case for current source supply.

4.3 Determination of Starting Parameters

It is understandable that the proper consideration of skin effect is critical to the accurate evaluation of starting parameters in the impedance matrix $[Z]$ defined by Eqns. (2.12) to (2.15). To this end, the speed response of starting parameters is expected to be obtained to account for the skin effect. The following procedure is employed to extract a set of parameters as a function of slip s from the nonlinear eddy-current field solutions.

4.3.1 Preliminary Consideration

d-axis and q-axis Starting Equivalent Circuits

The d-axis and q-axis starting equivalent circuits as shown in Fig. 4.1 can assist one to obtain the starting parameters based on field solutions. The d-q axis rotor resistances and leakage reactances r'_{2d}, r'_{2q}, x'_{2d}, x'_{2q} are not constant and may change notably with the rotor speed due to skin effect and nonlinearity. x_{1e} denotes stator end winding leakage reactance and x_{1s} denotes the summation of stator slot leakage reactance, tooth top leakage reactance and harmonic leakage reactance. It is to be

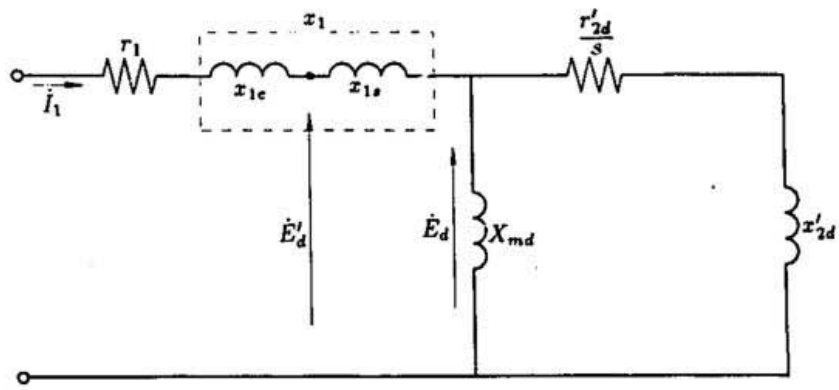

(a) d-axis

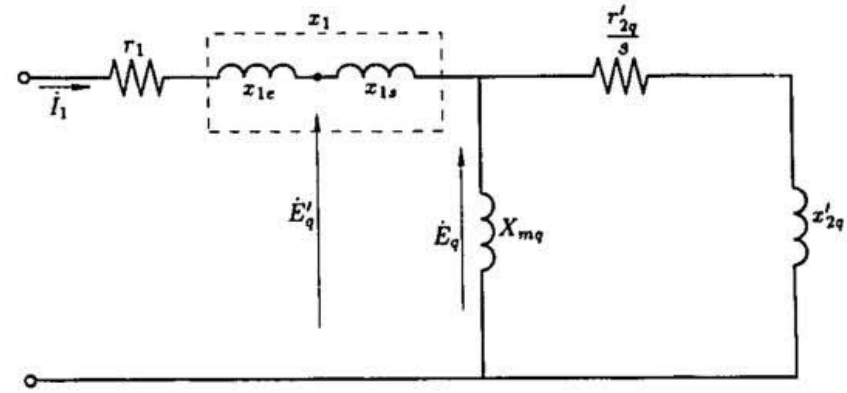

(b) q-axis

Figure 4.1: d-q axis starting equivalent circuits

noted that x_{1_s} comes from the conventional analytical formula; while the x_{1_s} may be determined directly from the field solutions.

First, voltage-source finite element model is applied to get the starting current corresponding to motor operation mode and the stator leakage reactance x_{1_s}. Then, with the just obtained starting current, the finite element model for current source supply is applied to calculate the d-axis field and q-axis field, respectively, so as to determine the speed response of each parameter.

Saturation Effect

Since in the starting process, the magnets will not induce any eddy-current in the rotor part, these starting parameters can be determined based only on induction motor operation mode, that is, no need to consider the excitation of magnets. However, the effects of magnets on magnetic saturation level have to be taken into account. Moreover, this kind of consideration is subjected to what will be expected from the related field solutions.

Under the first case for determining starting current, an auxiliary complex vector potential $\dot{A}'^{(k)}$ corresponding to the kth iteration is introduced and defined by

$$\dot{A}'^{(k)} = \frac{|\dot{A}^{(k)}| + |A_m|}{|\dot{A}^{(k)}|}\dot{A}^{(k)} \tag{4.53}$$

where $\dot{A}^{(k)}$ is the complex vector potential solution of the nonlinear equation (4.50) from the kth iteration; A_m is the real vector potential solution due to permanent magnet excitation alone, which was previously stored in computer memory as input data. In terms of the auxiliary complex vector potential $\dot{A}'^{(k)}$, one can obtain the corresponding flux density by

$$\bar{\dot{B}}'^{(k)} = \dot{B}_x'^{(k)}\bar{i} + \dot{B}_y'^{(k)}\bar{j}$$

$$= \frac{\partial \dot{A}'^{(k)}}{\partial y}\bar{i} - \frac{\partial \dot{A}'^{(k)}}{\partial x}\bar{j} \tag{4.54}$$

After further getting the amplitude $B_m'^{(k)}$ with the help of Eqn. (4.13), the required equivalent reluctivity $\nu_e^{(k+1)}$ for the next iterative solution can be determined from the equivalent magnetization curves by parabolic interpolation.

For the second case with the aim to determine the d-axis and q-axis parameters from corresponding d-axis or q-axis field analysis, as only a particular space position of stator MMF is involved, an auxiliary real vector potential $A'^{(k)}$ is introduced to consider the effect of magnets on the magnetic saturation of the material and is defined by

$$A'^{(k)} = Re(\dot{A}^{(k)}) + A_m \tag{4.55}$$

The corresponding flux density is obtained by

$$\begin{aligned} \bar{B}'^{(k)} &= B_x'^{(k)}\bar{i} + B_y'^{(k)}\bar{j} \\ &= \frac{\partial A'^{(k)}}{\partial y}\bar{i} - \frac{\partial A'^{(k)}}{\partial x}\bar{j} \end{aligned} \tag{4.56}$$

and

$$B_m'^{(k)} = [(\frac{\partial A'^{(k)}}{\partial y})^2 + (\frac{\partial A'^{(k)}}{\partial x})^2]^{\frac{1}{2}} \tag{4.57}$$

The required reluctivity $\nu^{(k+1)}$ for the next iterative solution can be evaluated from the fundamental magnetization curve.

End Effects

Since the finite element analysis is limited to 2D, end effects due to the rotor end-ring resistance are treated by a modification of the rotor bar conductivity. The

equivalent conductivity of the bar is given by

$$\sigma_e = \frac{r_b}{r_b + 2r_r}\sigma \tag{4.58}$$

where σ is the original conductivity of the bar, the subscripts b and r stand for bar and rings, respectively. The term r_b is the resistance of one bar given by

$$r_b = \frac{l_b}{\sigma_b S_b} \tag{4.59}$$

and r_r is the resistance of adjacent ring segment referred to the bar.

$$r_r = \frac{Z_2 D_r}{\sigma_r 4\pi P^2 S_r} \tag{4.60}$$

where l_b is the length of bar; Z_2 is the number of bars on the rotor; and D_r is the average diameter of end rings.

The end ring leakage inductance can be accounted by[42]

$$L_e = \frac{\mu_0 Z_2}{3m_1 P^2}(l_b - l_{ef} + 0.18\frac{\pi D_r}{2P}) \tag{4.61}$$

where l_{ef} the effective bore length. The stator end leakage inductance can be accounted for by the conventional method which is usually used for standard induction motor and wire-wound synchronous motor.

4.3.2 Parameter Determination

As mentioned above, three field computations are involved to extract the starting parameters at a specific slip s. One is the integral eddy-current field analysis under voltage source supply for obtaining starting current and stator leakage reactance x_{1s}. The other two are d-axis and q-axis eddy-current field analyses under current source supply to extract rotor d-axis and q-axis parameters, respectively.

Integral Eddy-current Magnetic Field

Nonlinear finite element model with prescribed voltage source is employed. Assuming starting current and stator leakage reactance x_{1s} are both independent of a particular space position of stator magnetomotive force (MMF), the auxiliary complex vector potential $\dot{A}'$ defined by Eqn. (4.53) and the equivalent reluctivity ν_e are applied to take into account the influence of magnetic non-linearity. The rotor is considered to be excited by induced eddy-current at a certain slip s. The eddy-current is assumed to flow in the rotor bar with a modified conductivity σ_e due to the effect of end-ring resistance. The effect of both stator end-winding leakage flux and rotor end-ring leakage flux is taken into account by x_{1e} and x_{2e}, respectively.

The real part of the complex vector potentials can be used to obtain flux plots for any instant time. Fig. 4.2 shows the flux distribution at $s = 1$ condition. The induced voltage per phase is given by

$$\dot{E}_i = -j\frac{\omega N_1 l_{ef} 2P}{3 s_c a_1}\{D\}_i^t\{\dot{A}\} \quad (i = A, B, C) \tag{4.62}$$

It can be expected that the computed values of three induced phase voltages using equation (4.62) are unbalanced due to the unsymmetrical rotor structure and their particular location of individual stator phase windings with respect to a fixed rotor layout. Balanced value of the three induced phase voltages can be restored by transposing the position of individual windings at 120° intervals. Therefore, the adjusted induced voltage, taking phase A for example, will be

$$\dot{E}'_A = \frac{1}{3}(\dot{E}_A + \alpha\dot{E}_B + \alpha^2\dot{E}_C) \tag{4.63}$$

where the operator α is defined by

$$\alpha = e^{j120°} \tag{4.64}$$

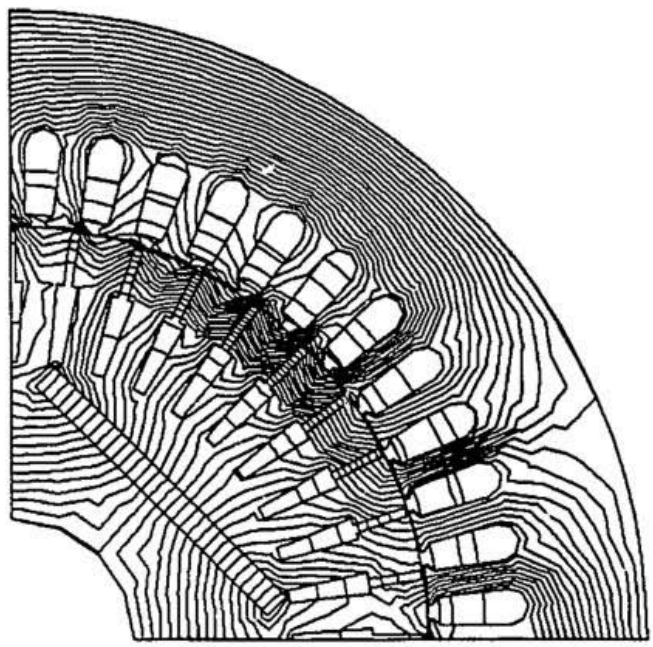

Figure 4.2: Flux distribution at $slip = 1$ instant

The corresponding phase B and phase C induced voltages are

$$\dot{E}'_B = \alpha^2 \dot{E}'_A \tag{4.65}$$

and

$$\dot{E}'_C = \alpha \dot{E}'_A \tag{4.66}$$

It is noted that the induced voltage $\dot{E}'_i$ $(i = A, B, C)$ has incorporated the contribution of slot leakage flux, tooth top leakage flux, and harmonic flux.

The induced voltage $\dot{E}_1$ associated with the fundamental flux is also accessible by performing a Fourier analysis on the real part of complex vector potentials $\dot{A}$ around the outer surface of the the rotor. The flux per pole, which can be regarded as constant with time, is given by

$$\phi_m = \sqrt{\phi_d^2 + \phi_q^2} \tag{4.67}$$

where ϕ_d and ϕ_q are the d-axis and q-axis flux components, respectively. Then, the corresponding induced voltage E_1 per phase is

$$E_1 = 4.44 f \phi_m N_s K_w \tag{4.68}$$

and the phase angle θ is defined by

$$\theta = \tan^{-1} \frac{\phi_q}{\phi_d} \tag{4.69}$$

The phase current can also be obtained as

$$\dot{I}_i = (\sqrt{2}\dot{V}_i + \dot{E}'_i)/Z \qquad (i = A, B, C) \tag{4.70}$$

where Z is the total phase impedance including external impedance except x_{1s}. The value of x_{1s} can be determined from above field-based solutions as

$$x_{1s} = \frac{|\dot{E}'_A - \dot{E}_1|}{|\dot{I}_A|} \tag{4.71}$$

D-axis Eddy-current Magnetic Field

Nonlinear finite element model with prescribed current source will be employed. The value of the prescribed current source has become available from the foregoing integral field computation. The three phase current sources are impressed in such a way so that the axis of the stator MMF is aligned with the d-axis at instant t=0. The influence of non-linearity caused by permanent magnets is taken into account by introducing the auxiliary real vector potential A' defined by Eqn. (4.55) and using fundamental magnetization curve since in such case only a particular space position of the stator MMF aligned with d-axis is involved. Using the same manner as explained in the last section, the induced voltage $\dot{E}_d$ in Fig. 4.1(a) associated with the fundamental flux can be evaluated by performing a Fourier analysis on the real part of the complex vector potentials $\dot{A}$ around the outer surface of the rotor. Analysis will start from $slip = 0$ since in such a case the rotor branch circuit in Fig. 4.1(a) can be regarded as open circuit. As a result, after obtaining the induced voltage $\dot{E}_d$, one can conveniently evaluate X_{md}. Consequently, for other cases rather than $slip = 0$, according to Fig. 4.1(a) the parameters r'_{2d} and x'_{2d} can be extracted in terms of obtained $\dot{E}_d(s)$ and x_{md},

$$Z_d(s) = \frac{-\dot{E}_d(s)}{\dot{I}_1} \tag{4.72}$$

$$r'_{2d}(s) = s\, Re(\frac{Z_d \cdot jX_{md}}{jX_{md} - Z_d}) \tag{4.73}$$

and

$$x'_{2d}(s) = Im(\frac{Z_d \cdot jX_{md}}{jX_{md} - Z_d}) \tag{4.74}$$

where Im means "imaginary part of". The variation of r'_{2d} and x'_{2d} with rotor speed for the illustrative working model is shown in Fig. 4.3 by solid lines.

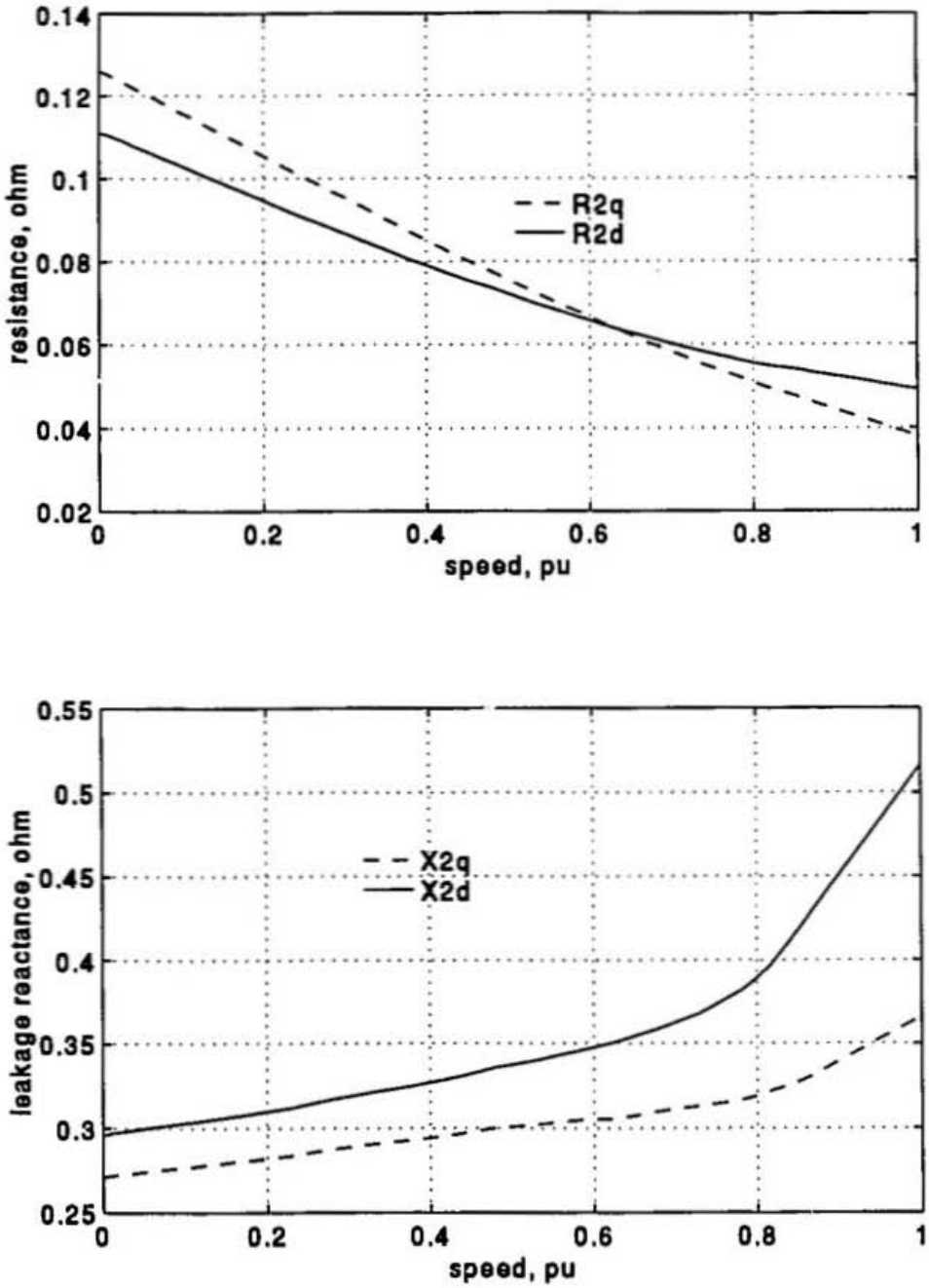

Figure 4.3: Speed response of rotor starting parameters

q-axis Eddy-current Magnetic Field

Nonlinear finite element model with current source supply and q-axis starting equivalent circuit in Fig. 4.1(b) are employed to obtain q-axis starting parameters. The finite element model is identical to the one just discussed for d-axis eddy-current magnetic field analysis except that the three phase current sources are impressed in such a way so that the axis of the stator MMF is in quadrature with the d-axis at instant $t = 0$. The introduction of the auxiliary real vector potential A' defined by Eqn. (4.55) allows us to consider the impact of non-linearity caused by the magnets based on fundamental magnetization curve. For the same reason, the field investigation proceeds from $slip = 0$ so that X_{mq} can first be ascertained. After the determination of $\dot{E}_q(s)$, the parameters r'_{2q} and x'_{2q} can be evaluated for other slips by

$$Z_q(s) = \frac{-\dot{E}_q(s)}{\dot{I}_1} \tag{4.75}$$

$$r'_{2q}(s) = s\, Re(\frac{Z_q . jX_{mq}}{jX_{mq} - Z_q}) \tag{4.76}$$

and

$$x'_{2q}(s) = Im(\frac{Z_q . jX_{mq}}{jX_{mq} - Z_q}) \tag{4.77}$$

The obtained results of r'_{2q} and x'_{2q} at different rotor speed are displayed in Fig. 4.3 by dashed line. It is obvious from Fig 4.3 that the skin effect has considerable impacts on rotor starting parameters. No doubt, using constant parameter values for predicting starting performance would lead to considerable errors.

Finally, the required parameters $X'_D(s)$ and $X'_Q(s)$ referred to stator side can be found as

$$X'_D(s) = X_{md} + x'_{2d}(s) + x'_{2c}(s) \tag{4.78}$$

and

$$X'_Q(s) = X_{mq} + x'_{2q}(s) + x'_{2e}(s) \tag{4.79}$$

where $x'_{2e}(s)$ is the end-ring leakage reactance calculated in terms of Eqn. (4.61).

4.4 Starting Performance Prediction

Availability of accurate field-based starting parameters from the above discussion has provided groundwork for simulating the starting performance by just using lumped parameter model[44]. In order to achieve an identification of different current and torque components in macroscopic sense and present a clear physical understanding of each component, and allow convenient parameter sensitivity analysis, the quasi-dynamic analysis approach will first be discussed. Then, we proceed to the actual transient analysis so as to acquire more detailed information such as maximum current requirement for converter, possible demagnetizing effect on magnets and the time of run up to stable synchronization, as well as synchronization process.

4.4.1 Quasi-dynamic Analysis

As explained in chapter 2, for quasi-dynamic analysis the starting process can be fairly treated as the superposition of two operation modes. One mode is the induction motor with applied voltage source. The other mode is ac PM generator operation with permanent magnet excitation. The saturation effects between these two modes have been properly considered in the above discussed section for determining the starting parameters by introducing the auxiliary complex vector potential $\dot{A}'$ or the auxiliary real vector potential A'. After superposing the results

of these two operating modes, one can get d-q axis instantaneous current components of each winding as expressed by Eqns. (2.25), (2.27) and (2.28). Using Eqn. (2.29), the results can be transformed back to *abc* system to get the instantaneous value of each phase-current. A PM motor under asynchronous mode has three stator current components with different frequency: line frequency f and $(1-s)f$ induced by rotating magnets as well as $(1-2s)f$ caused by unsymmetrical rotor construction. The frequency of the current in cage winding is sf induced by stator rotating field.

The total instantaneous torque including both average and pulsating components can be expressed by substituting Eqn. (2.28) into the torque expression Eqn. (2.19) as

$$\begin{aligned} T &= P[(L_q - L_d)i_d^m i_q^m + L_{mq} i_d^m i_Q^m - L_{md} i_q^m i_D^m] + P[(L_q - L_d) i_d^g i_q^g - L_{md} i_q^g i_f] \\ &\quad + P[(L_q - L_d)(i_q^m i_d^g + i_d^m i_q^g) + L_{mq} i_Q^m i_d^g - L_{md} i_D^m i_q^g - L_{md} i_q^m i_f] \\ &= T^m + T^g + T^{mg} \end{aligned} \tag{4.80}$$

where T^m, T^g and T^{mg} are the torque components corresponding to the motoring mode, generating mode and the interaction between these two modes, respectively.

Substituting Eqn. (2.25) corresponding to the motor operation mode into the first term of Eqn. (4.80), one obtains

$$\begin{aligned} T^m &= P[(L_q - L_d)(AC + BD) + L_{mq}(AG + BH) - L_{md}(EC + FD)] \\ &\quad P[(L_q - L_d)(AC - BD) + L_{mq}(AG - BH) - L_{md}(EC - FD)] \cos 2s\omega t \\ &\quad P[(L_q - L_d)(AD + CB) + L_{mq}(AH + GB) - L_{md}(ED + CF)] \sin 2s\omega t \\ &= T_{av}^m + T_{2s}^m \end{aligned} \tag{4.81}$$

It is shown that T^m is comprised of average cage torque component T^m_{av} and pulsating torque component T^m_{2s} with angular frequency $2s\omega$ owing to the unsymmetry between the rotor d-axis and q-axis. The pulsating torque T^m_{2s} arises from the interaction between the backward rotating component, with angular frequency $(1-2s)\omega$ resolved from the rotor elliptic MMF, and the stator MMF rotating at the angular frequency of supply and from saliency reluctance effects.

When the current components from Eqn. (2.27) subjected to the generator mode are substituted in the second term of Eqn. (4.80), one easily obtain

$$T^g_{(av)} = -\frac{P}{(1-s)\omega}\left[\frac{r_1^2+(1-s)^2X_q^2}{r_1^2+(1-s)^2X_dX_q}\right]\left[\frac{3(1-s)^2E_0^2r_1}{r_1^2+(1-s)^2X_dX_q}\right] \tag{4.82}$$

where negative sign indicates the average torque is of braking type. The second bracketed term represents the torque due to permanent magnets and the first bracketed modified term is used to account for the rotor saliency effect.

Substituting each current component from Eqns. (2.25) and (2.27) into the third term of Eqn. (4.80) will yield

$$\begin{aligned} T^{mg}_{(s)} &= \sqrt{2}P[(L_{mq}Gi^g_d - L_{md}Ei^g_q)\cos s\omega t + (L_{md}Fi^g_q - L_{mq}Hi^g_d)\sin s\omega t] \\ &\quad +\sqrt{2}P(L_q - L_d)[(Ai^g_q + Ci^G_d)\cos s\omega t - (Bi^g_q + Di^g_d)\sin s\omega t] \\ &\quad -\sqrt{2}P[C\cos s\omega t - D\sin s\omega t]L_{md}i_f \end{aligned} \tag{4.83}$$

It can be seen from Eqn. (4.83) that the interaction between the two operating modes will not develop average torque but only the pulsating torque with angular frequency $s\omega$. The first and second terms of the pulsating torque components in Eqn. (4.83) are attributed to the MMF interaction of the stator generating mode component with the rotor forward component and the backward component,

respectively, resolved from elliptic rotor MMF owing to the unsymmetric rotor structure. If $L_d = L_q$, the second term of the pulsating torque would vanish since the rotor backward rotating MMF would disappear. The third term of the pulsating torque in Eqn. (4.83) arises from the MMF interaction between the stator motoring mode component and permanent magnet.

Therefore, total torque can be expressed as

$$T_e = T_{av}^m + T_{av}^g + T_{2s}^m + T_s^{mg} = T_{av} + T_p \tag{4.84}$$

Fig. 4.4(a) shows the resulting average torque T_{av} as well as its individual components: cage torque component T_{av}^m and magnet torque component T_{av}^g for the illustrative model. In this case, all parameters are chosen as constant values at $slip = 0$. It can be seen that the curve of T_{av}^m is similar to the typical characteristics of induction motor except with a dip at slip slightly less than 0.5. This dip is caused by the electrical and magnetic unsymmetry between the d-axis and q-axis. The rotor backward rotating magnetic field resolved from the elliptic MMF will induce current in stator winding with angular frequency $(1-2s)\omega$ and then the current will produce another rotating magnetic field. These two rotating magnetic fields both at angular velocity $(1-2s)\omega$ will develop another pair of asynchronous torque. However, in such a case the rotor should be viewed as the primary and stator as the secondary, and moreover, $s = 0.5$ corresponds to their synchronous speed. Because $(1-2s)\omega$ is of positive value over the smaller range than 0.5 slip, the stator viewed as the secondary stands a torque in ω direction, and thus rotor will suffer a braking torque with equal magnitude but opposite direction. This braking torque will reach its maximum value at slip slightly less than 0.5, and leads to a torque dip on the resulting average torque curve at slip slightly less than 0.5.

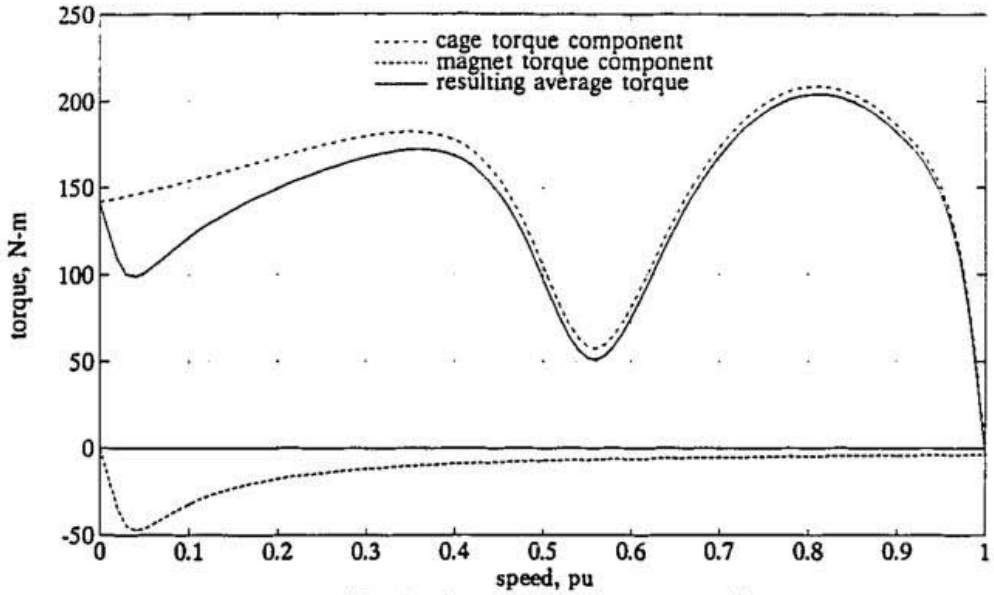

(a) using invariant parameters at $s = 0$

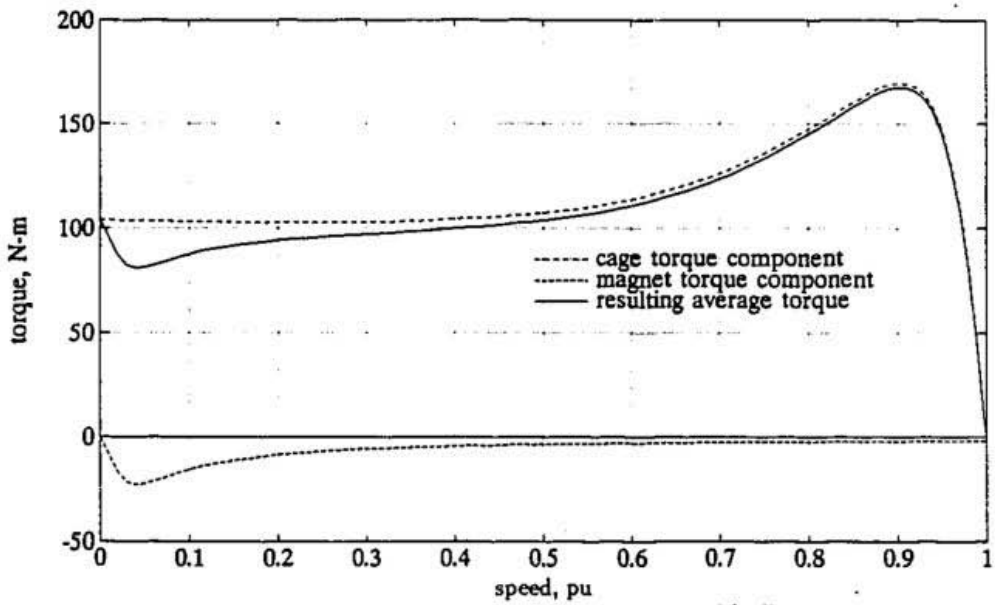

(b) using varying dynamic parameters with slip

Figure 4.4: Average torque as well as its components

The existence of this torque dip has been pointed out in the literatures[9, 11] and is usually considered as one of the main concerns for wide potential applications of PM motors. Fortunately, this concern may turn out to be uncalled-for. This is attributed to the skin effects which may favorably make rotor dynamic parameters much less unsymmetrical. Fig. 4.4(b) shows the simulation results of the average torque characteristics using varying dynamic parameters. The dip in the cage torque component has disappeared.

The magnet torque T^g_{av} at zero speed is zero. The torque after passing through a maximum, usually at a low speed, becomes nearly constant as shown by Fig. 4.4(b). When the magnet torque T^g_{av} is combined with cage torque T^m_{av}, a dip is produced in the resulting average torque T_{av}. This dip may be the main concern for the successful starting, but not the previous understanding that there exist two dips.

The pulsating torque T_p is comprised of double-slip-frequency component $T^m_{(2s)}$ and single-slip-frequency component $T^{mg}_{(s)}$. Of the two pulsating components, the single-slip-frequency component is much larger than the double-slip frequency component. Fig. 4.5 shows the magnitude envelopes of these two components for the illustrative model. The average torque is responsible for propelling the rotor forward while the pulsating torque only produces noise and vibration during starting.

4.4.2 Transient Analysis

The analysis consists of both mechanical and electromagnetic transients. It is well described by state-variable equation (2.32). The transient performances are computed by solving the state-variable equation numerically. It is expected that accurate results can be obtained when using those properly identified starting pa-

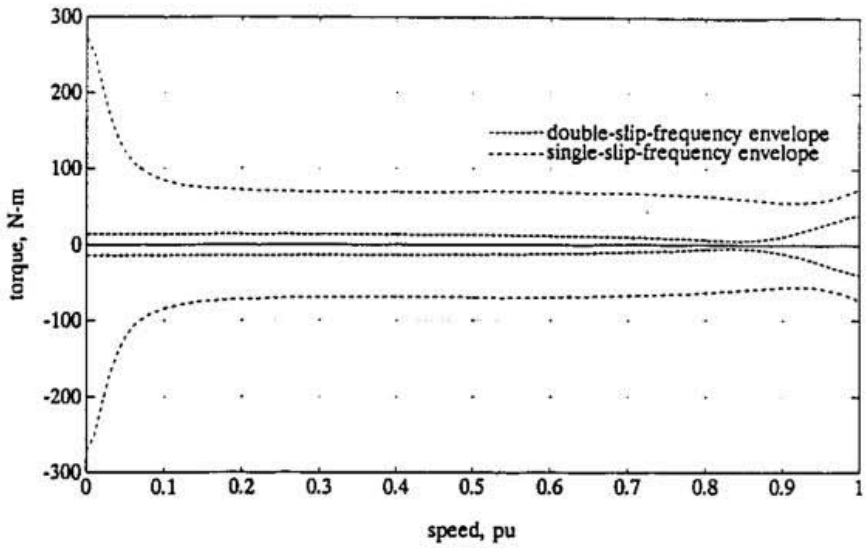

Figure 4.5: Envelopes of pulsating torque components

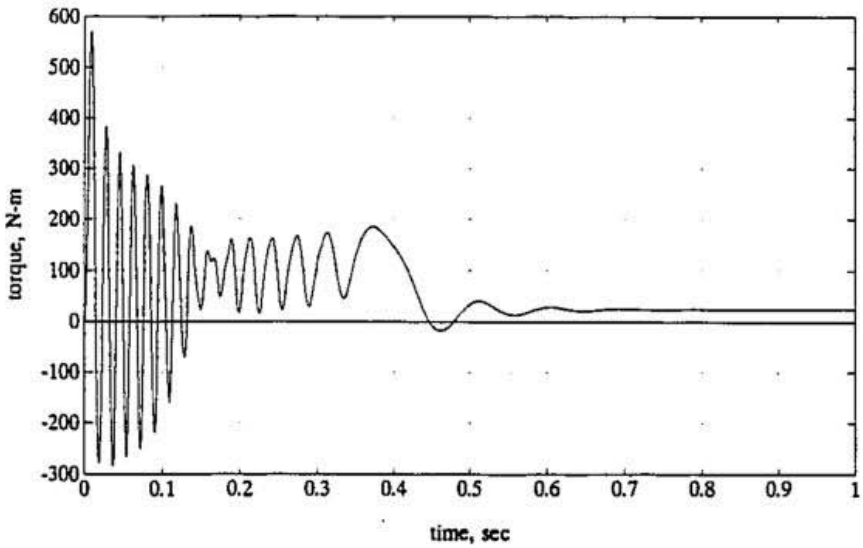

Figure 4.6: Torque-time curve during run-up

rameters. Fig. 4.6 and Fig. 4.7 show the torque versus time and speed, respectively, with the load torque chosen at 25 N-m for a coupled inertia of three times the rotor inertia. Fig. 4.8 shows the speed versus time curve and Fig. 4.9 gives the details of the starting phase current. These computed results are useful in order to ensure that a PM motor is well designed to start and synchronize properly. A general procedure for stating performance analysis based on finite element method is indicated by the flow chart as shown in Fig. 4.10.

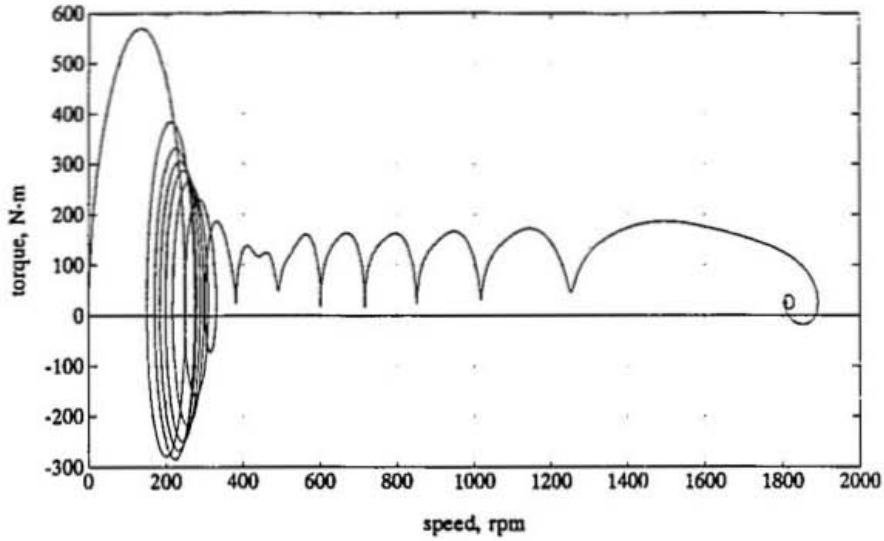

Figure 4.7: Torque-speed curve during run-up

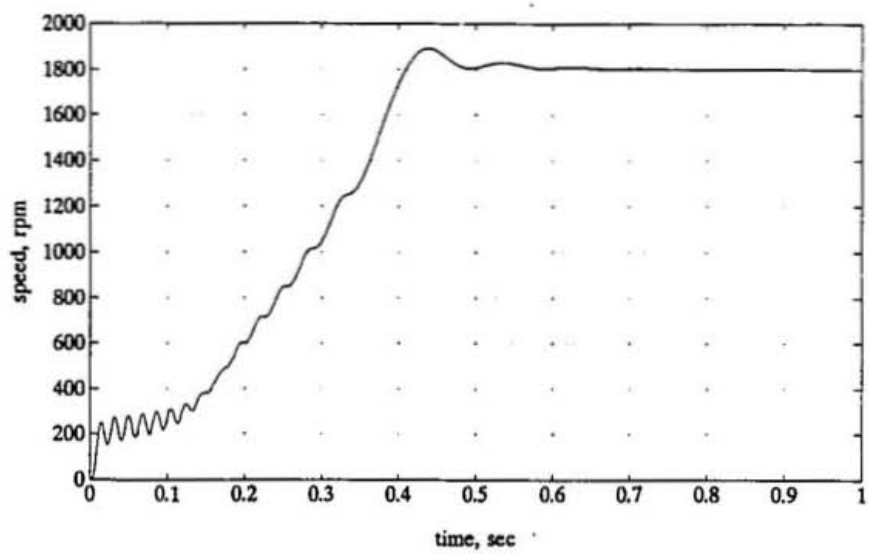

Figure 4.8: Speed-time curve during run-up

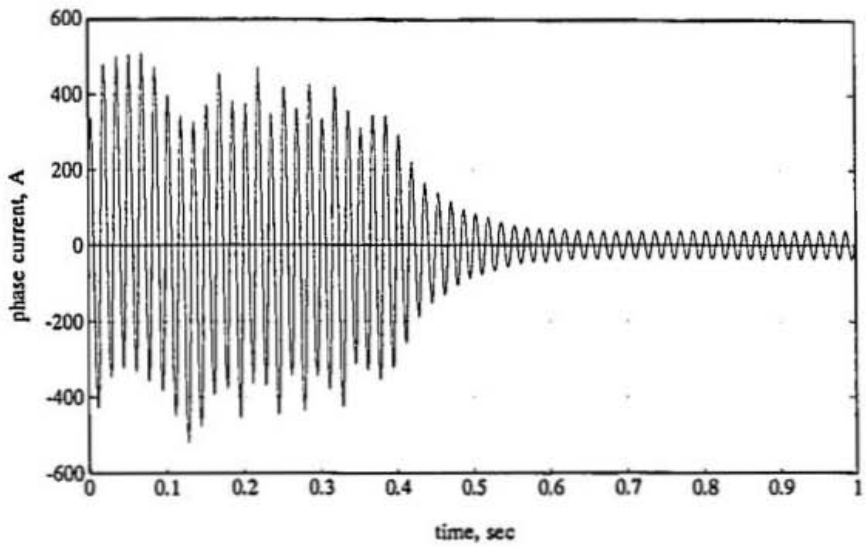

Figure 4.9: Variation in phase-current during run-up

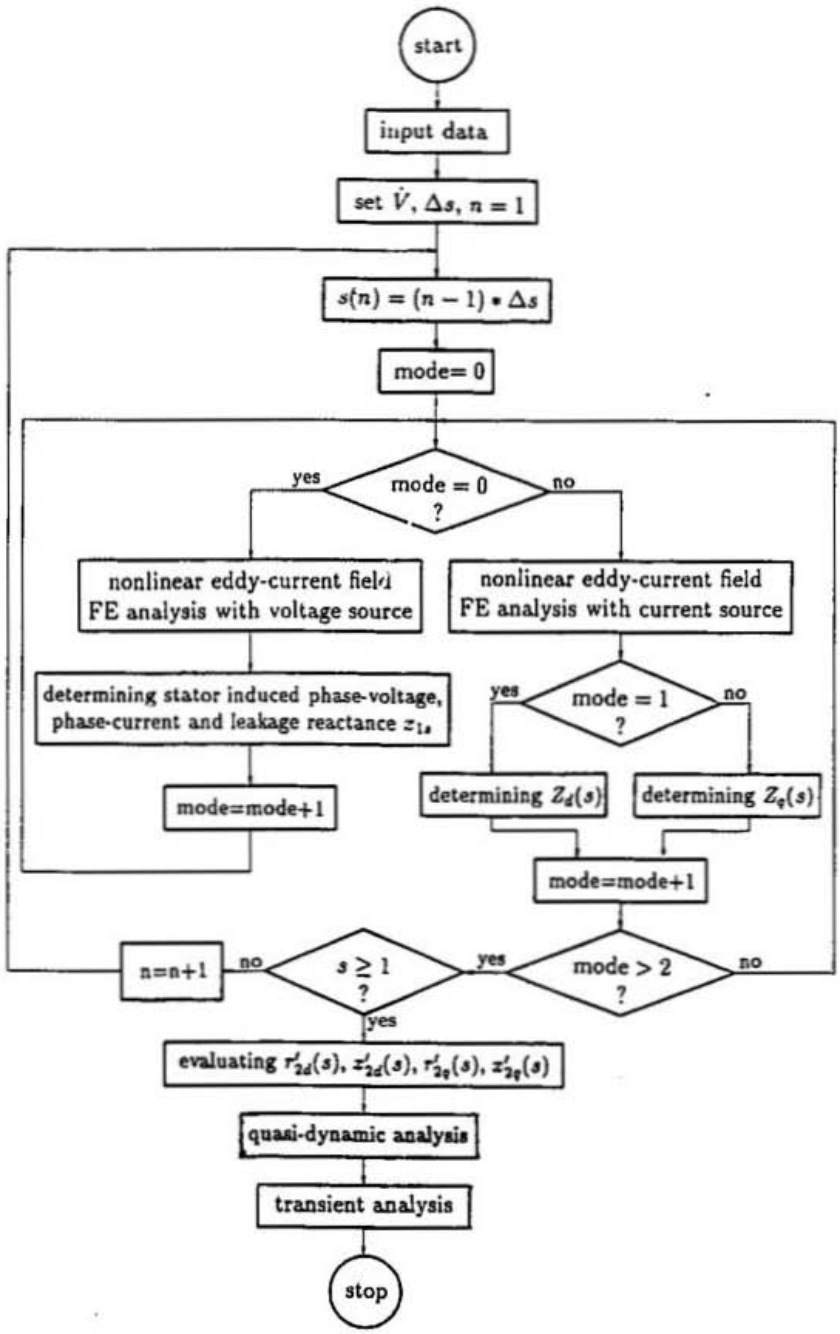

Figure 4.10: Flow chart for starting performance analysis

Chapter 5

Experimental Study

As an integral part of this study, an attempt is made to deal with some testing problems. In this chapter, the experimental setup is first outlined. A discussion on how to determine the load-dependent reactance parameters X_d, X_q and magnet-excited voltage E_0 is presented. A microprocessor-based digital torque angle measurement sub-system is described in detail. Finally, a scheme for accurately locating the position of zero torque angle is presented[45].

5.1 Experimental Setup

The experimental setup for the test investigation is shown in Fig. 5.1. The left side is the PM motor under investigation. In order to cover the full range of load angles, the test PM motor is coupled to the wire-wound synchronous machine as shown on the right side of Fig. 5.1. The synchronous machine is operated in generating mode to provide a required load torque. The stator current of the loading synchronous machine is dissipated in a large 3-phase power resistance bank.

A torque transducer is connected between the PM motor and the generator. The transducer is capable of accurately measuring cyclic torque variation and torque

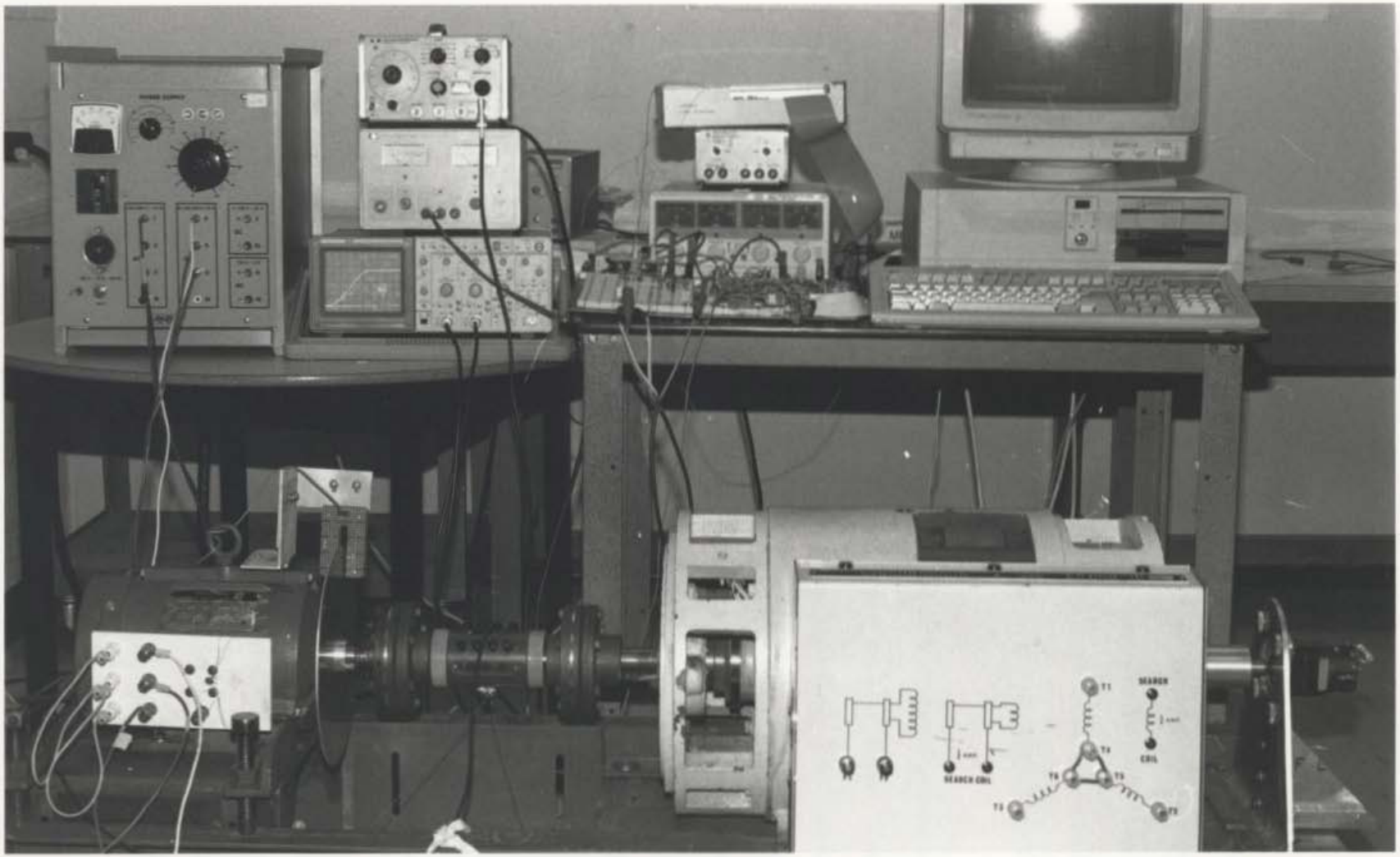

Figure 5.1: Experimental setup

transient. The torque signal is amplified by a low pass filter with a gain of 20dB and recorded by a multiple-channel storage oscilloscope. Torque angle measurement is achieved by using a digital torque angle measurement subsystem (described in section 5.3), which includes a magnet-excitation voltage transducer consisting of a rotor shaft-mounted disc and a stator frame-fixed photo-coupler as shown in Fig. 5.1.

The speed response of the PM motor is detected by a tacho-generator which is mounted on the far left end of the synchronous generator shaft. The output signal is directly fed into a storage oscilloscope for recording. The transient current is monitored through isolation-type current transducers having a good linear response over wide range. The input power is measured by the two-wattmeter method. A Lab-master board with built-in A/D and D/A converters is used for data acquisition and interface with the microcomputer. Various waveforms stored on the oscilloscope are printed out by a plotter connected to the parallel printer interface of the oscilloscope.

It is assumed that the armature resistance at ambient temperature is obtained in the usual manner from its dc value corrected by an appropriate factor to allow for skin and proximity effects.

In practice, owing to the existence of various noise disturbance in the measuremental environment, random inaccuracies in the measured data may occur. For some measured quantities, it may be advisable first to smooth the measured data by digital low pass filter in order to avoid the propagation of errors originating from this source.

5.2 Modified Load Test Method

In the measurement of machine parameters from test, it is not possible to isolate the stator leakage reactance from the total direct and quadrature synchronous reactances. It is common practice to lump the leakage into the synchronous reactances, which leads to the simplified phasor diagram as shown in Fig. 5.2.

Because the parameters X_d, X_q and E_0 tend to vary widely with loads due to saturation, the values of these parameters must be quoted together with the load and voltage conditions under which these were determined. From the phasor diagram, the following can be obtained as

$$E_i sin\delta_i = I_1 \sin\beta X_q \tag{5.1}$$

$$E_i cos\delta_i = E_0 + I_1 \cos\beta X_d \tag{5.2}$$

It is noted that once the data of applied voltage V, current I_1, input power P_1 and torque angle δ are known from the load test, other quantities in Eqns. (5.1) and (5.2) can be obtained as

$$E_i = \sqrt{(V\sin\delta + I_1 r_1 \cos\beta)^2 + (V\cos\delta - I_1 r_1 \sin\beta)^2}, \tag{5.3}$$

$$\delta_i = \arctan\frac{V\sin\delta + I_1 r_1 \cos\beta}{V\cos\beta - r_1 I_1 \sin\beta} \tag{5.4}$$

where

$$\beta = \frac{\pi}{2} + \delta - \varphi \tag{5.5}$$

and

$$\varphi = \arccos\frac{P_1}{3I_1 V} \tag{5.6}$$

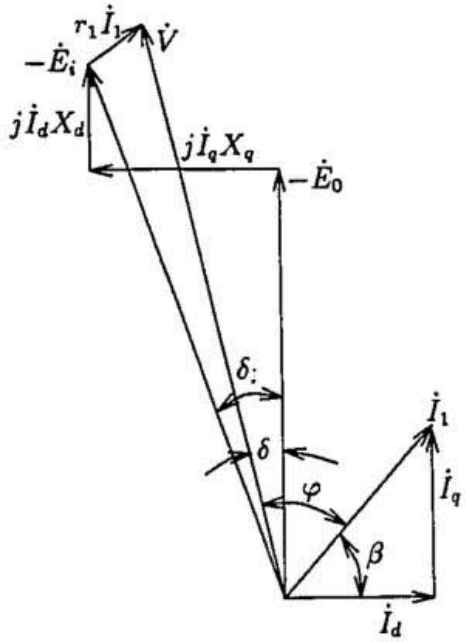

Figure 5.2: PM motor phasor diagram for testing

It is clear that the q-axis reactance X_q can easily be obtained using equation (5.1). However from Eqn. (5.2) itself, it is inadequate to evaluate the two unknown quantities E_0 and X_d. To this end, a small perturbation of the load is exerted to obtain another set of test data, which yields the following equation

$$E_i' cos\delta_i' = E_0 + I_1' \cos\beta' X_d \tag{5.7}$$

As a result, solving the simultaneous algebraic equations (5.2) and (5.7) gives the values of the saturated values E_0 and X_d for any operating point. In practice, the procedure is simply first to produce three curves $E_i(\beta)$, $\delta_i(\beta)$ and $I_1(\beta)$ by curve fitting from recorded data of applied voltage V, current I_1, input power P_1 and torque angle δ, which cover the entire range of different loads. Then, the required information for both equations(5.2) and (5.7) is obtained from reading these curves. Fig. 5.3 shows the values of X_d, X_q and E_0 for a 1 hp 4-pole interior-type PM synchronous motor by using the above proposed modified load test method. The effect of assuming constant E_0, as made in the original load test method[3, 23], on the value of X_d can be clearly seen from the dashed-line curve in Fig. 5.3(a). Over a load range around $\delta = 47°$ where the armature reaction in d-axis is changing from magnetizing to demagnetizing mode, the value of X_d becomes extremely irregular. This phenomenon was also observed in references[3, 23, 32]. This irregularity is due to the assumption of constant E_0 which, in fact is dependent on the saturation level, particularly in the region of ferromagnetic bridges. It is evident from Fig. 5.3(c) that E_0 is load dependent.

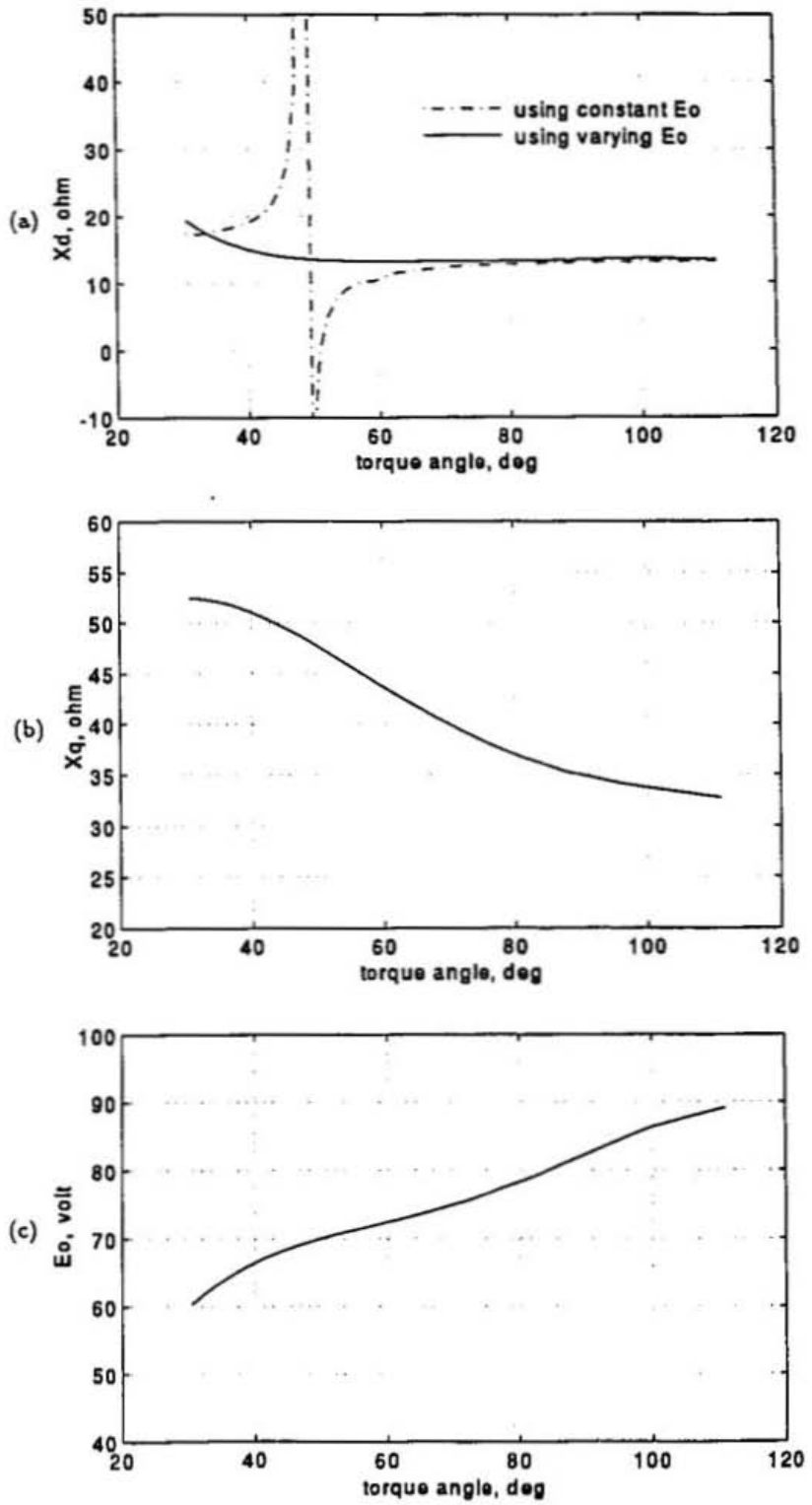

Figure 5.3: Test results of X_d, X_q and E_0 with load angle δ

5.3 Microprocessor-based Load Angle Measurement

The torque angle of a synchronous machine is defined as the angular displacement between the excitation voltage E_0 and the terminal voltage V, as shown in Fig. 5.2. For motoring operation, when the zero crossing of any one of the three phase terminal voltages is used as the reference to initiate a pulse and the zero crossing of the magnet excitation voltage in the same phase winding is used to terminate the pulse, the resulting pulse width represents the instantaneous torque angle. For generating mode, the reverse will happen.

The signal representing the excitation voltage is derived from a transducer consisting of a rotor shaft-mounted disc with an equi-spaced hole drilled on the circumference for each pole pair and a stator frame-fixed photo-coupler as indicated in Fig. 5.1. This photo-coupler can produce a pulse whenever any one of the holes cut across the photo-coupler governed by the rotation of the shaft. This arrangement can always provide one pulse per cycle of the terminal voltage when the shaft rotates at synchronous speed. The produced chain of low voltage pulses are then amplified to TTL level using voltage comparator as shown in the block diagram of Fig. 5.4. The reference voltage of the comparator is set to 0.6V so as to eliminate the noise from the photo-coupler signal.

The reference terminal phase voltage signal is derived through a step-down transformer. Before the reduced sinusoidal voltage is converted into a 5V rectangular pulse by the zero-crossing voltage detector, a phase-lag shifter with a range of 0 to 180° is employed to provide an approximate means for positioning the zero torque angle. It is intended to ensure that the photo-pulse at point a in Fig. 5.4

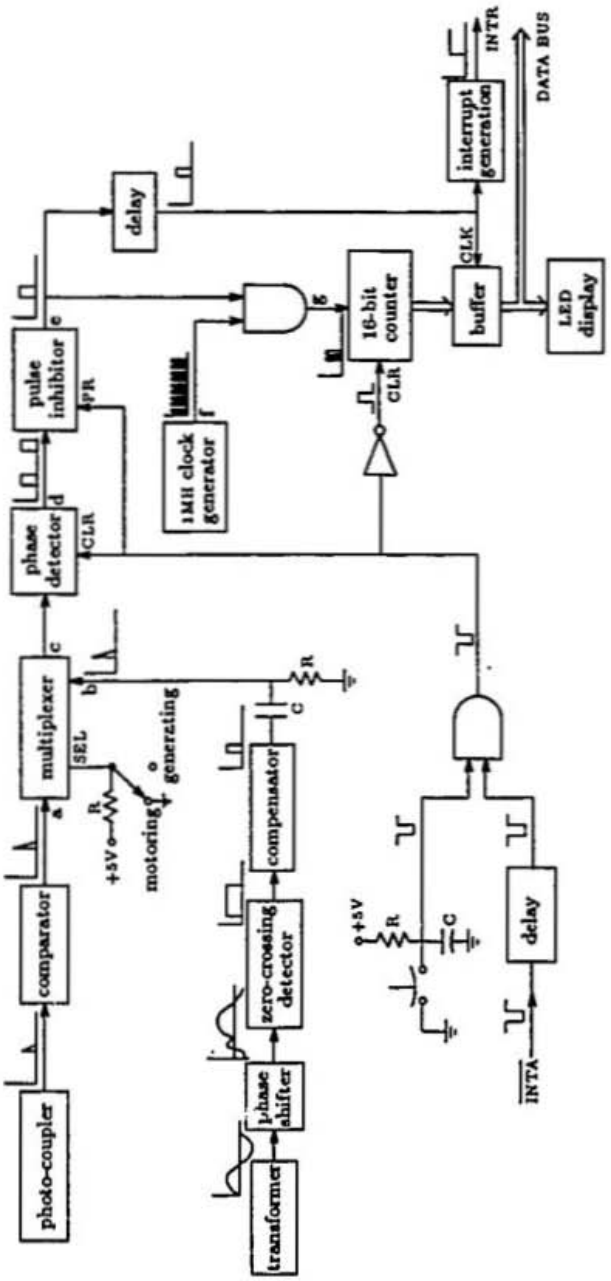

Figure 5.4: Block diagram for torque angle measurement

will align with the terminal voltage pulse at point *b* at no-load operation by adjusting the variable resistor of the phase shifter. Since the whole circuit operates on a single 5V supply for the sake of simplicity, the output of the negative half cycle of the phase shifter has been severely distorted, which makes the zero-crossing from negative to positive of the waveform useless. Therefore, the instant of the zero-crossing from positive to negative is used to signal the terminal voltage (see Appendix E). As a consequence of this 180° phase shift, the net effect of the phase shifter has become a phase-lead network with a range of 0 to 180°. For practical applications, it is desired to make the phase shifter work as both phase-lead and phase-lag circuit. To this end, a compensator is introduced to offset the phase to a certain degree as desired at the output of the compensator by adjusting the RC time constant of the compensator.

It is noted that for the motoring mode, the pulses at point *b* in Fig. 5.4 have to be taken as reference; while for generating mode, the pulses at point *a* have to be taken as reference. Therefore, a multiplexer circuit (see Appendix) is employed to enable this measurement device to be applicable to both the motoring and generating modes.

If the output gate pulse of the phase detector at point *d* of Fig. 5.4 is combined with the 1MHz clock pulses at point *f*, a chain of the clock pulses at point *g* are produced through an AND gate, and the number of these clock pulses is a measure of the torque angle. However, when these clock pulses are used to drive a 16-bit BCD counter, occasionally, false counting may occur. The reason is that in the case of high machine speed and heavy load, the next output gate pulse at point *d* may start before the final settled number of the counting is latched to the buffer and

counter is cleared. To avoid this undesirable operation, a pulse inhibitor is employed to ensure that no further gate pulses would pass to the AND gate until the reset signal is issued, which comes from the reset switch or interrupt acknowledgment signal ($\overline{INTA}$) from the microprocessor as indicated in Fig. 5.4.

Since 1MHz clock frequency is employed, for a 60Hz power supply system, there are 8,333 pulses corresponding to 180° electrical, which is the maximum torque angle to be measured. Thus, a resolution of 0.02 electrical degree per pulse is obtained. To obtain a stable reading, the buffer is enabled after the counting is over and hold the information until the arrival of next count. The output of the buffer is further fed into a microprocessor using 8255 programmable parallel port as the interface. At the same time, the buffered data are also decoded by display driver into 7-segment LED display.

The clock signal for latching the buffer and the interrupt signal can be derived from the output of the pulse inhibitor through a delay element to account for the propagation delay of the 16-bit cascade counter. The interrupt signal is produced using a JK flip-flop whose output goes high once the delay is over.

The above discussed torque angle measurement subsystem was designed, built and tested on the 1 hp, 4-pole PM motor which is coupled to a conventional synchronous generator. The measurement system functioned properly as desired and was also found to be very stable over the entire range of operating conditions.

5.4 Determination of Zero Torque Angle Position

Due to the characteristics of a PM motor, the precision of measured torque angle is highly related to the accuracy of the positioning of zero torque angle. For a PM motor under normal voltage supply, the no-load operation is at $\delta = \delta_0$ as explained in section 2.2, and therefore can not be used to position the zero torque angle. Usually, an approximate method is employed to determine the position of $\delta = 0$. As indicated by equation (2.36), the reluctance torque varies as V^2 while the magnet torque varies as V. As a result, a reduction in the terminal voltage causes a much greater reduction in the reluctance torque than in the magnet torque. This results in a decreased value of δ_0. When V is reduced to a value very close to E_0, the torque angle will fall to a minimum value. The value at this point is usually assumed to be zero torque angle. This angle difference with normal no-load operation at rated voltage is considered to be approximately δ_0. In practice, this approximation is identical to neglecting the windage and friction and iron losses. Even though the approximate method is convenient to employ, it is desirable to find a way which can accurately locate the zero torque position for precision measurement and control purposes.

From the above discussion, it is noted that the signal representing the excitation voltage can be errorless only if the holes on the disc are aligned with d-axis of the rotor and the photo-coupler is positioned at the axis of that particular stator phase winding whose applied voltage has been taken as the reference signal. However, unless special marks were made on the rotor during assembly, there is no obvious reference to determine the position of the d-axis. In order to overcome this difficulty,

a scheme is introduced to find out the positions of d-axis of the rotor and the axis of the referenced stator phase winding with no need for the accessibility to the internal construction of the motor. The procedure is described in the following steps:

1. Mount the disc with an equi-spaced hole for each pole pair on the rotor shaft and fix the photo-coupler to the stator frame, with both at arbitrary position. Then, take any one of three phase voltages as phase A to provide the referenced phase voltage signal for the primary of the step-down transformer.

2. Turn on the three-phase power supply and run the PM motor at no-load. By reversing the leads of the phase A power supply to the primary of the transformer, and/or interchanging the three-phase power supply leads to the three-phase stator windings, find out the connection which would lead to a minimum torque angle reading. Under this connection, the stator winding connected to the phase A power supply is then the phase A stator winding.

3. Run the motor first in one direction and get the torque angle reading, then do the same at the reverse direction by interchanging the phase B and phase C power supply. Assuming that the photo-coupler was just positioned at the axis of phase A winding of the stator, then both the torque angle readings should be the same if the holes on the disc were aligned with the d-axis of the rotor. This suggests that the disc has to be moved towards the rotating direction which has given the larger torque angle reading if both readings are not the same. This adjustment is repeated until the two readings respectively corresponding to forward and backward rotating directions are reasonably close.

4. In step 3, it is assumed that the arbitrary positioning of the photo-coupler was just aligned with the axis of phase A winding. Generally speaking, it is not

true. Hence, an adjustment is needed to relocate the position of the axis of phase A winding. It can be done by applying a low dc voltage to the three-phase stator windings with the connection as shown in Fig. 5.5. What happens is that the disc will rotate in such a way that the holes on the disc, which represents the d-axis of the rotor, should move to the axis of phase A winding. As a result, one can easily relocate the photo-coupler to the position as indicated by one of the holes.

Due to the adjustment of photo-coupler position in step 4, the holes on the disc have to be positioned again by repeating step 3. This iteration process is continued until no further adjustment is made in step 4. Practical application shows that only few iterations are required for both the holes on the disc and the photo-coupler to converge to their correct positions.

By using the proposed scheme, the initial torque angle for the 1 hp laboratory test PM motor is 29.6°; while using the approximate method, the initial torque angle is 22.2°. It can be seen that the error caused by the approximate method is quite significant.

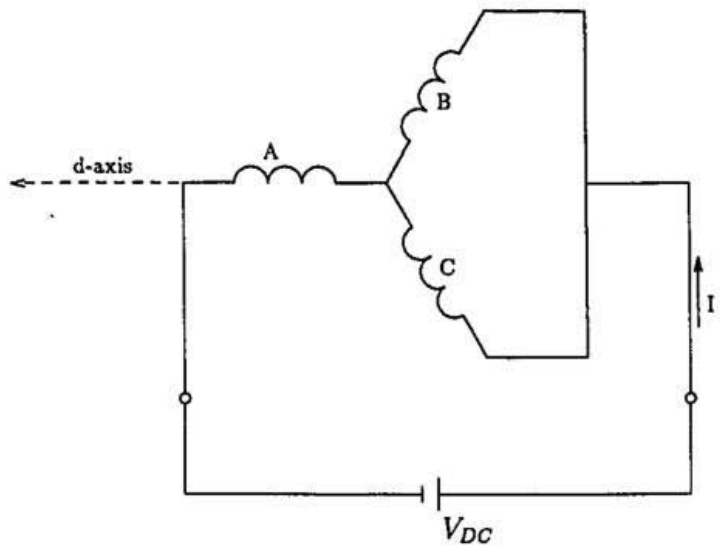

Figure 5.5: Connection of stator windings for locating the axis of phase *A* winding

Chapter 6

Application Example

A complete field-circuit combined procedure for the simulation of both the synchronous performance and starting process, along with the improved test techniques, have been discussed in the previous chapters. In this chapter, an application example is presented to provide a full picture of the usefulness of the proposed analysis and test techniques.

6.1 Working Model

A laboratory interior-magnet type motor with the configuration shown in Fig. 6.1 is employed to serve as the working model. The specifications of pertinent design data of this PM motor is given in Table 6.1. The standard aluminum rotor cage was used to provide the capability for line frequency starting and synchronization. The $SmCo_5$ magnets are used in the rotor. The $SmCo_5$ magnets were modeled in the finite element analysis by a linear demagnetization characteristic, having a residual flux density of 0.78 T and a coercivity of 626 kA/m. The initial finite element discretization of the one pole cross section of the permanent magnet synchronous motor is shown in Fig. 6.2 by using the mesh scheme as explained in

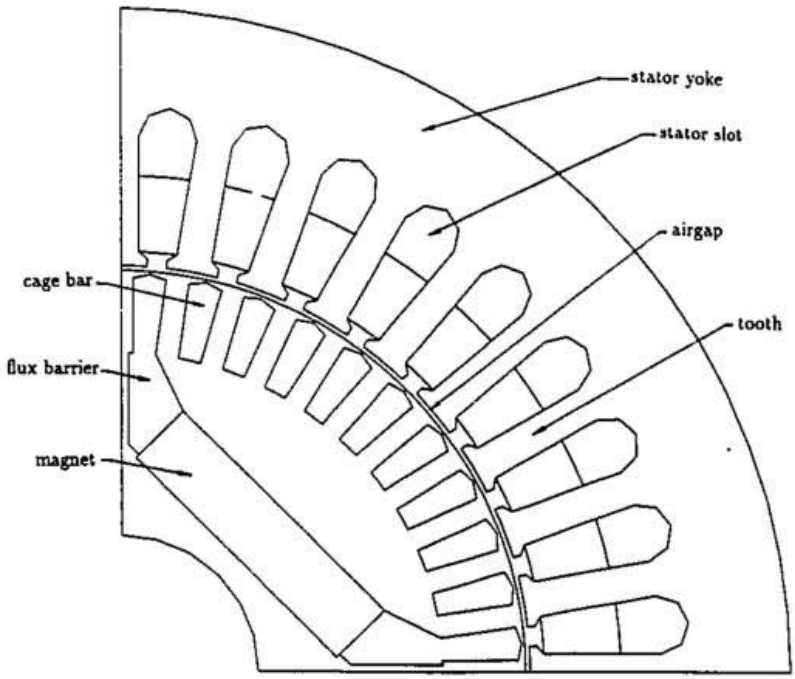

Figure 6.1: Configuration of the worked PM motor

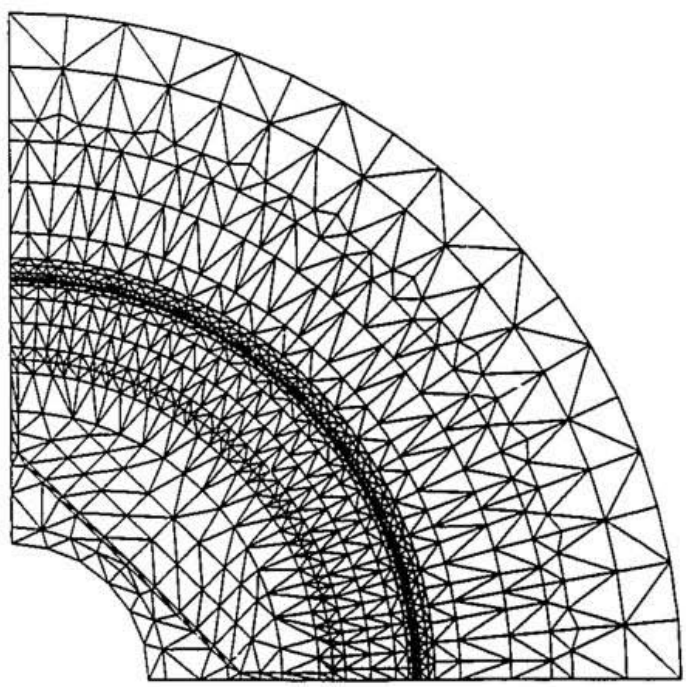

Figure 6.2: Initial finite element discretization of the worked PM motor

Table 6.1: Specifications and design data of the worked PM motor

Frame	143 T
Power rating	1 hp
Line voltage	208 V
Rated current	3 A
Base speed	1800 rpm
No. of phases	3
No. of poles	4
No. of stator slots	36
No. of cage slots	44
Conductors/slot	42
No. of series turns/phase	254
Connection	Y
Winding layout	double layer
Chording	1-8
Stator outer diameter	147.3 mm
Stator bore diameter	93.5 mm
Airgap	0.45 mm
Rotor inner diameter	31.4 mm
Rotor length	78.8 mm
Magnet dimensions (cross section)	$7.7 \times 32.5\ mm^2$
Moment inertia	$0.0032\ kg - m^2$

Appendix F.

Since finite element analysis is limited to 2D, the end effects due to the end-ring resistance were treated by a modification of the rotor bar conductivity, and the end ring leakage flux has been accounted for by end ring leakage inductance as mentioned in section 4.3.

The lumped synchronous and starting parameters were then extracted from the static field solutions and eddy-current field solutions, respectively. The availability of these accurate parameters has made it possible to provide complete analysis

of synchronous performance and starting performance in terms of governing equations (2.12), (2.30) and (2.31). along with the torque equation (2.19).

6.2 Synchronous Performance Investigation

The calculated values of load-dependent parameters, X_d, X_q and E_0, using the proposed loading method, are shown in Fig. 6.3 by the dashed lines. The solid lines in Fig. 6.3 are the corresponding experimental values obtained from the new load test method. The operating point where the d-axis armature reaction is changing from magnetizing to demagnetizing region is around 48° of torque angle. It is noted that at the torque angle around 25°, there exists a dip on the E_0 curve and a crest on the X_d curve. This phenomenon can be readily appreciated by comparing the flux distributions between two different operating points as shown in Fig. 6.4, in which we have introduced programming technique to isolate the d-axis component and the magnet component from the resultant load fields. Due to the fact that this irregular operating point lies in the magnetizing region of the d-axis armature reaction, and the direction of the armature reaction flux in the inter-pole ferromagnetic bridge of the magnets is opposite to the direction of the leakage flux of the magnets. Even so, under most of its operating range, the small magnet leakage flux can easily make this narrow ferromagnetic bridge highly saturated. Thus, the main path of the d-axis component of armature reaction is across the magnet or the inter-pole magnetic barrier, resulting in a very large reluctance. However, under certain load condition (for this particular example, around 25°), these two flux components in the opposite direction turn out to be somewhat balanced and make the magnetic bridge become least saturated. As a result, the leakage flux of the magnets across

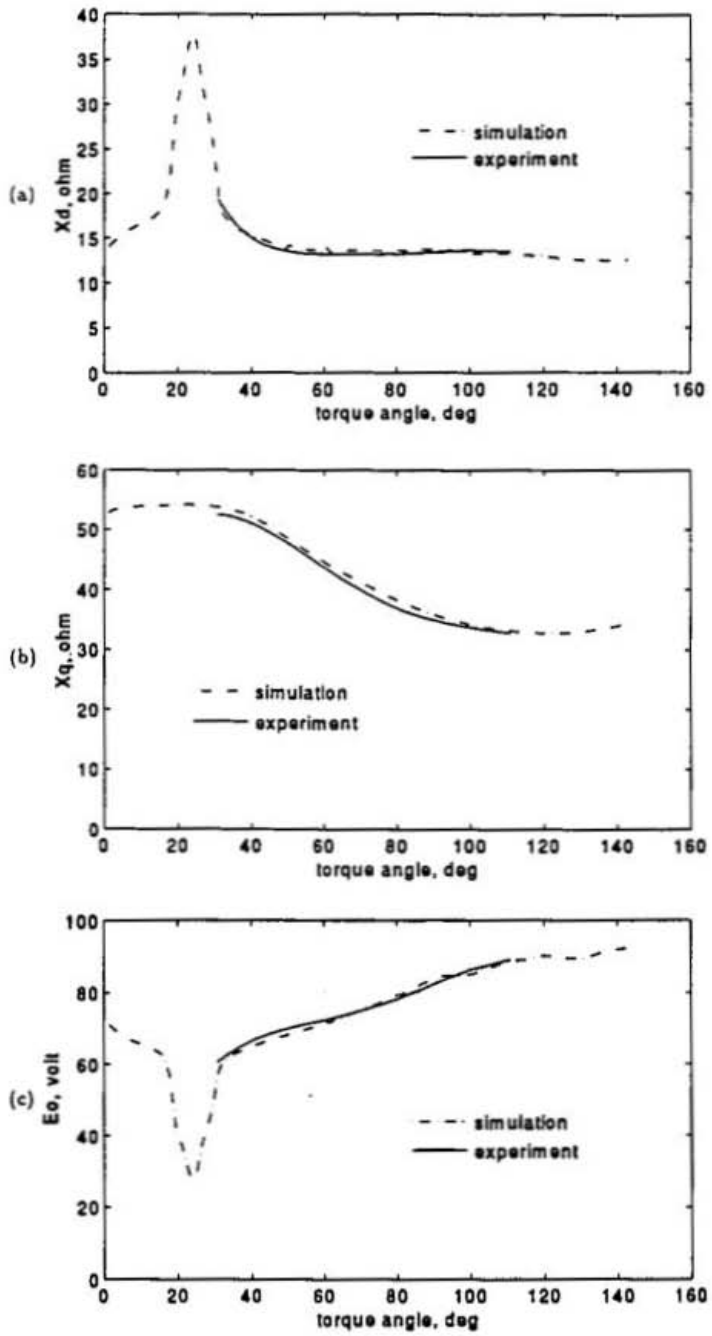

Figure 6.3: Variation of X_d, X_q and E_0 with load angle δ

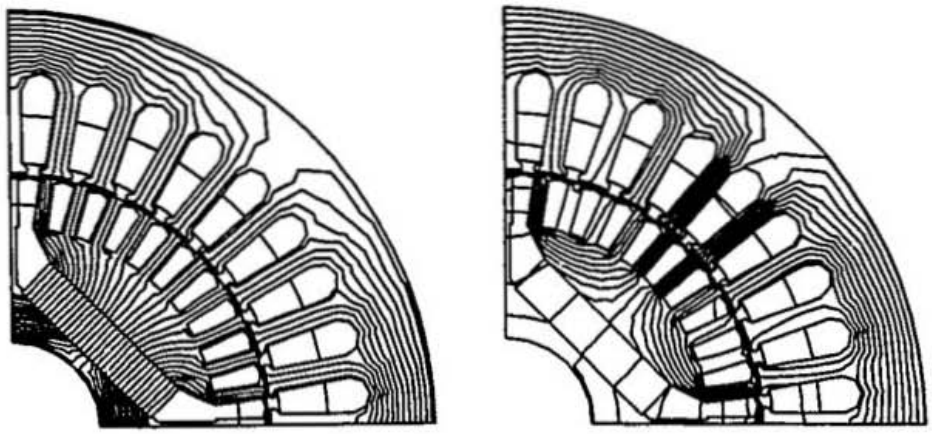

magnet component d-axis component

(a) at load condition $\delta = 24.8°$

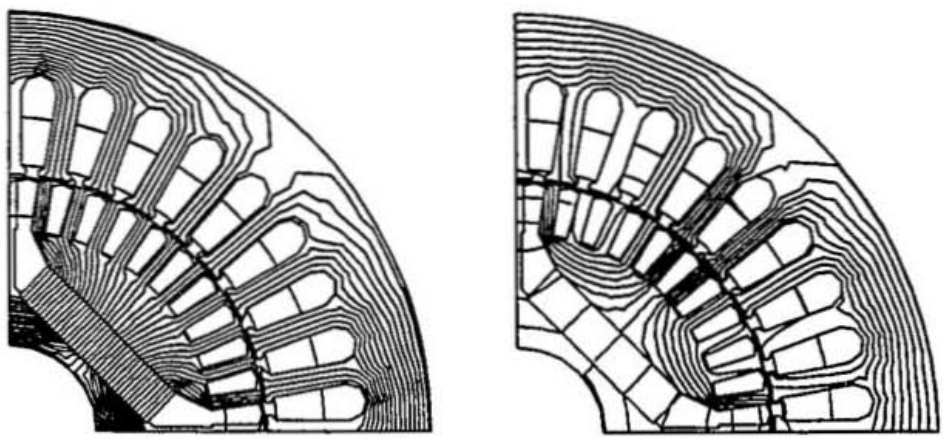

magnet component d-axis component

(b) at load condition $\delta = 38.1°$

Figure 6.4: Flux distribution comparison between two load conditions

the bridge increases rapidly. At the same time, the unsaturated bridge also provides a shortcut for the d-axis component of the armature reaction flux. Consequently, at this particular load condition, X_d increases notably with the considerable reduction of E_0.

It can also be noted from Fig. 6.3(c) that the magnet excitation voltage E_0 varies with load. The tendency for E_0 to increase is also attributed to the interaction between the magnet flux and the armature reaction flux. When the d-axis armature reaction changes from magnetizing to zero, and from less demagnetizing to heavy demagnetizing with the increase of the load, the main path of the magnet flux in the iron part becomes less saturated. In contrast, the leakage path of magnet flux in the inter-pole ferromagnetic bridge turns to be more and more saturated due to the same direction of these two flux components in the bridge region. As a result, both these two factors lead to the increase of the main magnet flux, thus increasing the value of E_0.

Figures 6.5 and 6.6 are the simulation results of torque characteristic and power factor when the worked PM motor is fed by current source supply at rated stator current, $I_1 = 3A$. It is clear from the torque versus torque angle curve that due to $X_d < X_q$, the pullout torque occurs at torque angle greater than 90°. For the same reason, the initial torque angle is far from zero value, being around 44° torque angle. It is noted from the power factor curve that for current source supply, the power factor can be controlled to any expected value, even in leading power factor region in favour of load commutation for an inverter-driven system. In this example, the leading power factor values are in the torque angle region greater than 152°.

Figures 6.7, 6.8 and 6.9 show the comparisons between the simulated and mea-

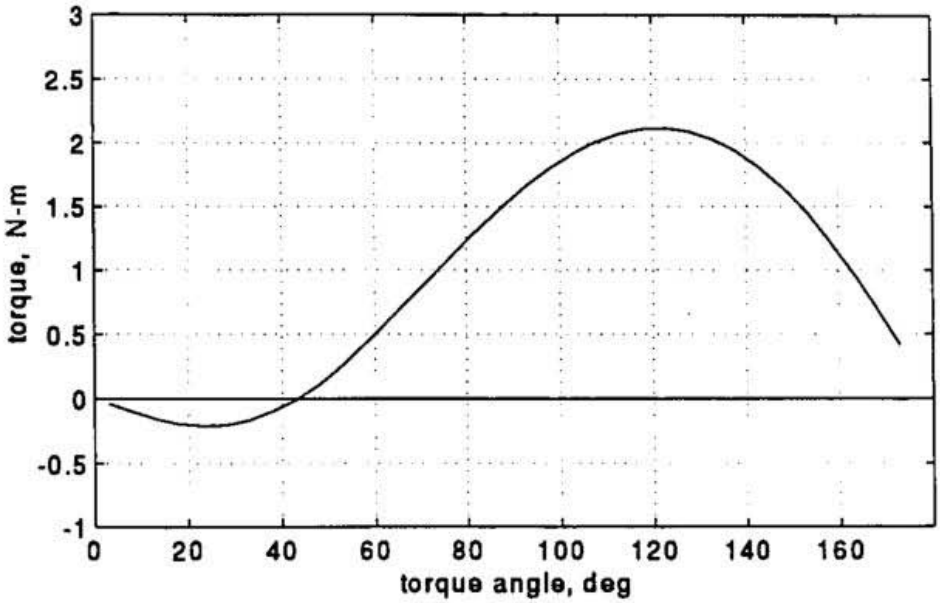

Figure 6.5: Torque characteristic fed from current source

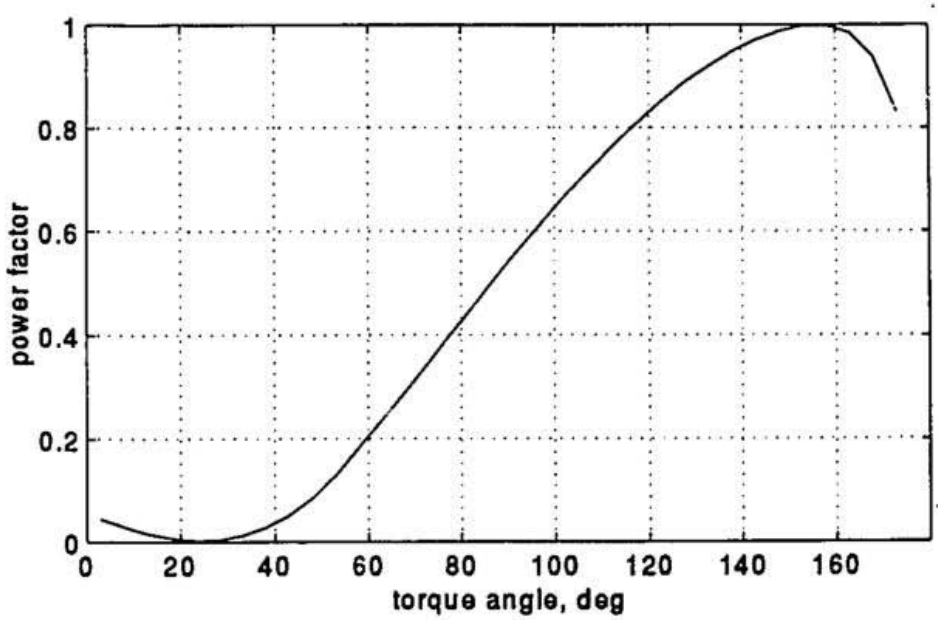

Figure 6.6: Power factor characteristic fed from current source

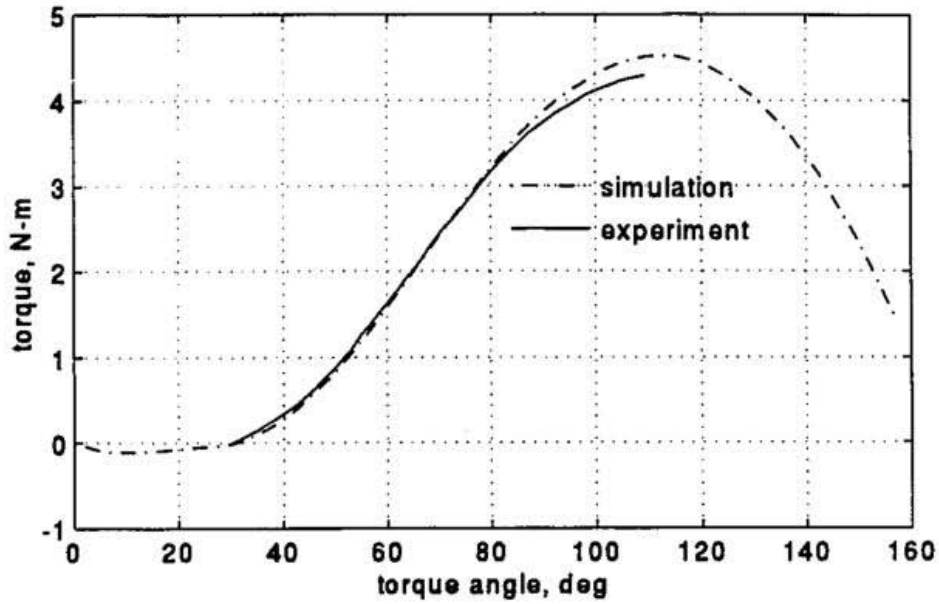

Figure 6.7: Simulated and measured results of torque characteristic fed from voltage source

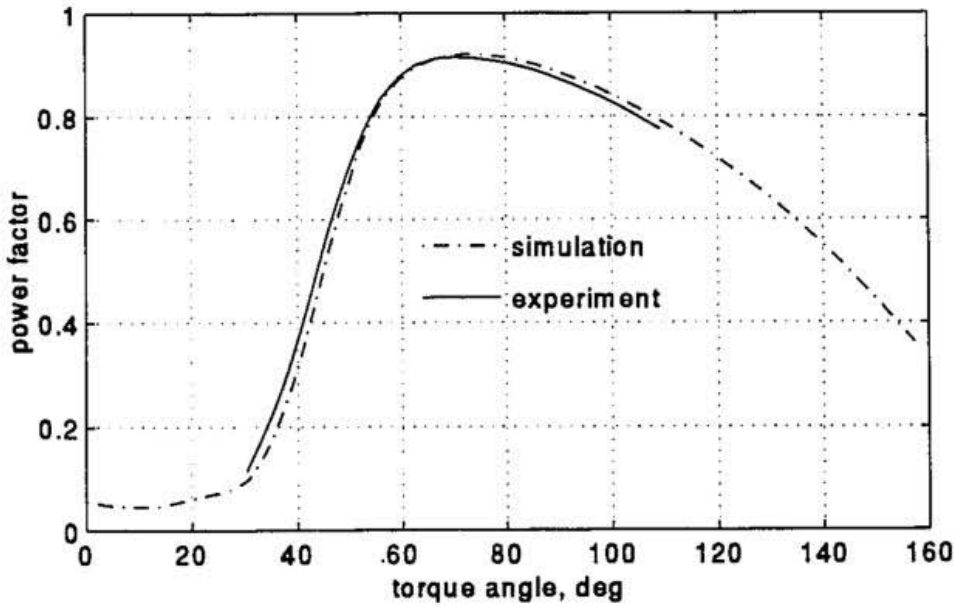

Figure 6.8: Simulated and measured results of power factor characteristic fed from voltage source

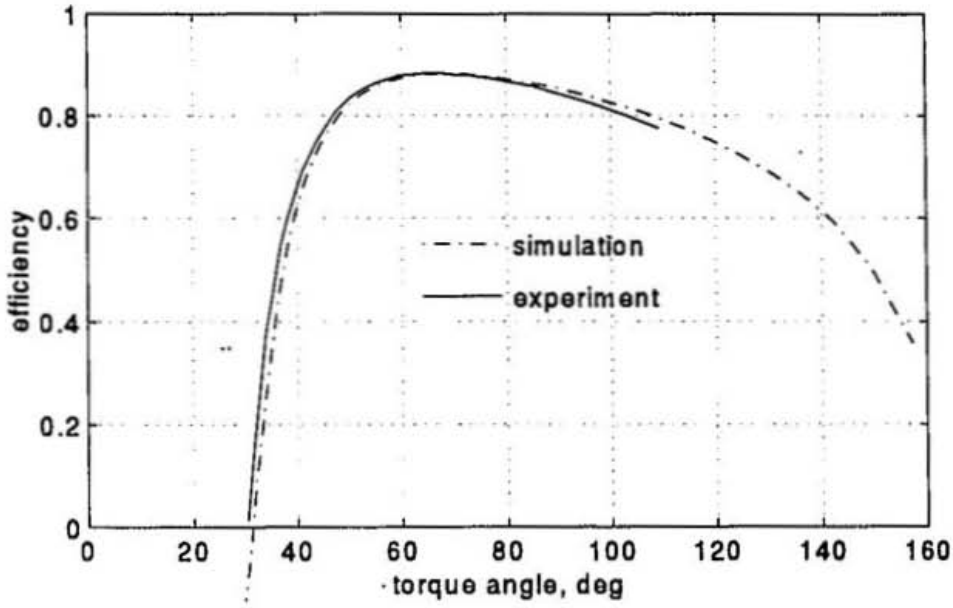

Figure 6.9: Simulated and measured results of efficiency characteristic fed from voltage source

sured torque characteristic, power factor and efficiency, respectively, when the PM motor was fed from voltage source. It is observed from Figs. 6.7–6.9 that excellent agreements between simulated and test results are achieved, except for the discrepancy of the torque values under heavy load. This discrepancy is mainly due to neglecting the thermally induced resistance variation in stator windings, which would appreciably degrade the capability of torque output with the considerable temperature rise at heavy load condition.

6.3 Starting Performance Investigation

In directly starting across the line, the motor must pull into synchronism from some subsynchronous speed to which the motor has just been accelerated by the asynchronous cage torque. Based on the eddy-current finite element solutions and using the established lumped parameter model, it is easy to carry out the starting performance investigation. Fig. 6.10 shows the flux distribution at $slip = 1$ instant. Also included in the Fig. 6.10 is a flux plot without eddy current flowing in the bar (simply let $\sigma_e = 0$) in order to observe the influence of eddy current on flux penetration. It can be seen from the comparison between these two figures that the skin effect is very strong and the induced eddy current in the bar caused most of the armature reaction flux to pass through rotor surface. The speed response of rotor parameters is displayed in Fig. 6.11. It is explicit from Fig. 6.11 that the skin effect and nonlinearity have significant effects on rotor starting parameters, thereby the starting performance.

The simulation results of pseudo-steady state torque versus speed characteristic is shown in Fig. 6.12. Average value means averaged over 360 electrical degree,

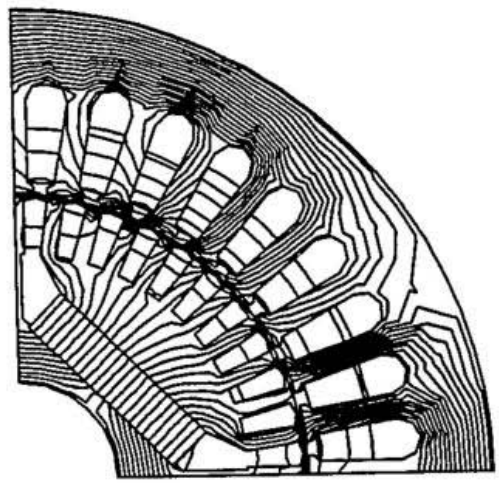

(a) considering eddy-current effects

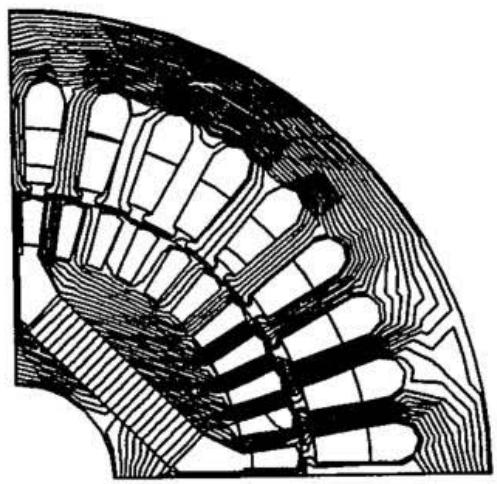

(b) without considering eddy-current effects

Figure 6.10: Flux distribution at $slip = 1$ instant

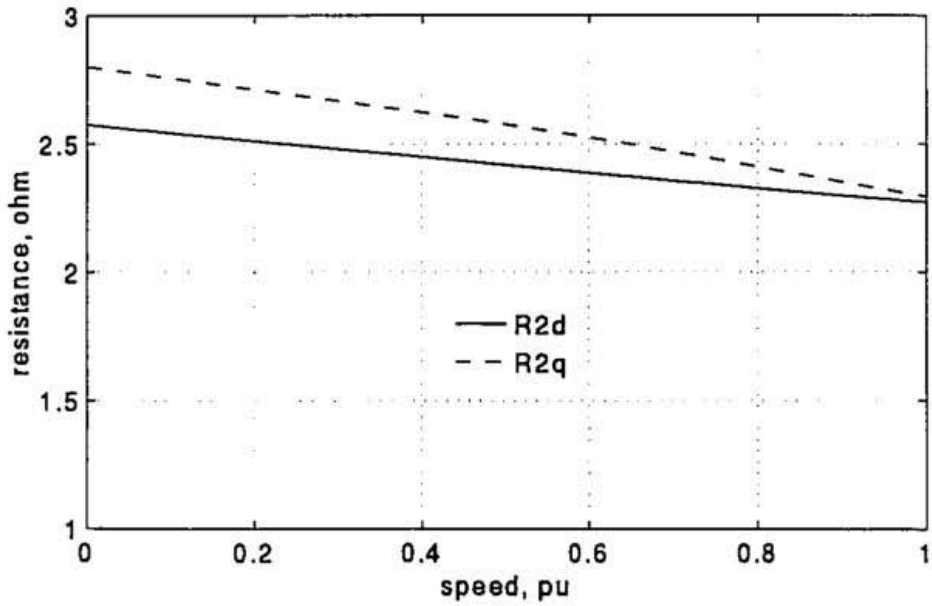

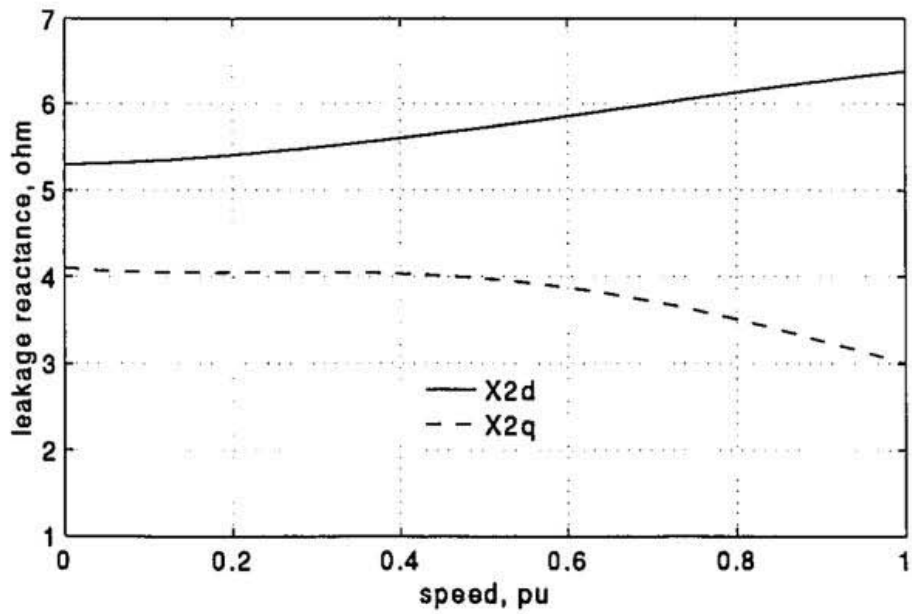

Figure 6.11: Speed response of rotor starting parameters

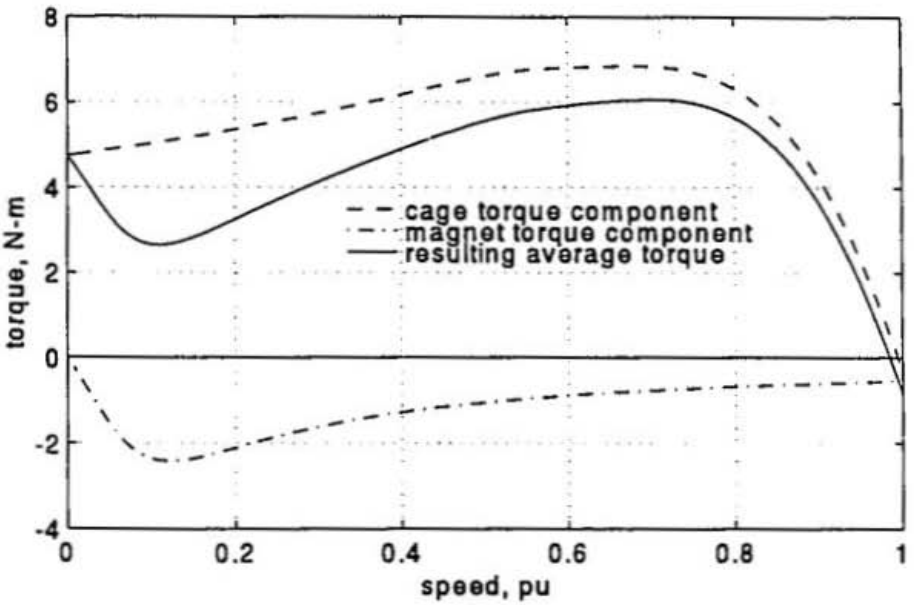

Figure 6.12: Average torque components

and it is assumed that acceleration rate is small enough not to affect the results. The cage torque component is the torque that would be obtained without the magnet braking torque component. The braking torque is nonzero at all speed except standstill, and tends to have a peak value at a fairly low speed. It is implied again from this example that the near half-speed torque dip doesn't exist when the dynamic parameters are employed in the analysis. But the impact of the magnet braking torque should be properly considered for the successful starting of a PM motor.

Figure 6.13 shows the simulation and measured results of starting current at no-load. It is noted that the measured values are slightly less than the ones from simulation after synchronization is achieved. This is mainly caused by the measurement errors, since the sensitivity of current transducer is not high enough for small current measurement due to cutoff effect. Figures 6.14, 6.15 and 6.16 show the simulation results of speed versus time, torque versus time and torque versus speed, respectively, at no-load. Since the tachogenerator is mounted on the load machine and the torque transducer is also coupled to the load machine, the measurement of the torque and speed is not accessible at no-load operation. The maximum current information is important for the rating demand of many types of inverters, avoiding permanent demagnetization of magnets and the proper setting of over-current relay. The time of run-up to stable synchronization needs to be specified for some applications involving high coupled inertia. The torque levels throughout run-up and particularly the pull-in torque can be deciding factors in the suitability of a motor for a particular application. Fortunately, all these engineering information can be found from the curves of Figs. 6.11-6.16 to evaluate and optimize the design

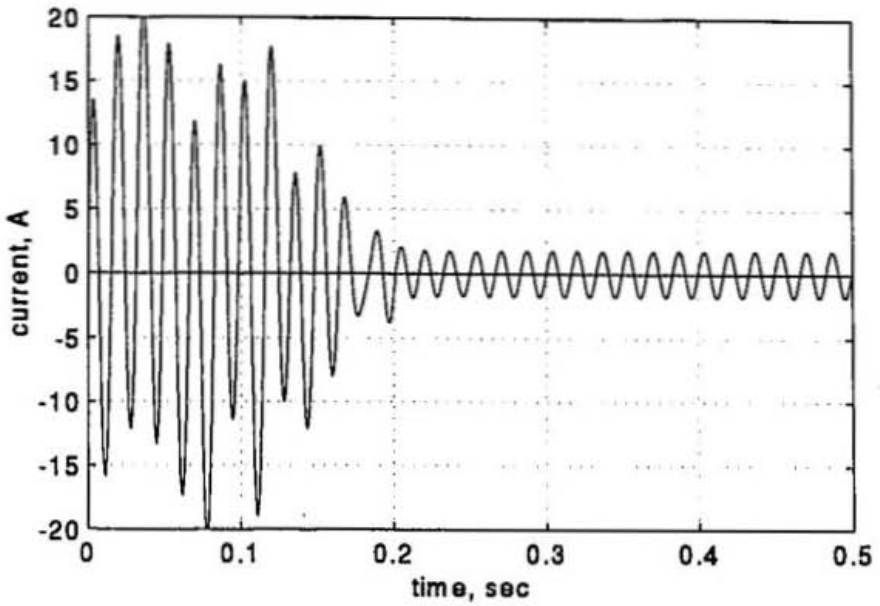

(a) simulation

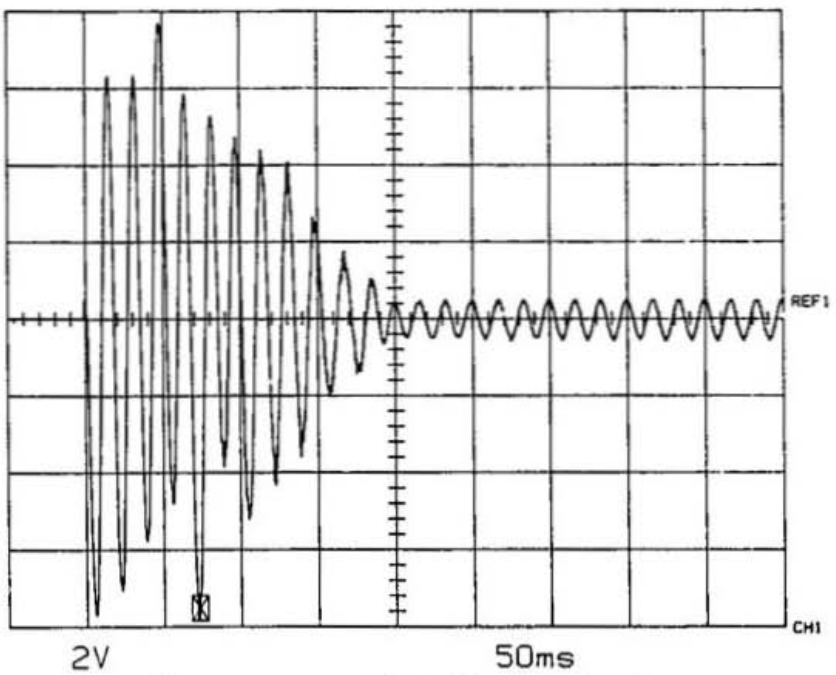

(b) measurement (5 A/div, 50 ms/div)

Figure 6.13: Simulated and measured results of starting current at no-load

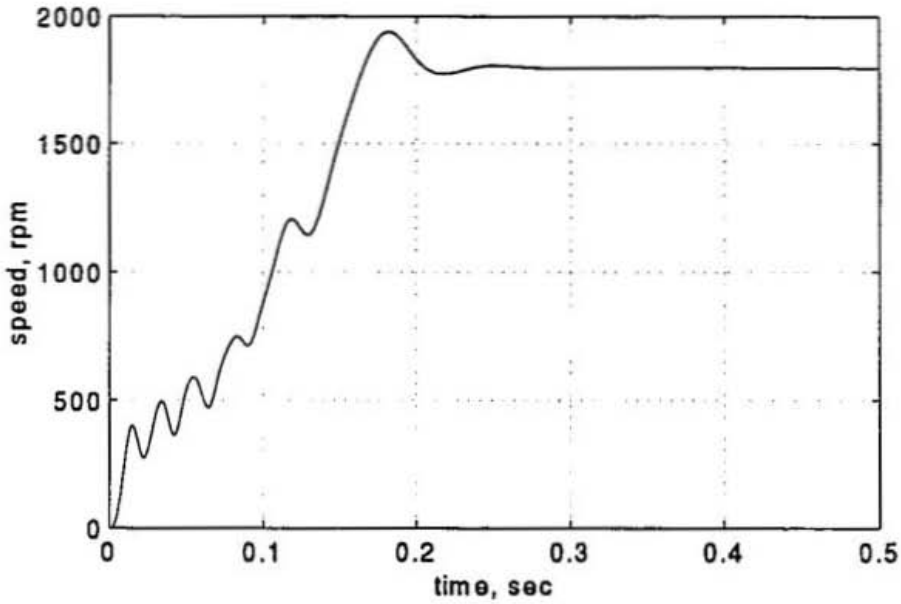

Figure 6.14: Simulation results of speed versus time at no-load

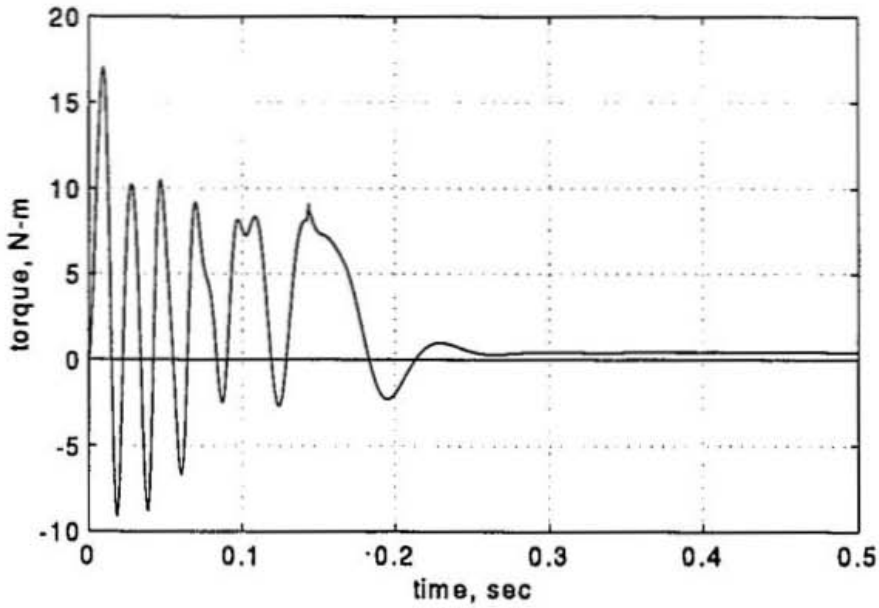

Figure 6.15: Simulation results of torque versus time at no-load

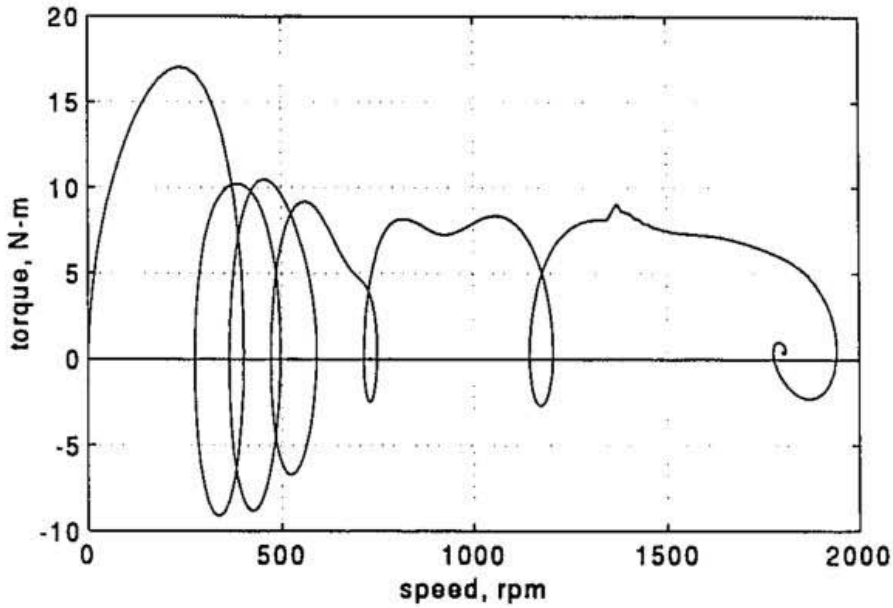

Figure 6.16: Simulation results of torque versus speed at no-load

for specified performances.

Figure 6.17 shows the simulated and measured result of speed versus time with a coupled load of about twelve times the rotor inertia, that is, $J_L = 0.039\ kg - m^2$. Figure 6.18 shows the simulated and measured result of torque versus time with the same load, and figure 6.19 shows the simulated and measured result of torque versus speed. Figure 6.20 gives the details of starting current obtained from simulation and measurement, respectively under the same load. It is observed that the agreement between the measured and simulated results is excellent. Synchronization of a PM motor is very complex because of the interaction of the inertia torque with two components of synchronizing torque, one due to the rotor saliency, the other due to the magnets. These two components can be additive or subtractive depending on the instantaneous angle between the rotor d-axis and the axis of stator MMF wave. It is obvious that the synchronization of this worked PM motor is accomplished successfully, and is well damped with little overshoot beyond synchronous speed. It is understandable that the effect of magnet flux level in PM machines is important. The higher the magnet flux the better the pull-in and pull-out torques will be, but the starting current and input kVA will require the magnet flux level to be kept within certain limits.

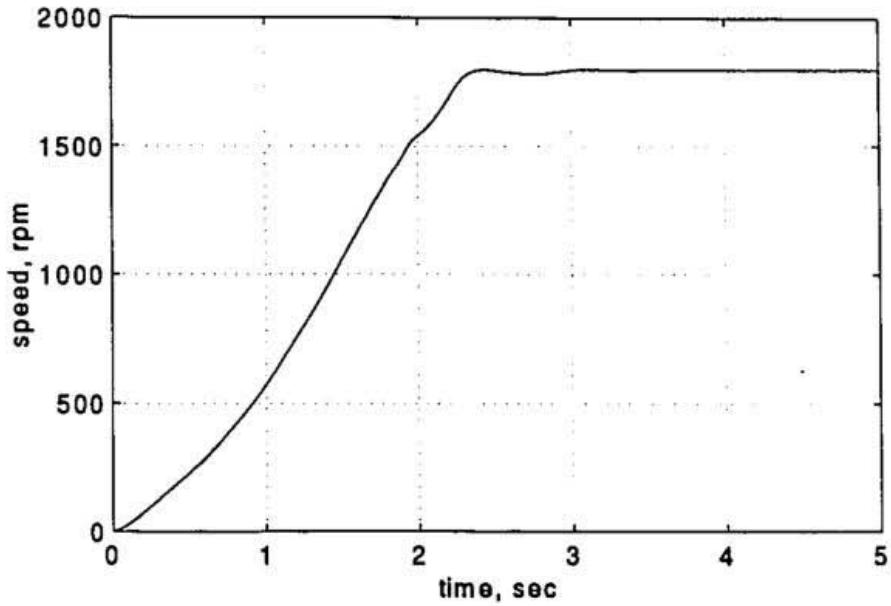

(a) simulation

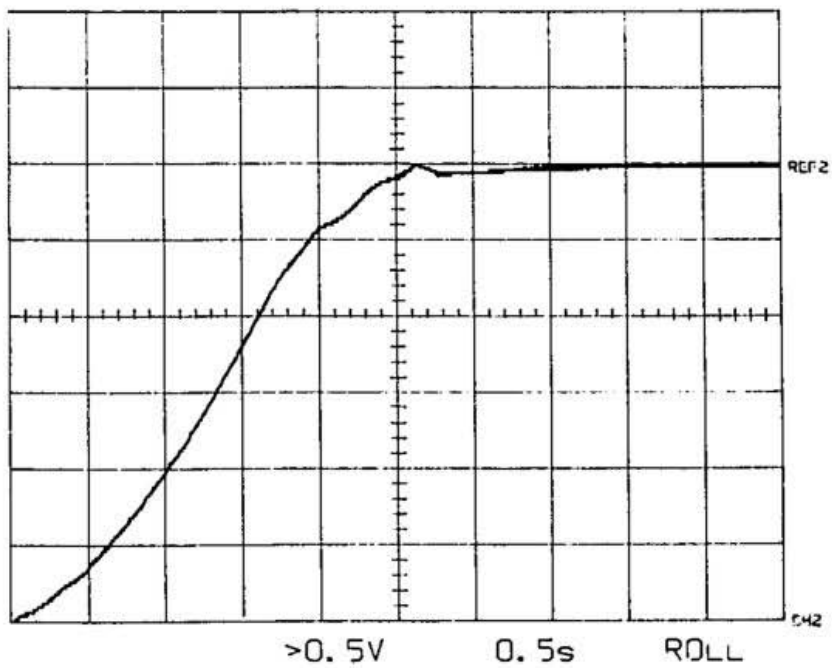

(b) measurement (300 rpm/div, 0.5 s/div)

Figure 6.17: Simulated and measured results of speed versus time with load

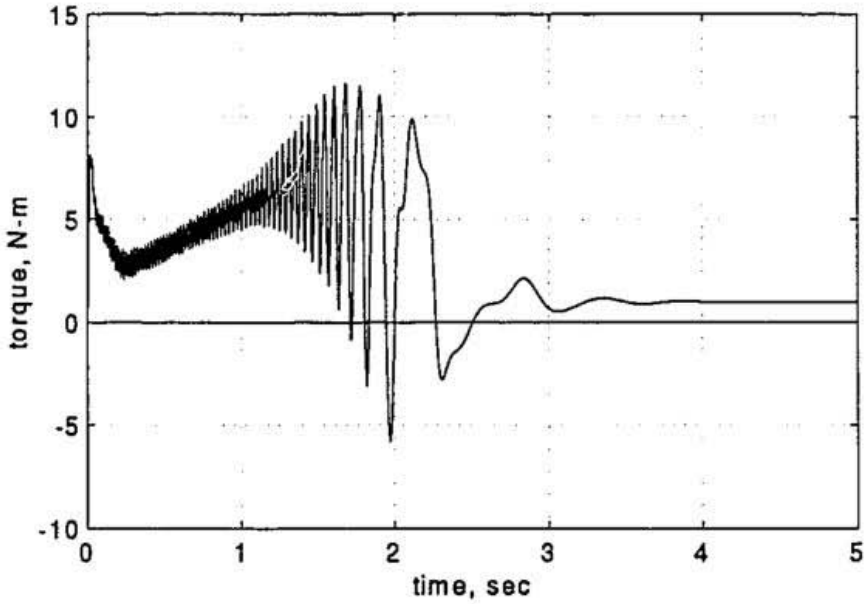

(a) simulation

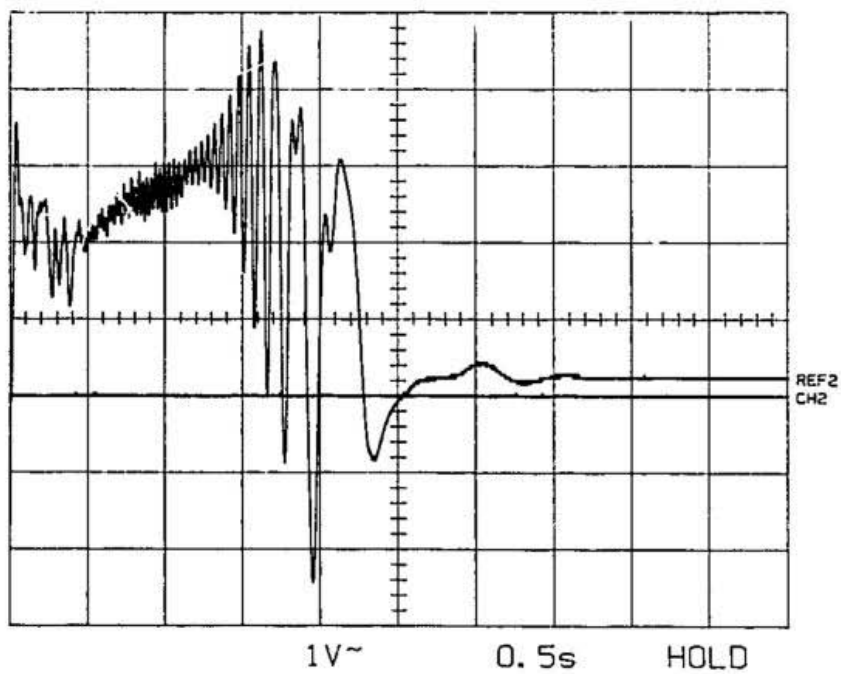

(b) measurement (2.5 N-m/div, 0.5 s/div)

Figure 6.18: Simulated and measured results of torque versus time with load

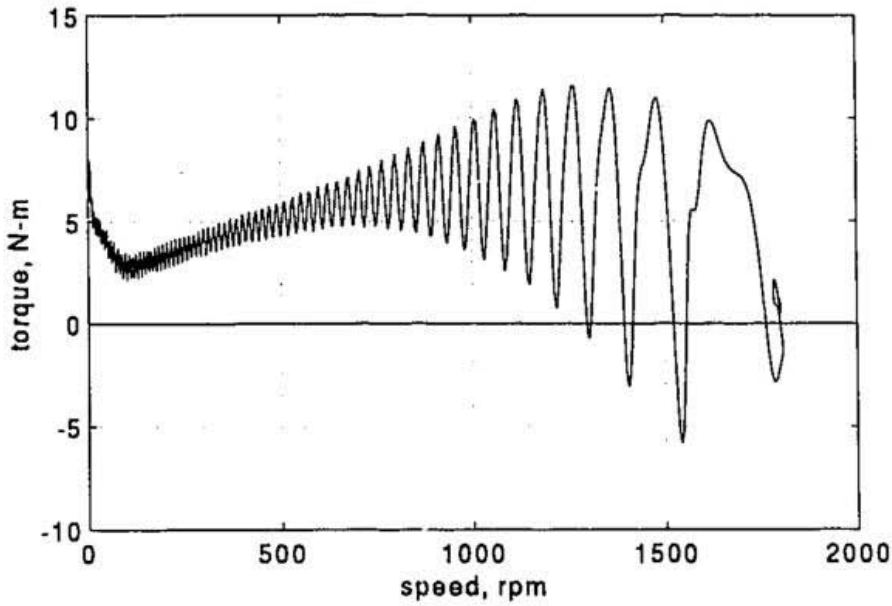

(a) simulation

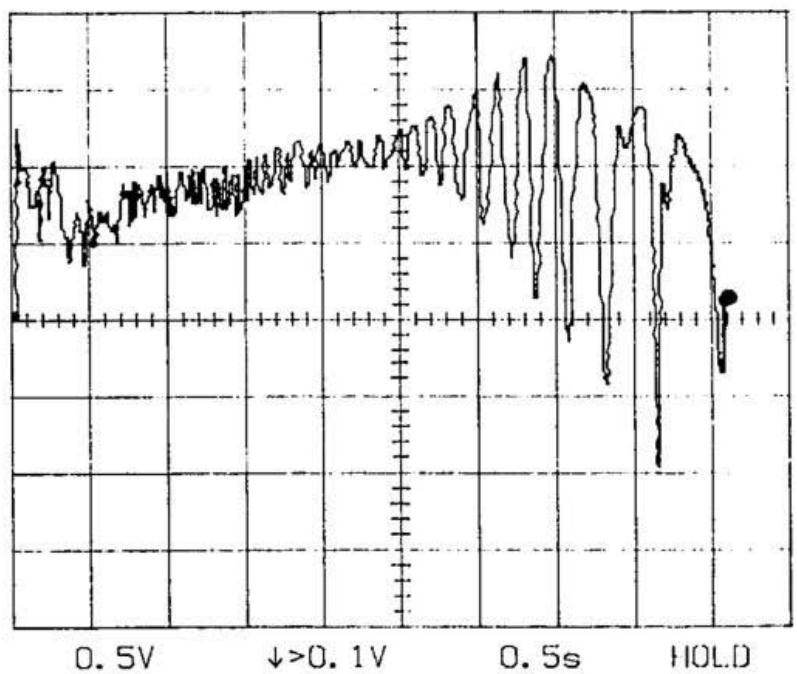

(b) measurement (3 N-m/div, 200 rpm/div)

Figure 6.19: Simulated and measured results of torque versus speed with load

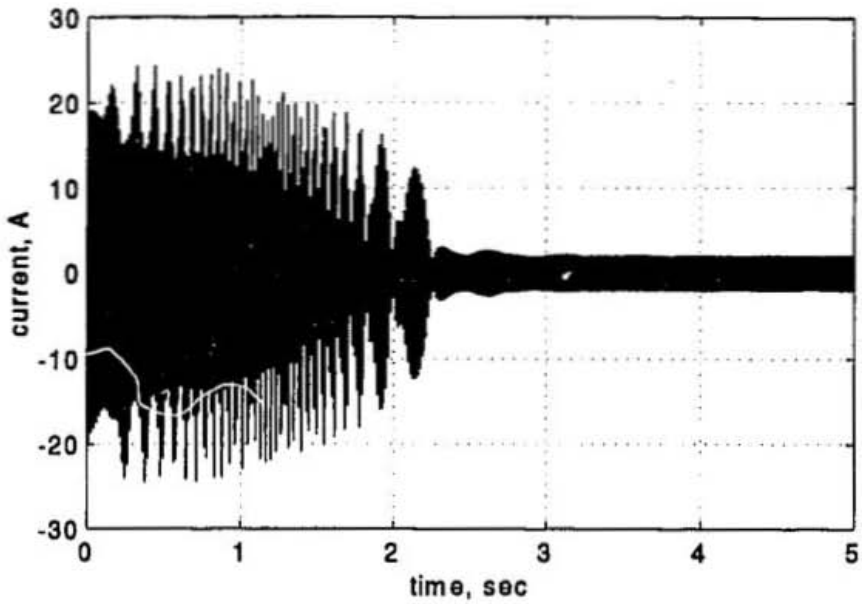

(a) simulation

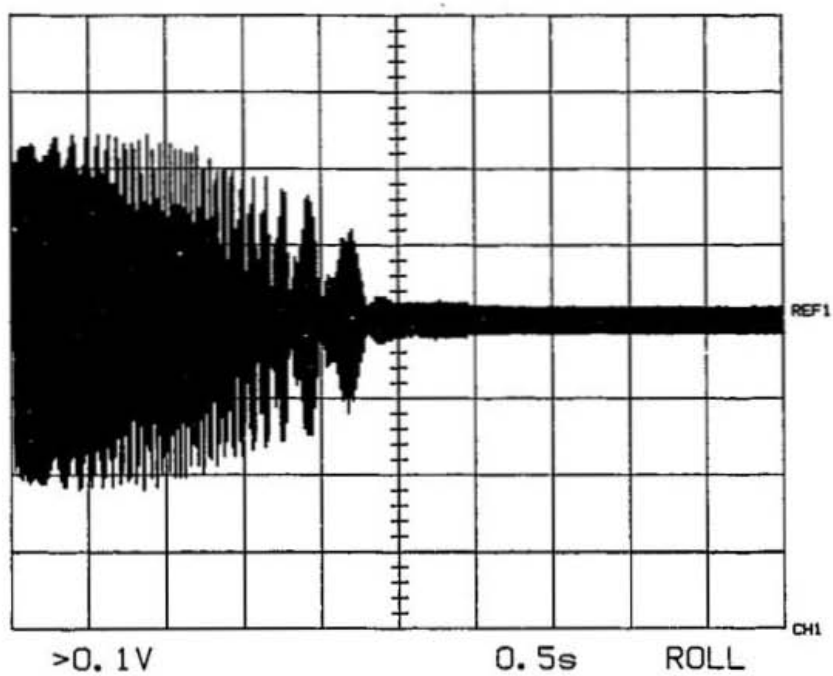

(b) measurement (10 A/div, 0.5 s/div)

Figure 6.20: Simulated and measured results of starting current with load

Chapter 7

Summary and Conclusion

In the design of interior-type permanent magnet motors, proper calculations of the starting and synchronous performance are necessary. Saturation, complex shape and placement of magnets and barriers, and the induced eddy currents in the rotor bars pose difficulties when traditional equivalent circuits and lumped parameter models are used. On the other hand, finite element analysis has the potential to overcome these difficulties. But this is a time-consuming process. Therefore, in this study a complete procedure is developed to combine the finite element analysis with lumped parameter circuit model to provide desirable engineering information but at minimum computational effort. The first stage in the analysis procedure is to develop a unified lumped parameter circuit model. The next stage is to extract individual lumped parameters from the corresponding finite element solutions. Therefore, the main difference between the proposed lumped parameter model and conventional equivalent circuit model is that in the former, all adopted lumped parameters are load and speed dependent, while in the latter, all the parameters are considered as constant even though it was recognized that assuming constant parameters is far from reality.

In chapter 2, using standard two-axis theory with fixed rotor reference frame and matrix transformation, a unified lumped parameter model is derived to provide the basis for the investigation of both the steady-state and dynamic performances. A per-phase equivalent circuit is introduced to account for the saliency of a PM motor and the influence of iron losses in favour of the synchronous performance calculation. The starting performance investigation has been completed by two approaches. One is the quasi-dynamic analysis with pseudo-constant speed characteristic. The other is the transient analysis characterized by state-variable equations.

Static field calculation and synchronous performance simulation have been discussed in chapter 3. For a PM motor fed from current source, different load conditions were simulated just by setting the corresponding initial phase angle β of stator current. For voltage source supply, since the value of stator current satisfying the prescribed terminal voltage for a specific load is not available until field solutions are obtained, a Newton-Raphson iterative algorithm in conjunction with a scheme for effective estimation of initial phase current value has been developed to accommodate the static field finite element model to a voltage source supply. Based on field solutions, a novel method has been proposed to determine the load-dependent parameters X_d, X_q and E_0, in which the effects of the interaction between the d-axis and q-axis fields are included. In addition, a flux method has been introduced for torque calculation so as to eliminate the sensitivity to mesh discretization. The effect of magnetic field distortion on iron losses has been accounted for by introducing eddy current and minor loop hysteresis correction factors.

In chapter 4, in order to alleviate the eddy-current field computation, time-phasor was applied to the make the finite element analysis independent of time

factor based on the introduction of equivalent reluctivity in terms of equivalent magnetic energy. The corresponding finite element formulae for the voltage source supply have then been derived with complete elimination of the troublesome iterative process for the starting current. Based on the eddy-current field solutions, a procedure for extracting the starting parameters has been developed. First, voltage-source finite element model was applied to get the starting current and stator leakage reactance. With the starting current determined, the current-source finite element model was applied to extract d-axis and q-axis magnetizing reactances and rotor starting parameters. Since in the starting process, the magnets do not induce eddy-current in the rotor part, the rotor starting parameters are determined in the absence of magnets. The effects of magnets on magnetic saturation have been taken into account by the introduction of auxiliary complex vector potential and auxiliary real vector potential. With accurate field-based starting parameters known, the lumped parameter model was then used to evaluate the starting performance. The average and pulsating torque components were obtained by means of quasi-dynamic analysis. Transient analysis approach was employed to obtain the speed response, transient torque, and instantaneous current during the run-up including the synchronization process.

The experimental study was carried out in chapter 5. A novel load test method has been proposed to determine the load-dependent parameters X_d, X_q and E_0 based on the measurement of load angle, input power and input current. This method not only takes into account the variation of E_0 with load and the interaction between the d-axis and q-axis quantities, but also is convenient to implement. The developed microprocessor-based torque angle measurement system is able to

provide fast transient response and adequate resolution for measuring and control applications. This designed and built prototype system is general and can be used for both motoring and generating modes for all kinds of synchronous machines. A scheme of accurately locating the position of zero torque angle has been developed to ensure the accuracy of the torque angle measurement but with no need for the accessibility to the internal construction of a PM motor.

A practical application example was presented in chapter 6 to show the usefulness of the developed analysis and test techniques in chapter 2 to 5. The detailed experimental and simulation results of starting and synchronous performances have been given with regard to a 1 hp laboratory PM synchronous motor. It is shown that experimental and simulation results are in excellent agreement.

In short, the major contributions of this thesis are:

- A complete procedure to combine finite element analysis with lumped parameter circuit model.
- A unified lumped circuit model applicable for both steady-state and transient operations.
- A new simulation method for determining the load-dependent parameters X_d, X_q and E_0.
- Improved eddy-current finite element formulae directly starting with voltage source.
- A novel approach for obtaining the starting current and starting parameters.

- A new test method for determining the load-dependent parameters X_d, X_q and E_0.
- A novel microprocessor-based load angle measurement system.
- A novel scheme for locating the position of zero torque angle.

Some major conclusions of this study are:

- Field and circuit combined analysis is a feasible, accurate and efficient approach for the simulation of starting and synchronous performances of permanent magnet synchronous machines.
- Saturation can cause significant variation in magnet excitation and d-axis and q-axis synchronous reactances. Therefore, there is a need for more knowledge of parameters than is usually sufficient for conventional synchronous machines, with particular attention to the effects of ferromagnetic bridge due to its easily changeable saturation state.
- The irregularity of X_d value over a load range is caused by the assumption of constant E_0. The assumption that any one or more of the parameters X_d, X_q or E_0 are constant can lead to significant errors in the motor performance predictions.
- The previous concern that there exists a dip near half speed on the average torque curve is unwarranted due to the fact that skin effect may favourably make rotor dynamic parameters much less unsymmetric.

- The error of positioning the zero torque angle caused by using the approximate method is not too small to be neglected for precision measurement and high quality control applications.

This study has focused only on the sinusoidal inverter source supply. But, in practical inverter drive applications, the existence of harmonics is unavoidable. Fortunately, the effects of harmonics on motor performance may still be properly assessed during the performance evaluation by using circuit models in conjunction with certain modification of individual lumped parameters according to the harmonic frequency being considered. However, in the case of high quality motor drive fed from a supply with large harmonic components, it is desirable to use more adequate simulation model. Thus, some of the suggested further works may include the following:

- Modeling of harmonics in stator mmf including both time and space harmonics.

- Prediction of cogging torque arising from the interaction between mmf harmonics and airgap permeance harmonics[46].

- Experimental investigation of the effects of harmonics on motor performance, inverter power capability and control strategies.

Bibliography

[1] M.A. Rahman and G.R. Slemon, *The promising applications of* NdBFe *magnets in electrical machines*(Invited), IEEE Trans. on Magnetics, Vol. MAG-21, No.5, pp. 1712-16, 1985.

[2] T. Sebastian, G.R. Slemon and M.A. Rahman, *Design considerations for variable speed permanent magnet motors*, Proc. International Conf. on Electrical Machines, pp. 1099-1102, 1986.

[3] V.B. Honsinger, *The fields and parameters of interior type ac permanent magnet machines*, IEEE Trans. on Power Apparatus and Systems, Vol. PAS-101, No.4, pp. 867-876, 1982.

[4] M.A. Rahman, T.A. Little and G.R. Slemon, *Analytical models for interior-type permanent magnet synchronous motors*, IEEE Trans. on Magnetics, Vol. MAG-21, No.5, pp. 1741-43, 1985.

[5] G.R. Slemon and A.V. Gumaste, *Steady-state analysis of a permanent magnet synchronous motor drive with current source inverter*, IEEE Trans. on Industry Applications, Vol. IA-19, No.2, pp. 190-197, 1983.

[6] A.V. Gumaste and G.R. Slemon, *Steady-state analysis of a permanent magnet synchronous motor drive with voltage source inverter*, IEEE Trans. on Industry Applications, Vol. IA-17, No.2, pp. 143-151, 1981.

[7] M.A. Rahman and A.M. Osheiba, *Performance of large line-start permanent magnet synchronous motors*, IEEE Trans. on Energy Conversion, Vol. EC-5, No.1, pp. 211-217, 1990.

[8] V.B. Honsinger, *Performance of polyphase permanent magnet machines*, IEEE Trans. on Power Apparatus and Systems, Vol. PAS-99, No.4, pp. 1510-18, 1980.

[9] V.B. Honsinger, *Permanent magnet machines: Asynchronous operation*, IEEE Trans. on Power Apparatus and Systems, Vol. PAS-99, No.4, pp. 1503-109, 1980.

[10] A. Consoli and A. Abela, *Transient performance of permanent magnet ac motor drives*, IEEE Trans. on Industry Applications, Vol. IA-22, No.1, pp. 32-41, 1986.

[11] T.J.E. Miller, *Transient performance of permanent magnet ac machines*, IEEE Industry Application Society Annual Meeting Conf. Record, pp. 500-503, 1986.

[12] M.V.K. Chari, G. Bedrosian and J. D'Angelo, *Finite element application in electrical engineering*, IEEE Trans. on Magnetics, Vol. MAG-29, No.2, pp. 1304-1314, 1993.

[13] P. Silvester and M.V.K. Chari, *Finite element solution of saturable magnetic field problems*, IEEE Trans. on Power Apparatus and Systems, Vol. PAS-89, No.7, pp. 1642-51, 1970.

[14] M.V.K. Chari and Z.J. Csendes, *Finite element analysis of the skin effect in current carrying conductors*, IEEE Trans. on Magnetics, Vol. MAG-13, No.5, pp. 1125-27, 1977.

[15] P. Silvester and R.L. Ferrari, *Finite elements for electrical engineers*, Cambridge University Press, 1990.

[16] F.A. Fouad, T.W. Nehl and N.A. Demerdash, *Magnetic field modeling of permanent magnet type electrically operated synchronous machines using finite element*, IEEE Trans. on Power Apparatus and System, Vol. PAS-100, No.9, pp. 4125-35, 1981.

[17] P. Silvester, H.S. Cabayan and B.T. Browne, *Efficient techniques for finite-element analysis of electrical machines*, IEEE Trans. on Power Apparatus and Systems, Vol. PAS-92, No.4, pp. 1274-81, 1973.

[18] D. Shen, G. Meunier and J.L. Coulomb, *Solution of Magnetic fields and electrical circuits combined problems*, IEEE Trans. on Magnetics, Vol. MAG-21, No.6, pp. 2288-91, 1985.

[19] E. Vassent, G. Meunier and A. Foggia, *Simulation of induction machines using complex magnetodynamics finite element coupled with the circuit equations*, IEEE Trans. on Magnetics, Vol. MAG-27, No.5, pp. 4246-49, 1991.

[20] T.W. Nehl, F.A. Fouad, N.A. Demerdash and E.A. Maslowski, *Dynamic simulation of radially-oriented permanent magnet type electronically operated synchronous machines with parameters obtained from finite element field solutions*, IEEE Trans. on Industry Applications, Vol. IA-18, No.2, pp. 172-182, 1982.

[21] K.J. Binns and T.M. Wang, *Analysis and performance of a high-field permanent-magnet synchronous machine*, Proc. IEE, Vol. 131, Part B, No.6, pp. 252-258, 1984.

[22] B.J. Chalmers, S.A. Hamed and G.D. Baines, *Parameters and performance of a high-field permanent-magnet synchronous motor for variable-frequency operation*, Proc. IEE, Vol. 132, Part B, No.3, pp. 117-124, 1985.

[23] T.J.E. Miller, *Methods for testing permanent magnet polyphase ac motor*, IEEE Industry Application Society Annual Meeting Conf. Record, pp. 494-499, 1981.

[24] J. Mizia, K. Adamiak, A.R. Eastham and G.E. Dawson, *Finite element force calculation: comparison of method for electric machines*, IEEE Trans. on Magnetics, Vol. MAG-24, No.1, pp. 447-450, 1988.

[25] K.J. Binns, C.P. Riley and M. Wong, *The efficient evaluation of torque and field gradient in permanent magnet machines with small airgap*, IEEE Trans. on Magnetics, Vol. MAG-21, No.6, pp. 2435-38, 1985.

[26] J.L. Coulomb and G. Meunier, *Finite element implementation of virtual work principle for magnetic or electric force and torque computation*, IEEE Trans. on Magnetics, Vol. MAG-20, No.1, pp. 1894-96, 1984.

[27] J. Marinescu and N. Marinescu, *Numerical computation of torque in permanent magnet motors by Maxwell stress and energy method*, IEEE Trans. on Magnetics, Vol. MAG-24, No.1, pp. 463-466, 1988.

[28] L. Chang, A.R. Eastham and G.E. Dawson, *Permanent magnet synchronous motors: finite element torque calculation*, IEEE Industry Applications Society Annual Conference Record, pp. 69-73, 1989.

[29] M.A. Rahman, A.M. Osheiba and M.A. Choudhury, *Run-up response of polyphase permanent magnet synchronous motors*, Electric Machines and Power Systems Journal, Vol. 9, pp. 347-356, 1985.

[30] S.C. Tandon, A.F. Armor and M.V.K. Chari, *Nonlinear transient finite element field computation for electrical machines and drives*, IEEE Trans. on Power Apparatus and systems, Vol. PAS-102, No.5, pp. 1089-95, 1983.

[31] T.W. Preston, A.B.J. Reece and P.S. Sangha, *Induction motor analysis by time-stepping techniques*, IEEE Trans. Magnetics, Vol. MAG-21, No.1, pp. 471-474, 1988.

[32] K. Miyashita, S. Yamashita, T. Shimozu and H. Sento, *Development of a high speed 2-pole permanent magnet synchronous motor*, IEEE Trans. on Power Apparatus and System, Vol. PAS-99, No.6, pp. 2175-80, 1980.

[33] S.F. Gorman, C. Chen and J.J. Cathey, *Determination of permanent magnet synchronous motor parameters for use in brushless dc motor drive analysis*, IEEE Trans. on Energy Conversion, Vol. EC-3, No.3, pp. 674-681, 1988.

[34] D. Pavlik, V.K. Garg, J.R. Repp and J. Weiss, *A finite element technique for calculating the magnet sizes and inductances of permanent magnet machines*, IEEE Trans. on Energy Conversion, Vol. EC-3, No.1, pp. 116-122, 1988.

[35] P.H. Mellor, F.B. Chaban and K.J. Binns, *Estimation of parameters and performance of rare-earth permanent-magnet motors avoiding measurement of load angle*, Proc. IEE, Vol. 138, Part B, No.6, pp. 322-330, 1991.

[36] S. Williamson, *Induction motor modeling using finite elements,* Proceedings of International Conference on Electrical Machines, France, pp. 1-8, 1994.

[37] N.N. Hancock, *Matrix analysis of electrical machinery* , Pergamon Press, 1974.

[38] M.V.K. Chari and P.P. Silvester, *Finite elements in electrical and magnetic field problems*, Chichester: John Wiley, 1981.

[39] Tomy Sebastian and Gordon R. Slemon, *Operating limits of inverter-driven permanent magnet motor drives*, IEEE Trans. on Industry Applications, Vol. IA-23,No.2, pp. 327-333, 1987.

[40] M.A. Rahman and P. Zhou, *Determination of saturated parameters of PM motors using loading magnetic fields*, IEEE Trans. on Magnetics, Vol. MAG-27, No.5, pp. 3947-50, 1991.

[41] J.D. Lavers, P.P. Biringer and H. Hollitscher, *A simple method of estimating the minor loop hysteresis loss in thin laminations*, IEEE Trans. on Magnetics, Vol. MAG-14, No.5, pp. 386-388, 1978.

[42] E. Levi, *Polyphase motors*, Chichester: John Wiley, 1984.

[43] Ping Zhou, M.A. Rahman and M.A. Jabbar, *Field circuit analysis of permanent magnet synchronous motors*, IEEE Trans. on Magnetics, Vol. MAG-30, No.3, pp. 1350-1359, 1994.

[44] M.A. Rahman and Ping Zhou, *Field-based analysis for permanent magnet motors*, IEEE Trans. on Magnetics, pp. 3664-3667, 1994.

[45] M.A. Rahman and Ping Zhou, *Accurate determination of PM motor parameters by digital torque angle measurement*, Journal of Applied Physics, 76, No.10, 1994.

[46] Z.Q. Zhu and D. Howe, *Analytical prediction of the cogging torque in radial-field permanent magnet brushless motors*, IEEE Trans. on Magnetics, Vol. MAG-28, No.2, pp 1371-1374, 1992.

[47] D.A. Lindholm, *Automatic Triangular Mesh Generation on Surfaces of polyhedra*, IEEE Trans. on Magnetics, Vol. MAG-19, No.6, pp 2539-42, 1983.

[48] Z.J. Cendes, D. Shenton and H. Shahnasser, *Magnetic field computation using Delaunay triangulation and complementary finite element methods*, IEEE Trans. on Magnetics, Vol. MAG-19, No.6, pp 2551-54, 1983.

Appendix A

Static Inductance Method

The measurement circuit shown in Fig. A.1 is composed of two non-inductive resistors (r_3 and r_4) and one variable non-inductive resistor (r_2) used to balance the bridge circuit. The r_1 and L represent the resistor and self-inductance of the stator winding. When the switch is closed with the rotor and stator aligned along the d-axis (or q-axis), a constant current I established a field in the stator winding. After balancing the bridge (i.e. $v_{ab} = 0$) and then opening the switch the current I through the inductor will fall exponentially to zero. Assuming V_{ab} is the instantaneous voltage across the bridge during this transient period, then,

$$v_{r3} = r_3 \frac{v}{r_3 + r_4} \tag{A.1}$$

$$v_{r2} = r_2 [\frac{v}{r_1 + r_2} - \frac{1}{r_1 + r_2} L \frac{di}{dt}] \tag{A.2}$$

and

$$\begin{aligned} v_{ab} &= v_{r3} - v_{r2} \\ &= v[\frac{r_3}{r_3 + r_4} - \frac{r_2}{r_1 + r_2}] + \frac{r_2}{r_1 + r_2} L \frac{di}{dt} \end{aligned} \tag{A.3}$$

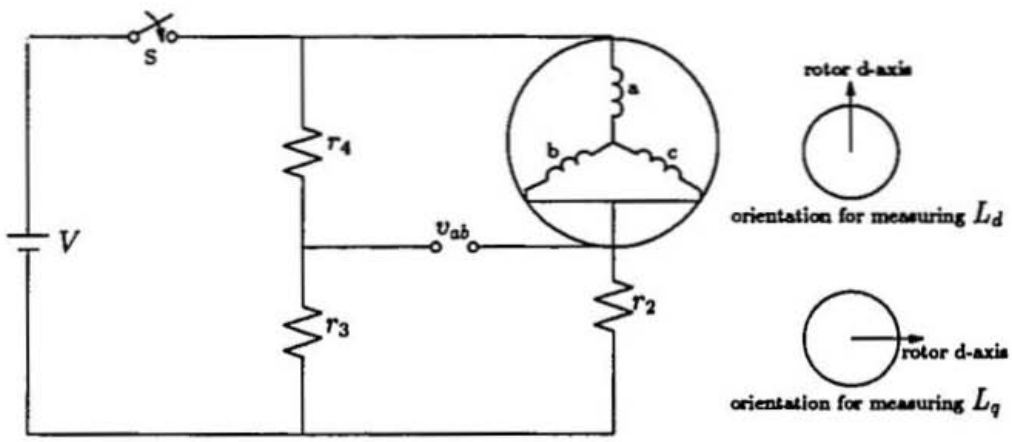

Figure A.1: Static inductance measurement circuit

Since the bridge is balanced,

$$\frac{r_3}{r_4} = \frac{r_2}{r_1} \tag{A.4}$$

Thus,

$$v_{ab} = (\frac{r_2}{r_1 + r_2}) L \frac{di}{dt} \tag{A.5}$$

The flux linkage can be obtained by integrating this transient voltage

$$\begin{aligned} \psi &= \int_0^\infty v_{ab}\, dt \\ &= \int_I^0 \frac{L r_2}{r_1 + r_2}\, dt \\ &= \frac{r_2}{r_1 + r_2} LI \end{aligned} \tag{A.6}$$

Therefore,

$$L = \frac{r_1 + r_2}{I r_1} \int_0^\infty v_{ab}\, dt \tag{A.7}$$

As a result, integrating the voltage across the bridge gives rise to the inductance along the axis of the alignment.

Appendix B

Variational Calculus

Variational calculus is concerned with the determination of unknown functions by extremizing integral expressions that contain those functions.

In order to derive the equivalent variational formulation to Poisson boundary-value problem in Eqn. (3.1), multiply every term of the first equation by the first variation δA of potential function A, and then the integration is performed over entire region Ω,

$$\iint_\Omega [\frac{\partial}{\partial x}(\nu\frac{\partial A}{\partial x}) + \frac{\partial}{\partial y}(\nu\frac{\partial A}{\partial y})]\,\delta A\,dx\,dy = -\iint_\Omega J\,\delta A\,dx\,dy \qquad \text{(B.1)}$$

Applying Green's theorem

$$\iint_\Omega (\frac{\partial P}{\partial x} + \frac{\partial Q}{\partial y})\,dx\,dy = \oint_s [P\cos(n,x) + Q\cos(n,y)]\,ds \qquad \text{(B.2)}$$

The left side of Eqn.(B.1) becomes

$$\begin{aligned}&\iint_\Omega [\frac{\partial}{\partial x}(\nu\frac{\partial A}{\partial x}) + \frac{\partial}{\partial y}(\nu\frac{\partial A}{\partial y})]\,\delta A\,dx\,dy \\ &= -\iint_\Omega \nu(\frac{\partial A}{\partial x}\frac{\partial \delta A}{\partial x}) + \frac{\partial A}{\partial y}\frac{\partial \delta A}{\partial y})\,dx\,dy + \oint_s \nu\frac{\partial A}{\partial n}\,\delta A\,ds \qquad \text{(B.3)}\end{aligned}$$

Substituting Eqn.(B.3) into Eqn.(B.1), one gets

$$\iint_\Omega \nu(\frac{\partial A}{\partial x}\frac{\partial}{\partial x}\delta A + \frac{\partial A}{\partial y}\frac{\partial}{\partial y}\acute{o}A)\,dx\,dy - \iint_\Omega J\,\delta A\,dx\,dy - \oint_s \nu\frac{\partial A}{\partial n}\,\delta A\,ds = 0 \qquad \text{(B.4)}$$

Using the properties of variation operator δ

$$\frac{\partial}{\partial x}\delta A = \delta(\frac{\partial A}{\partial x});\ \frac{\partial}{\partial y}\delta A = \delta(\frac{\partial A}{\partial y})$$

and

$$B = \sqrt{(\frac{\partial A}{\partial x})^2 + (\frac{\partial A}{\partial y})^2},$$

then

$$\begin{aligned}\iint_\Omega \nu(\frac{\partial A}{\partial x}\frac{\partial}{\partial x}\delta A + \frac{\partial A}{\partial y}\frac{\partial}{\partial y}\delta A)\,dx\,dy &= \iint_\Omega \nu[\frac{\partial A}{\partial x}\delta(\frac{\partial A}{\partial x}) + \frac{\partial A}{\partial y}\delta(\frac{\partial A}{\partial y})]\,dx\,dy \\ &= -\iint_\Omega \nu B\,\delta B\,dx\,dy \qquad \text{(B.5)}\end{aligned}$$

Without loss of generality, assuming the region Ω consists of two sub-regions Ω_a and Ω_b, the enclosed line integration path S comprises Dirichlet boundary s_1, Neumann boundary s_2 and the interface l_a and l_b which are essentially the same surface l but have equal and opposite normal vector $\bar{n}$. Then

$$\oint_s \nu\frac{\partial A}{\partial n}\delta A\,ds = \oint_{s1} \nu\frac{\partial A}{\partial n}\delta A\,ds + \oint_{s2} \nu\frac{\partial A}{\partial n}\delta A\,ds + \oint_l (\nu_a\frac{\partial A}{\partial n} - \nu_b\frac{\partial A}{\partial n})\,\delta A\,ds \qquad \text{(B.6)}$$

Considering

$$\delta A = 0 \quad \text{over } s_1 \qquad \text{(B.7)}$$

and

$$\nu\frac{\partial A}{\partial n} = -H_t = J_s \quad \text{over } s_2 \qquad \text{(B.8)}$$

as well as

$$\nu_a\frac{\partial A}{\partial n} - \nu_b\frac{\partial A}{\partial n} = H_a - H_b = J_s' \quad \text{over } l_l \qquad \text{(B.9)}$$

where J_s' denotes the surface current density which may exist over the interface, thus

$$\oint_s \nu\frac{\partial A}{\partial n}\delta A\,ds = \oint_{s2} \nu\frac{\partial A}{\partial n}\delta A\,ds + \oint_l J_s'\,\delta A\,ds \qquad \text{(B.10)}$$

If the interface which exists surface current density is also considered as generalized Neumann boundary, then Eqn. (B.10) can be reduced to the form

$$\oint_s \nu \frac{\partial A}{\partial n} \delta A \, ds = \int_{s2} J_s \, \delta A \, ds \tag{B.11}$$

Substitution of Eqn. (B.5) and Eqn. (B.11) into Eqn. (B.4) gives

$$\iint_\Omega \nu B \, dB \, dx \, dy - \iint_\Omega J \, \delta A \, dx \, dy - \int_{s2} J_s \delta A \, ds = 0 \tag{B.12}$$

The left hand side of Eqn. (B.12) can be viewed as the first variation δW of the functional W. Then, the original functional

$$W(A) = \iint_\Omega (\int_0^B \nu b \, db) \, dx \, dy - \iint_\Omega J A \, dx \, dy - \int_{s2} J_s A \, ds \tag{B.13}$$

It can be verified that

$$\delta^2 > 0 \tag{B.14}$$

Thus, Eqn.(B.13) corresponds to a minimum problem. Since Neumann boundary condition and interface condition have been implicitly satisfied in Eqn. (B.12), only Dirichlet boundary condition is to be constrained. Therefore, the equivalent conditional variation problem is given by

$$\begin{cases} W(A) = & \iint_\Omega (\int_0^B \nu b \, db - JA) \, dx \, dy - \int_{s2} J_s A \, ds = \min \\ s_1 : & A = A_0 \end{cases} \tag{B.15}$$

Appendix C

Virtual Work Principle Based Flux Method

For a conservative system, when the currents in the system are held fixed by suitable terminal voltage supply, the power equation can be expressed as

$$\{i\}^t\cdot\{v\} = \{i\}^t\cdot[R]\cdot\{i\} + \{i\}^t\cdot p([L]\cdot\{i\}) = \{i\}^t\cdot[R]\cdot\{i\} + \{i\}^t\cdot p[L]\cdot\{i\} \qquad \text{(C.1)}$$

where $\{i\}$ is the current vector; $\{v\}$ is the voltage vector; $\{i\}^t$ is the transpose of current vector $\{i\}$; [R] is the resistance matrix; [L] is the inductance matrix and p is the time-derivative operator $\frac{d}{dt}$. The second term of right hand side of Eqn. $(C.1)$ represents the sum of the rate of change of the magnetic stored energy and the mechanical power output converted from magnetic energy. If one allows an angular displacement $\Delta\theta$, inductance change $[\Delta L]$ will occur. Consequently, the change of magnetic stored energy is

$$\Delta W = \frac{1}{2}\{i\}^t\cdot([L]+[\Delta L])\cdot\{i\} - \frac{1}{2}\{i\}^t\cdot[L]\cdot\{i\} = \frac{1}{2}\{i\}^t\cdot[\Delta L]\cdot\{i\} \qquad \text{(C.2)}$$

According to the virtual work principle, the electromagnetic torque is given as

$$T_e = -\frac{\partial W}{\partial\theta} = \lim_{\Delta\theta\to 0} -\frac{1}{2}\{i\}^t\cdot(\frac{[\Delta L]}{\Delta\theta})\cdot\{i\} = -\frac{1}{2}\{i\}^t\cdot\frac{\partial[L]}{\partial\theta}\cdot\{i\}$$

$$= -\frac{1}{2}\{i\}^t \cdot \frac{\partial[L]}{\partial\delta} \cdot \frac{\partial\delta}{\partial\theta} \cdot \{i\} = -\frac{P}{2}\{i\}^t \cdot \frac{\partial[L]}{\partial\delta} \cdot \{i\}^t \qquad \text{(C.3)}$$

where power angle δ is in electrical degree. Introducing the synchronously rotating d-q axes system for a PM motor operating at synchronous speed, one obtains[37]

$$\frac{\partial[L]}{\partial\delta} = \begin{bmatrix} 0 & (L_d - L_q) & 0 \\ (L_d - L_q) & 0 & 1 \\ 0 & 1 & 0 \end{bmatrix} \qquad \text{(C.4)}$$

and

$$\{i\} = \{i_d, i_q, \psi_f\}^t \qquad \text{(C.5)}$$

where i_d, i_q are the equivalent d-axis and q-axis current components in the stator windings, respectively. ψ_f is the flux linkage produced by the permanent magnets. Substitution of $\frac{\partial[L]}{\partial\delta}$ and $\{i\}$ from Eqns. $(C.4)$ and $(C.5)$ into the Eqn. $(C.3)$, and with the help of Eqns. (3.34), (3.35) and (3.48), the torque expression becomes

$$T_e = P[(L_d - L_q)i_d i_q + \psi_f i_q] = \frac{mP}{\omega}[(X_{md} - X_{mq})i_q i_d + E_0 i_q]$$
$$= \frac{PE_i}{\omega}(I_q \cos\delta_i - I_d \sin\delta_i) = \frac{mP}{\sqrt{2}} N_s k_s K_{dp1} \phi_m (I_q \cos\delta_i - I_d \sin\delta_i) \qquad \text{(C.6)}$$

Equation (C.6) is noted as Eqn. (3.57). Therefore, from a theoretical point of view the flux method is equivalent to using the conventional virtual work method.

Appendix D

Resultant Magnetic Flux Density

Let B_x and B_y be equal to

$$B_x = B_1 \sin(\omega t + \varphi_1)$$
$$B_y = B_2 \sin(\omega t + \varphi_2) \tag{D.1}$$

respectively, then the expression of resultant of magnetic flux densities can be derived as follows;

$$\begin{aligned}
B^2(t) &= B_x^2(t) + B_y^2(t) \\
&= B_1^2 \sin^2(\omega t + \varphi_1) + B_2^2 \sin^2(\omega t + \varphi_2) \\
&= \frac{1}{2}\{B_1^2 + B_2^2 - [B_1^2 \cos(2\omega t + 2\varphi_1) + B_2^2 \cos(2\omega t + 2\varphi_2)]\} \\
&= \frac{1}{2}\{B_1^2 + B_2^2 - [B_1^2(\cos 2\varphi_1 \cos 2\omega t - \sin 2\varphi_1 \sin 2\omega t) \\
&\quad + B_2^2(\cos 2\varphi_2 \cos 2\omega t - \sin 2\varphi_2 \sin 2\omega t)]\} \\
&= \frac{1}{2}\{B_1^2 + B_2^2 - [(B_1^2 \cos 2\varphi_1 + B_2^2 \cos 2\varphi_2) \cos 2\omega t \\
&\quad - (B_1^2 \sin 2\varphi_1 + B_2^2 \sin 2\varphi_2) \sin 2\omega t)]\} \\
&= \frac{1}{2}[B_1^2 + B_2^2 - A\cos(2\omega t + \beta)]
\end{aligned} \tag{D.2}$$

where

$$\begin{aligned} A &= [(B_1^2 \cos 2\varphi_1 + B_2^2 \cos 2\varphi_2)^2 + (B_1^2 \sin 2\varphi_1 + B_2^2 \sin 2\varphi_2)^2]^{\frac{1}{2}} \\ &= [B_1^4 + B_2^4 + 2B_1^2 B_2^2 (\cos 2\varphi_1 \cos 2\varphi_2 + \sin 2\varphi_1 \sin 2\varphi_2)]^{\frac{1}{2}} \\ &= [B_1^4 + B_2^4 + 2B_1^2 B_2^2 \cos 2(\varphi_1 - \varphi_2)]^{\frac{1}{2}} \end{aligned} \tag{D.3}$$

and

$$\beta = \arctan \frac{B_1^2 \sin 2\varphi_1 + B_2^2 \sin 2\varphi_2}{B_1^2 \cos 2\varphi_1 + B_2^2 \cos 2\varphi_2} \tag{D.4}$$

Appendix E

Circuit Layouts of Torque Angle Measurement System

Figure E.1 shows the circuit and waveforms at different points of the voltage phase meter. The applied phase voltage signal is obtained through a 110:3 V step-down transformer. Before the reduced sinusoidal voltage is converted to a 5V rectangular pulse by the zero-crossing voltage detector, a phase-lag shifter with a range of 0° to 180° is employed to provide an approximate means for positioning the zero torque angle. As the whole circuit operates on a single 5V supply, which makes the zero-crossing from negative to positive of the waveform become useless, the instant of the zero-crossing from positive to negative is used to signal the applied voltage. As a consequence of this 180° phase shift, the net effect of the phase shifter has become as a phase-lead network with a range of 0° to 180°. In order to make the phase shifter able to work as both phase-lead and phase-lag circuit, a compensator is introduced to offset the phase to a certain degree as desired at the output of the compensator by adjusting the RC time constant of the monostable.

In order to enable this device to be applicable to both the motoring and generating modes, a multiplexer circuit as shown in Fig. E.2 is employed. The output 1Y of

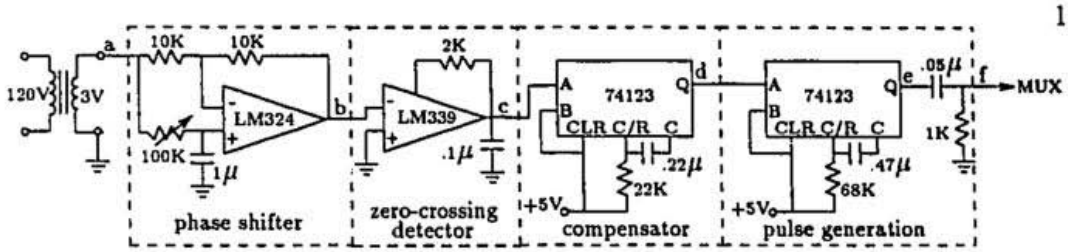

(a)

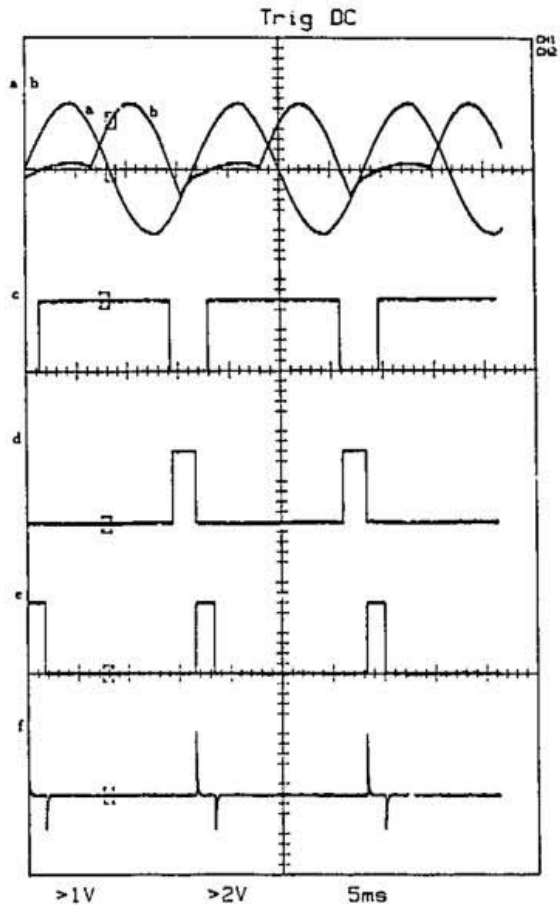

(b)

Figure E.1: Circuit and waveforms of voltage phase meter

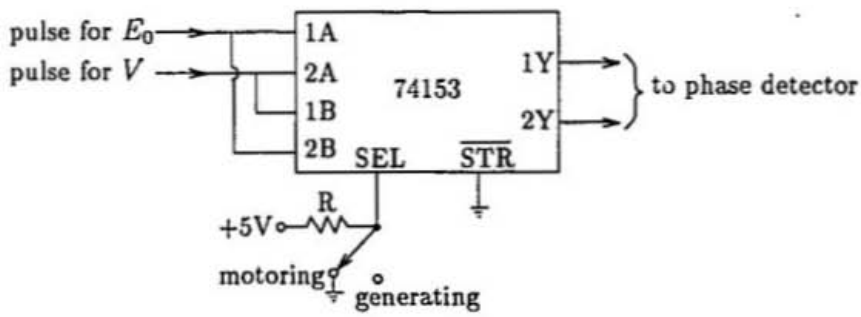

Figure E.2: Multiplexer circuit

the multiplexer is now fixed as the reference signal only, and the phase displacement signal will always be output from 2Y.

Once the signal from MUX 1Y to start a pulse and the signal from MUX 2Y to stop the pulse are fed into the phase detector as shown in Fig. E.3(a), a pulse of width equal to the phase shift between the induced excitation voltage and applied voltage is produced in the output Q of the positive-edge-triggered D flip-flop. The pulse inhibitor is employed to ensure that no further gate pulses would pass to the AND gate at point f until the reset signal is issued. The waveforms at various points are shown in Fig. E.3(b). To obtain a stable reading, the buffer is enabled after the counting is over and hold the information until the arrival of next count. The output of the buffer is further fed into a microprocessor using 8255 programmable peripheral interface. The 8255 is configured as mode 0. Port A and port B are used as input ports to the microprocessor for the 16-bit data transfer. Port C upper ($C_4 - C_7$) is used as output port for interrupt acknowledgment ($\overline{INTA}$) to restart the measurement of torque angle and port C lower ($C_0 - C_3$) is used as input port for interrupt signal to request a read from microprocessor when the updated buffer data is ready. At the same time, the buffered data are also decoded by display driver into 7-segment LED display.

The clock signal for latching the buffer and the interrupt signal can be derived from the output of the pulse inhibitor at point f of Fig. E.3. Since for a 16-bit cascade counter, the input signal must propagate through various flip-flops before the counter settles to its final steady-state value, a delay element is employed to account for the propagation delay as shown in Fig. E.4(a), where the first monostable provides 40 μs time delay. Because the latching takes place on the positive-going

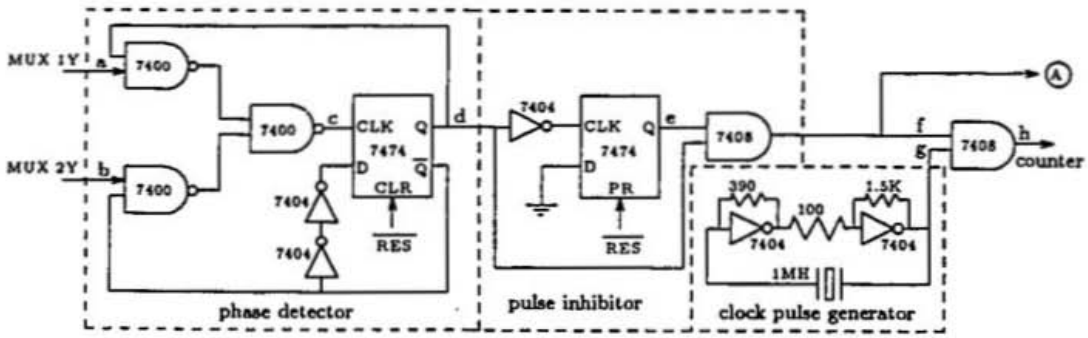

(a) circuit layout

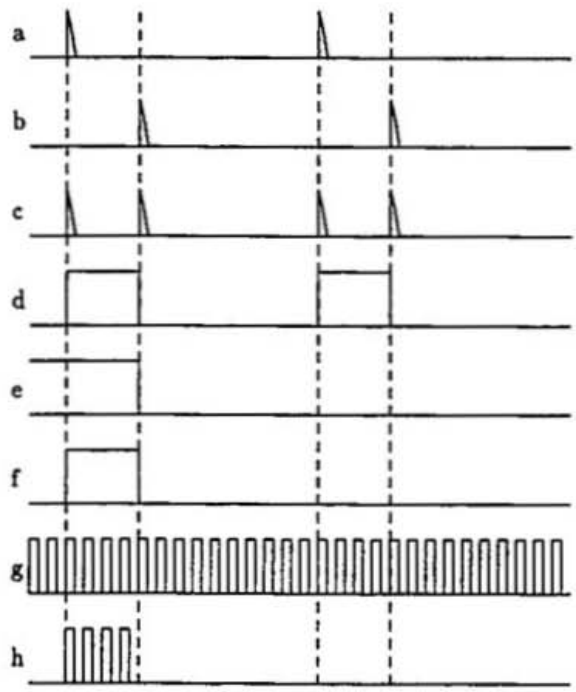

(b) waveforms at various points

Figure E.3: Circuit layouts and waveforms of torque angle detector

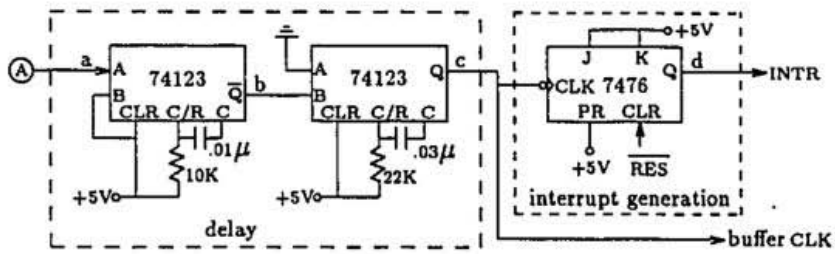

(a) circuit layout

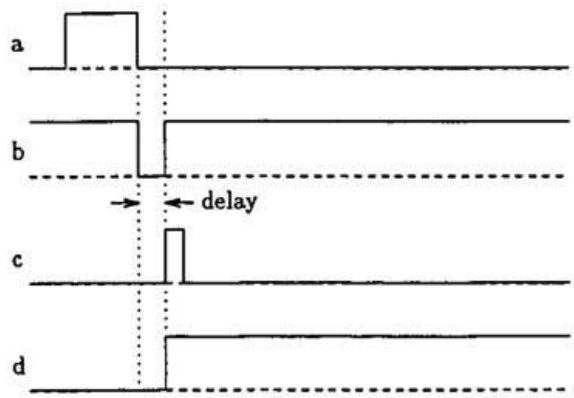

(b) waveforms at various points

Figure E.4: Circuit and waveforms of buffer clock and interrupt signal generator

edge of the clock pulse, another monostable is used to generate the required buffer clock pulse. The interrupt signal is produced using a JK flip-flop whose output becomes high once the delay is over, as shown in the waveforms Fig. E.4(b).

Appendix F

Grid Generation

The entire stator grid and the partial rotor grid in slot region are generated automatically by means of generalized half slot pitch modules as shown in Fig. F.1(a). The remainder rotor grid is generated in a similar manner using the generalized half pole module as shown in the Fig. F.1(b). These modules are fully flexible in the sense that all major geometrical dimensions can be specified at will. The stator and rotor grids are joined together in the airgap by means of an airgap fitting algorithm. The algorithm combines the two grids by the generation of a row of elements in airgap. The following steps summarize the salient features of this algorithm.

1. The nodes of the tip points of teeth on stator inner surface and rotor outer surface are identified as pivot nodes. These pivot nodes on both sides are radially mapped onto each other in order to generate new nodes which will not be considered as pivot nodes as concerns the projected surface.
2. Relocate all non-pivot nodes in equal interval between every and each pair of pivot nodes on both surfaces.
3. Generate triangle elements one by one in entire airgap according to the following notion of quality factor[47]. Let triangle have side lengths a, b and c,

then the quality factor of a triangle is defined as

$$q = \frac{8(s-a)(s-b)(s-c)}{abc} \tag{F.1}$$

Where s is semi-perimeter of the triangle, that is

$$s = \frac{a+b+c}{2} \tag{F.2}$$

An optimal triangle is the one which has maximum q. The *best* triangle shape is equilateral, for which $q = 1$. Slender triangles have appropriately low q value. If the triangle degenerates to a set of co-linear points, $q = 0$. Thus, all possible triangles are in the range:

$$0 \leq q \leq 1$$

Referring to Fig. F.2, an element is formed in the following manner. Supposing node 1 and node 2 have been connected. It is obvious that either way of connecting node 2 with node 3 or connecting node 1 with 4 will work for the generation of a new element. However, the quality factor q of the $1-2-4$ triangle is larger than that of the 1-2-3 triangle. Therefore, connecting node 1 with node 4 is preferred. This process is repeated until all the nodes along the stator inner and rotor outermost surfaces are covered.

4. Make necessary adjustment to the inner layer grids of the stator and the outmost layer grids of the rotor due to the addition and movement of the nodes along the surfaces of both sides in airgap, as above mentioned in step 1 and step 2. This adjustment is processed in a similar way as the generation of airgap elements in step 3 in terms of the notion of quality factor of a triangle. However, it should be noted that, due to the alternate encounter of slots and

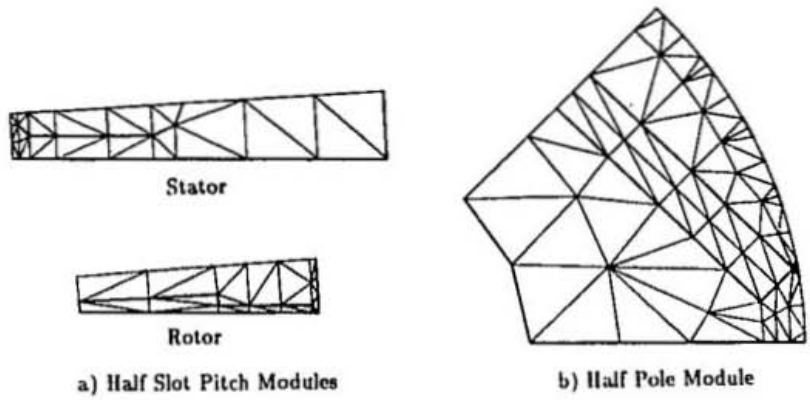

Figure F.1: Finite element grid of generalized modules

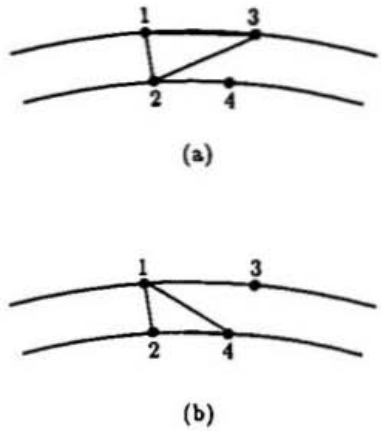

Figure F.2: Formation of triangle elements using the notion of quality factor

teeth, the application of quality factor for the formation of these elements must be confined to the same material individually, so as to avoid such an element that consists of different mediums.

After the initial finite element grid is generated using above scheme, the notion of Delaunay triangulation may be applied to consequent refining in the locations with greater error[48].